



PARTICLE-LADEN MULTIPHASE FLOWS: A FINITE ELEMENT ANALYSIS
ON BIOFUEL PARTICLE EMISSIONS

João Paulo Innocente de Souza

Dissertação de Mestrado apresentada ao Programa de Pós-graduação em Engenharia Mecânica, COPPE, da Universidade Federal do Rio de Janeiro, como parte dos requisitos necessários à obtenção do título de Mestre em Engenharia Mecânica.

Orientador: Gustavo Rabello dos Anjos

Rio de Janeiro
Dezembro de 2021

PARTICLE-LADEN MULTIPHASE FLOWS: A FINITE ELEMENT ANALYSIS
ON BIOFUEL PARTICLE EMISSIONS

João Paulo Innocente de Souza

DISSERTAÇÃO SUBMETIDA AO CORPO DOCENTE DO INSTITUTO
ALBERTO LUIZ COIMBRA DE PÓS-GRADUAÇÃO E PESQUISA DE
ENGENHARIA DA UNIVERSIDADE FEDERAL DO RIO DE JANEIRO COMO
PARTE DOS REQUISITOS NECESSÁRIOS PARA A OBTENÇÃO DO GRAU
DE MESTRE EM CIÊNCIAS EM ENGENHARIA MECÂNICA.

Orientador: Gustavo Rabello dos Anjos

Aprovada por: Prof. Gustavo Rabello dos Anjos

Prof. Marcelo José Colaço

Prof. Norberto Mangiavacchi

Prof. Prashant Valluri

RIO DE JANEIRO, RJ – BRASIL

DEZEMBRO DE 2021

Souza, João Paulo Innocente de
Particle-laden Multiphase Flows: A Finite Element
Analysis on Biofuel Particle Emissions/João Paulo
Innocente de Souza. – Rio de Janeiro: UFRJ/COPPE,
2021.

XV, 91 p.: il.; 29, 7cm.

Orientador: Gustavo Rabello dos Anjos
Dissertação (mestrado) – UFRJ/COPPE/Programa de
Engenharia Mecânica, 2021.

Referências Bibliográficas: p. 89 – 91.

1. FEA. 2. Biofuel. 3. Particles. I. Anjos, Gustavo
Rabello dos. II. Universidade Federal do Rio de Janeiro,
COPPE, Programa de Engenharia Mecânica. III. Título.

*"Se a educação sozinha não transforma a sociedade, sem ela tampouco a sociedade muda." -
Paulo Freire*

Agradecimentos

Primeiramente, dedico este trabalho aos meus pais, Paulo e Dhebora, que foram fundamentais no meu desenvolvimento como cidadão e me proporcionaram toda a base para que pudesse chegar até aqui. Agradeço, ainda, aos outros familiares por todo o incentivo e apoio em cada etapa da vida.

Agradeço imensamente ao meu melhor amigo e maior incentivador, Diego, pelas horas de conversa e distrações, sobretudo no período de isolamento, que se estendeu por grande parte do meu curso de mestrado. Estendo os agradecimentos aos outros amigos que sempre se mantiveram presentes de alguma forma.

Deixo aqui, também, minha enorme admiração pelo meu orientador, Professor Gustavo Rabello, que, desde o início, me guiou e se dedicou de forma generosa e paciente ao trabalho que nos propusemos desenvolver, servindo de grande referência para minha vida acadêmica. Estendo a admiração aos outros professores do Programa de Engenharia Mecânica da COPPE/UFRJ pelas ótimas aulas ministradas, apesar das dificuldades impostas pelo ensino remoto, mantendo a excelência do ensino. Direciono, ainda, meus cumprimentos aos membros da minha banca de defesa, que aceitaram fazer parte da avaliação deste trabalho.

À CAPES, minha gratidão pela bolsa de estudos a mim fornecida como forma de incentivo ao pesquisador brasileiro e, ao GESAR (Grupo de Estudos e Simulações Ambientais em Reservatórios) da UERJ, minha admiração e agradecimento pelos equipamentos a mim concedidos para que pudesse executar minhas simulações.

Resumo da Dissertação apresentada à COPPE/UFRJ como parte dos requisitos necessários para a obtenção do grau de Mestre em Ciências (M.Sc.)

**ESCOAMENTO CARREGADO DE PARTÍCULAS: UMA ANÁLISE DE
ELEMENTOS FINITOS NA EMISSÃO DE PARTÍCULAS DE
BIOCOMBUSTÍVEIS**

João Paulo Innocente de Souza

Dezembro/2021

Orientador: Gustavo Rabello dos Anjos

Programa: Engenharia Mecânica

O escoamento multifásico carregado de partículas é um importante assunto de estudo em mecânica dos fluidos, especialmente na indústria de óleo e gás. Neste trabalho, a emissão de partículas pelo consumo do biocombustível é analisada e simulada, a fim de se obter os principais efeitos desse transporte até a atmosfera, que podem causar danos ao meio ambiente e à saúde. A fase contínua é simulada numericamente diretamente através das equações de Navier-Stokes, cujos resultados estão em total concordância com os apresentados na literatura. Quanto à dispersão sólida, é feita uma análise de Euler-Lagrange, que permite um melhor entendimento da trajetória de cada partícula. Um simulador numérico é construído por meio do Método de Elementos Finitos (FEM) e os resultados são obtidos para diferentes geometrias encontradas em sistemas de biocombustíveis. Todos os resultados e comparações são apresentados e discutidos ao longo deste documento. Para simular e comparar mecanismos de filtragem de particulados na exaustão de motores diesel, é utilizado o DPF (Filtro de Partículas Diesel) com dados referentes ao diesel e biodiesel, sendo possível fazer uma comparação nas emissões de partículas poluentes, sendo este último mais vantajoso devido à menor taxa de emissão, conforme mostrado na simulação deste texto. Variações da geometria também são avaliadas em relação à eficiência de filtragem.

Abstract of Dissertation presented to COPPE/UFRJ as a partial fulfillment of the requirements for the degree of Master of Science (M.Sc.)

PARTICLE-LADEN MULTIPHASE FLOWS: A FINITE ELEMENT ANALYSIS
ON BIOFUEL PARTICLE EMISSIONS

João Paulo Innocente de Souza

December/2021

Advisor: Gustavo Rabello dos Anjos

Department: Mechanical Engineering

Particle-laden multiphase flow is an important subject of study in fluid mechanics, especially in the oil and gas industry. In this work, the particle emission from biofuel consumption is analyzed and simulated, in order to obtain the main effects of such transportation into the atmosphere, that may cause environmental and health damages. The continuous phase is numerically simulated directly through the Navier-Stokes equations, for which the results are in complete accordance to the ones presented in the literature. As for the solid dispersion, an Euler-Lagrange analysis is made, which provides a better understanding of each particle trajectory. A numerical simulator is built by means of the Finite Element Method (FEM) and the results are obtained for different geometries found in biofuel systems. All the results and comparisons are shown and discussed throughout this document. In order to simulate and compare particulate filtering mechanisms in the exhaustion of diesel engines, the DPF (Diesel Particle Filter) is used with data referring to diesel and biodiesel, being possible to make a comparison in particulate emissions pollutants, the latter being more advantageous due to the lower emission rate, as shown in the simulation in this text. Geometry variations are also evaluated regarding filtration efficiency.

Contents

List of Figures	x
List of Tables	xv
1 Introduction	1
2 Literature Review	3
2.1 Literature Review on Biofuel	3
2.2 Literature Review on Numerical Methods for Fluid Dynamics and Multiphase Flow	6
3 Governing Equations	12
3.1 The Continuous Phase	12
3.2 The Porous Medium	16
3.3 The Solid Phase	18
3.4 The Final Set of Differential Equations	20
3.4.1 General Boundary Conditions	21
4 The Finite Element Analysis	22
4.1 The Variational Form	22
4.2 The Galerkin Method	24
4.3 The Semi-Lagrangian Formulation	29
5 Computational Implementation	32
5.1 Code Organization	32
5.2 The Graphical User Interface (GUI)	35
6 Verification and Physical Analysis	37
6.1 The Lid-driven Cavity	37
6.2 The Backward-facing Step Problem	39
6.3 Flow in a Channel with Obstacle	41
6.4 The Cavity with Natural Convection	43
6.5 The Expansion with Heat Transfer	45

6.6	The Poiseuille with Porous Region Flow	48
6.7	The Flow over Porous Medium	51
7	The Diesel Particulate Filter (DPF)	54
7.1	The Structure of the DPF	54
7.2	Particulate Size Distribution	55
7.3	The DPF Flow Simulation	58
7.4	The Particle-laden Multiphase Flow in the DPF	59
7.5	The DPF with Continuous Particulate Injection	64
7.6	Analysis of the Filter's Geometry	70
7.6.1	The Internal Steep Edge	70
7.6.2	The External Steep Edge	72
7.6.3	The Internal Step-shaped Edge	75
7.6.4	The External Step-shaped Edge	77
7.6.5	The Internal Harmonic-shaped Edge	80
7.6.6	The External Harmonic-shaped Edge	82
7.6.7	Comparison of Cases	85
8	Conclusion	86
	References	89

List of Figures

2.1	Net efficiency improvement based on [1].	4
2.2	CO_2 emission of the tailor-made biofuel blends and B5 diesel based on data from [2], showing that pure Diesel produces a higher amount of CO_2	5
2.3	Particle size distributions, found in [3], where the differences between diesel and biodiesel particulate distribution are noticeable, since diesel produces larger particles and in a higher concentration.	5
2.4	Three different models for flow in conjugated porous regions as seen in [4]. When compared, NSD and NSF show sharp transition between the flow and porous media regions, while the PE model presents a smooth transition between regions. Additionally, the PE shows a lower parabolic profile for the poiseuille flow and, as opposite, the NSF model presents an overshooting of the maximum value at Height = 2.	11
3.1	Schematic drag and buoyancy forces on a single particle in an incompressible flow that reaches the body with a velocity \mathbf{u}	18
3.2	Drag coefficient as a function of Re_p , [5].	20
4.1	Element's nodes representation, with local (i) and respective global (k) numbers, for the MINI (left) and quadratic (right) kinds. The scheme also denotes the points where pressure, temperature and velocity are calculated.	24
4.2	Base element in the (L_1, L_2) coordinate system. This coordinate system is chosen to coincide with the linear element's shape functions, denominated L_1 , L_2 and $L_3 = 1 - L_1 - L_2$	26
4.3	MINI element shape functions, (a) N_1 , (b) N_2 , (c) N_3 , (d) N_4 , as functions of L_1 and L_2 , the coordinate system of the base triangle.	26
4.4	Quadratic element shape functions, (a) N_1 , (b) N_2 , (c) N_3 , (d) N_4 , (e) N_5 , (f) N_6 , as functions of L_1 and L_2 , the coordinate system of the base triangle.	27

4.5	Scheme of the semi-lagrangian formulation showing how the position \mathbf{x}_d , at the previous time step t_d , is determined. The vector $-\mathbf{u}\Delta t$ is used for said calculation, where \mathbf{u} is the velocity of the fluid particle located at the position \mathbf{x} of the node.	29
5.1	Chart representing the classes in the code implementation using Object Oriented Programming (OOP) in <i>Python</i> , [6].	32
5.2	Unstructured mesh of a complex geometry containing 1626 elements and 883 vertices from <i>Gmsh</i>	34
5.3	Input example from <i>.xml</i> file showing parameters and boundary conditions for the analyzed case. The mesh used is shown in the parameter called "name".	34
5.4	Graphical User Interface (GUI) main tab, where all simulation parameters can be set, as well as boundary conditions. Both can be saved in a <i>.xml</i> file and loaded to this tab.	35
5.5	Graphical User Interface (GUI) output tab, where the real-time simulation can be observed. In this example, a Poiseuille flow with particles is being run.	36
6.1	Boundary conditions for the lid-driven cavity problem, for $Re = 100$	37
6.2	Velocity fields in the (a) horizontal and (b) vertical directions for the lid-driven cavity problem, for $Re = 100$	38
6.3	Verification of the lid-driven cavity problem, for $Re = 100$, with [7].	38
6.4	Mesh convergence analysis for the lid-driven cavity problem, doubling the size of the mesh at each analysis. Mesh convergence analysis is useful to determine the ideal number of elements in the mesh, avoiding computational processing waste.	39
6.5	Boundary conditions for the backward-facing step problem.	40
6.6	Horizontal velocity field and stream lines for the backward-facing step problem, for $Re = 800$. The recirculation positions, X_1, X_2 and X_3 , are also shown.	40
6.7	Boundary conditions for the in a channel with obstacle.	41
6.8	Horizontal velocity field for the flow in a channel with obstacle, with $Re = 1000$ and $Ga = 1/Fr^2 = 10^{-4}$	42
6.9	Boundary conditions for the natural convection problem.	43
6.10	Temperature field with stream lines in the natural convection problem.	43
6.11	Velocity fields in the (a) horizontal and (b) vertical directions for the cavity with natural convection problem.	44
6.12	Particles' motion at different time steps for the natural convection problem.	45

6.13	Boundary conditions for the expansion problem.	46
6.14	Stream lines in the expansion problem, for $Re = 1000$	46
6.15	Temperature field in the expansion problem, for $Re = 1000$ and $Pr = 0.7$	47
6.16	Particles' motion at different time steps, for $Re = 1000$	48
6.17	Boundary conditions for a Poiseuille with porous region flow, for $Re = 100$	49
6.18	Horizontal velocity field for the Poiseuille with porous region flow, for $Re = 100$, $Da = 0.025$ and $Fo = 2.0$	49
6.19	Temperature field for the Poiseuille with porous region flow, for $Re = 100$, $Da = 0.025$, $Fo = 2.0$ and $Pr = 0.7$	49
6.20	Velocity field along the horizontal axial line for the Poiseuille with porous region flow, for different values of Darcy number (Da).	50
6.21	Pressure field along the horizontal axial line for the Poiseuille with porous region flow, for different values of Darcy number (Da).	50
6.22	Boundary conditions for the flow over porous medium, for $Re = 6, 38$, $Da = 0.373$, $Fo = 1.952$ and $Ga = 1/Fr^2 = 10^{-4}$	51
6.23	Horizontal velocity field for the flow over porous medium, for $Re = 6.38$, $Da = 0.373$, $Fo = 1.952$ and $Ga = 1/Fr^2 = 10^{-4}$	52
6.24	Velocity field represented by vectors in the entry region for the flow over porous medium, for $Re = 6, 38$, $Da = 0.373$, $Fo = 1.952$ and $Ga = 1/Fr^2 = 10^{-4}$	52
6.25	Verification of the Darcy/Forchheimer model implemented, [4], for $Re = 6, 38$, $Da = 0.373$, $Fo = 1.952$ and $Ga = 1/Fr^2 = 10^{-4}$	53
7.1	Schematic drawing of the DPF. The structure resembles a honeycomb, through which the fluid enters and gets filtered.	54
7.2	Schematic drawing of the DPF's channel, [8], where the filtration system is evidenced. The analyzed region is comprised within the dashed red line.	55
7.3	Normal curves and their data fit for diesel and biodiesel, based on [3]. The curve fit is used to quantify the normal distribution of particles emitted by both fuels. The mean diameter of biodiesel particles are noticed to be smaller than diesel ones, with a lower concentration as well.	57
7.4	DPF flow simulation, based on [8], with a proportion between the total length and the entry channel of 118.8.	58
7.5	DPF mean-line horizontal velocity compared to [8], with $Re = 228$. .	59
7.6	Scheme of the DPF and its dimensions.	60

7.7	Horizontal velocity field and particles' trajectories at different time steps of the diesel DPF, for $Re = 228$, $Da = 10^{-4}$, $Fo = 2.0$ and $Ga = 1/Fr^2 = 10^{-2}$.	61
7.8	Horizontal velocity field and particles' trajectories at different time steps of the biodiesel DPF, for $Re = 228$, $Da = 10^{-4}$, $Fo = 2.0$ and $Ga = 1/Fr^2 = 10^{-2}$.	63
7.9	DPF pressure field, for $Re = 228$, $Da = 10^{-4}$ and $Fo = 2.0$.	64
7.10	DPF velocity field near the exit, for $Re = 228$, $Da = 10^{-4}$ and $Fo = 2.0$.	64
7.11	Horizontal velocity field and particles' trajectories at different time steps of the diesel DPF for a continuous injection, for $Re = 228$, $Da = 10^{-4}$, $Fo = 2.0$ and $Ga = 1/Fr^2 = 10^{-2}$.	66
7.12	Horizontal velocity field and particles' trajectories at different time steps of the biodiesel DPF for a continuous injection, for $Re = 228$, $Da = 10^{-4}$, $Fo = 2.0$ and $Ga = 1/Fr^2 = 10^{-2}$.	68
7.13	Particles' admission and exhaustion rates for diesel-powered engines.	69
7.14	Particles' admission and exhaustion rates for biodiesel-powered engines.	69
7.15	Scheme of the DPF with internal steep edge.	70
7.16	Velocity field and particle distribution in the permanent regime for the diesel DPF with an internal steep edge.	71
7.17	Velocity field and particle distribution in the permanent regime for the biodiesel DPF with an internal steep edge.	71
7.18	Particles' admission and exhaustion rates for diesel-powered engines, for a DPF with an internal steep edge.	71
7.19	Particles' admission and exhaustion rates for biodiesel-powered engines, for a DPF with an internal steep edge.	72
7.20	Scheme of the DPF with external steep edge.	72
7.21	Velocity field and particle distribution in the permanent regime for the diesel DPF with an external steep edge.	73
7.22	Velocity field and particle distribution in the permanent regime for the biodiesel DPF with an external steep edge.	73
7.23	Particles' admission and exhaustion rates for diesel-powered engines, for a DPF with an external steep edge.	74
7.24	Particles' admission and exhaustion rates for biodiesel-powered engines, for a DPF with an external steep edge.	74
7.25	Scheme of the DPF with internal step-shaped edge.	75
7.26	Velocity field and particle distribution in the permanent regime for the diesel DPF with an internal step-shaped edge.	75
7.27	Velocity field and particle distribution in the permanent regime for the biodiesel DPF with an internal step-shaped edge.	76

7.28 Particles' admission and exhaustion rates for diesel-powered engines, for a DPF with an internal step-shaped edge.	76
7.29 Particles' admission and exhaustion rates for biodiesel-powered en- gines, for a DPF with an internal step-shaped edge.	77
7.30 Scheme of the DPF with external step-shaped edge.	77
7.31 Velocity field and particle distribution in the permanent regime for the diesel DPF with an external step-shaped edge.	78
7.32 Velocity field and particle distribution in the permanent regime for the biodiesel DPF with an internal step-shaped edge.	78
7.33 Particles' admission and exhaustion rates for diesel-powered engines, for a DPF with an external step-shaped edge.	79
7.34 Particles' admission and exhaustion rates for biodiesel-powered en- gines, for a DPF with an external step-shaped edge.	79
7.35 Scheme of the DPF with internal harmonic-shaped edge.	80
7.36 Velocity field and particle distribution in the permanent regime for the diesel DPF with an internal harmonic-shaped edge.	80
7.37 Velocity field and particle distribution in the permanent regime for the biodiesel DPF with an internal harmonic-shaped edge.	81
7.38 Particles' admission and exhaustion rates for diesel-powered engines, for a DPF with an internal harmonic-shaped edge.	81
7.39 Particles' admission and exhaustion rates for biodiesel-powered en- gines, for a DPF with an internal harmonic-shaped edge.	82
7.40 Scheme of the DPF with external harmonic-shaped edge.	82
7.41 Velocity field and particle distribution in the permanent regime for the diesel DPF with an external harmonic-shaped edge.	83
7.42 Velocity field and particle distribution in the permanent regime for the biodiesel DPF with an external harmonic-shaped edge.	83
7.43 Particles' admission and exhaustion rates for diesel-powered engines, for a DPF with an external harmonic-shaped edge.	84
7.44 Particles' admission and exhaustion rates for biodiesel-powered en- gines, for a DPF with an external harmonic-shaped edge.	84

List of Tables

Chapter 1

Introduction

The present work is intended to numerically analyze multiphase flows under several conditions found in biofuel consumption. Beforehand, a literature review is provided, in order to evaluate previous studies on the referred theme. As simulation method, the Finite Element Analysis (FEA), will be used and the whole formulation for the proposed problems will be developed. The stream-vorticity will be cited as a well established formulation and compared to this work, for which the Navier-Stokes and continuity equations in their original form are discretized through FEA.

The continuous phase, representing the fluid, will be treated through the Euler approach and its governing equations for mass, momentum and energy conservation will be completely discretized in order to simulate the complete phenomenon. The FEA is then applied to the governing equation, so that a computational solution is provided to the non-linear system of differential equations.

Particles' motion will be determined by the Lagrange approach, where each particle is tracked down simultaneously and moved with the computed flow field. In this work, drag and buoyancy are considered as main forces in the particle, thus configuring a one-way coupling. For different geometries and conditions, particles' inertia will be evaluated, in order to analyze discrepancies between trajectories and stream lines provided by the continuous phase.

The entire implementation is made through *Python*'s scientific packages, provided by *Anaconda*'s distribution, where all the modules, including matrix assemblies and semi-lagrangian calculations, were fully coded for this work. The mesh generation is made using the open source software *Gmsh*, where different geometries are modeled, in order to represent the studied cases.

The second chapter of this document is reserved to a broad literature review on both biofuel and numerical methods for fluid simulation. Several scientific articles are analyzed in order establish the previous work that has already been developed in this area.

Chapter 3 presents the fundamentals of fluid dynamics and transport of parti-

cles, going through Reynolds' transport theorem to enunciate the Navier-Stokes and energy balance equations. All the correlations are derived to their dimensionless forms, so that dimensionless numbers can be used as simulation adjustable parameters. Also, the Darcy/Forchheimer formulation is presented, to represent flows in completely or partially porous regions.

The fourth chapter discusses the discretization of the problem's equations, presenting the variational form, also known as weak form. The Galerkin method is used to approximate the continuous quantities to their respective discrete representation, using two kinds of elements, the MINI and the quadratic ones. Next, the semi-lagrangian approach is explained as a way of calculating time derivatives, composing the linear system to be solved computationally.

Chapter 5 is the section where the computational implementation is explained, going through the different classes in the Object Oriented Programming (OOP) and a Graphical User Interface (GUI) created to facilitate the entire process of simulating and saving inputs, initial and boundary conditions and results. A command-line version of the software was also used and is shown in this chapter.

Chapter 6 is intended to show some physical analysis as well as a method verification by comparing a classical CFD problem with results taken from the literature. Four other cases are simulated, showing results from a backward-facing step problem and a flow around a cylinder case, as well as particle distribution in space and time for an expansion and a convective cavity. For partially porous media, a code verification is also presented, comparing the results obtained for specific problem with the literature. Discussions around results are provided in order to guide conclusions about the real and simulated phenomena.

Chapter 7 is reserved for the entire DPF analysis, showing how particle distribution can be fit into a normal distribution for both diesel and biodiesel fuels. Said distribution is then used to simulate the filtering processes of the geometry that represents part of the filter. A comparison between diesel and biofuel regarding particle size, concentration and emissions is provided by the end of this chapter and, to conclude the analysis, different geometry variations are considered and evaluated.

Finally, chapter 8 concludes this work by summing up all the discussion and results presented, showing that FEA is a well established tool for Computational Fluid Dynamics (CFD) simulation. Also, as a closure, this chapter evaluates the main differences between diesel, which is a fossil fuel, and biodiesel, regarding, mainly, pollutant emissions. Future work is also presented, with the objective of improvement of the code.

Chapter 2

Literature Review

2.1 Literature Review on Biofuel

Biofuel is characterized as an energy source produced from biomass, opposed to those originated from geological processes, called fossil fuels. According to REHAM *et al.* [10], diesel, gasoline and natural gas are among the most commonly used fuels in the past few years. REHAM *et al.* [10] also state that fossil fuels are responsible for serious environmental changes, including the increase on global surface temperature. Following the same idea, XU *et al.* [11] defend that developing fuel from renewable sources, and not from fossil ones, has become an urgent matter, which led to government regulations and stringent laws on greenhouse gas reductions, as presented by HASHIM *et al.* [2]. Given that biofuel is "considered an economically feasible option as alternate fuel because of their improved emission characteristics" REHAM *et al.* [10] and "regulation on harmful emissions is becoming stricter" KIM *et al.* [1], Ethanol is a good example of biofuel used as a substitute for fossil fuels in vehicles, since it provides efficiency improvement and harmful emission reduction, as said by KIM *et al.* [1]. An important result shown by the authors is that the net indicated efficiency of an SI engine can be increased by 4.0% when ethanol is added to gasoline. Also, KIM *et al.* [1] show the correlation between the type of mixture ethanol+gasoline and the particle emission, found in many graphical plots in the article. One of them, for example, shows the particle size spectra for three different types of gasoline+ethanol mixtures. Figure 2.1 compares the efficiency between pure gasoline and the mixture, based on the plot from [1].

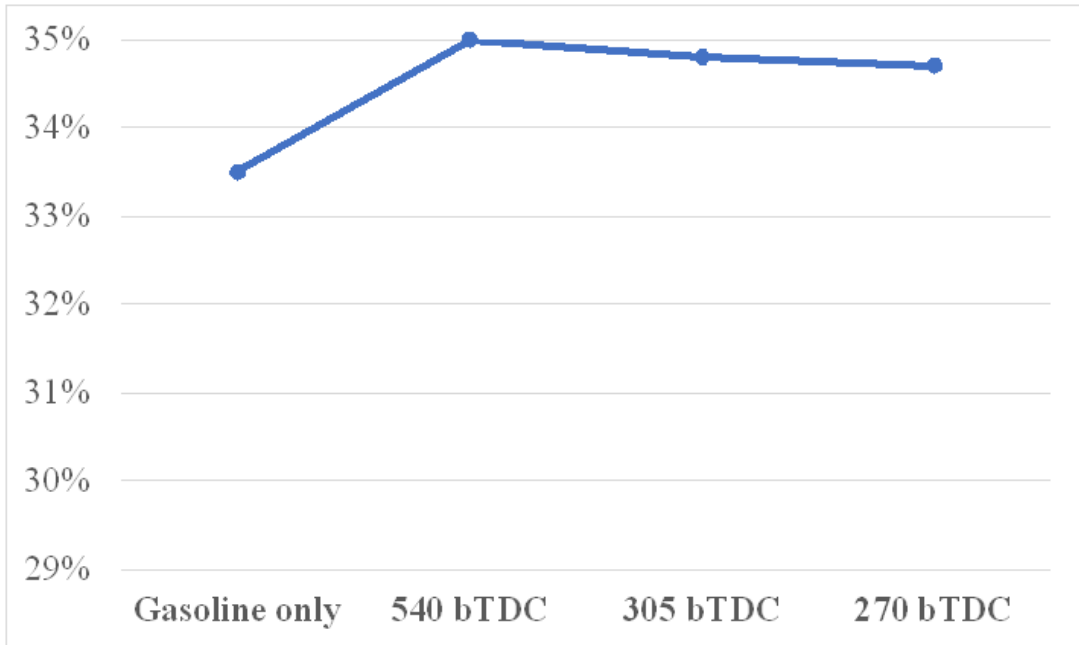


Figure 2.1: Net efficiency improvement based on [1].

As can be seen in Figure 2.1, the mixture between ethanol and gasoline provides a good net efficiency increase and, in addition, is a good renewable option for a fossil fuel substitute.

An important result shown by KIM *et al.* [1] is that the net indicated efficiency of an SI engine can be increased by 4.0% when ethanol is added to gasoline. Also, KIM *et al.* [1] show the correlation between the type of mixture ethanol+gasoline and the particle emission, found in many graphical plots in the article. One of them, for example, shows the particle size spectra for three different types of gasoline+ethanol mixtures.

Still in the topic of pollution and emissions, one of the findings by HASHIM *et al.* [2] is that, when comparing different biofuel blends with Diesel, biofuel blends present significant reduction on CO_2 emission, as can be seen in Figure 2.2, created based on data from [2]. Analyzing the bar chart, it is of easy conclusion that a minimum of 20% reduction on CO_2 emission is observed between Diesel and biofuel blends, Considering that, for biodiesel, there is a closed carbon chain, where the CO_2 emitted is also consumed by the biomass cultivation.

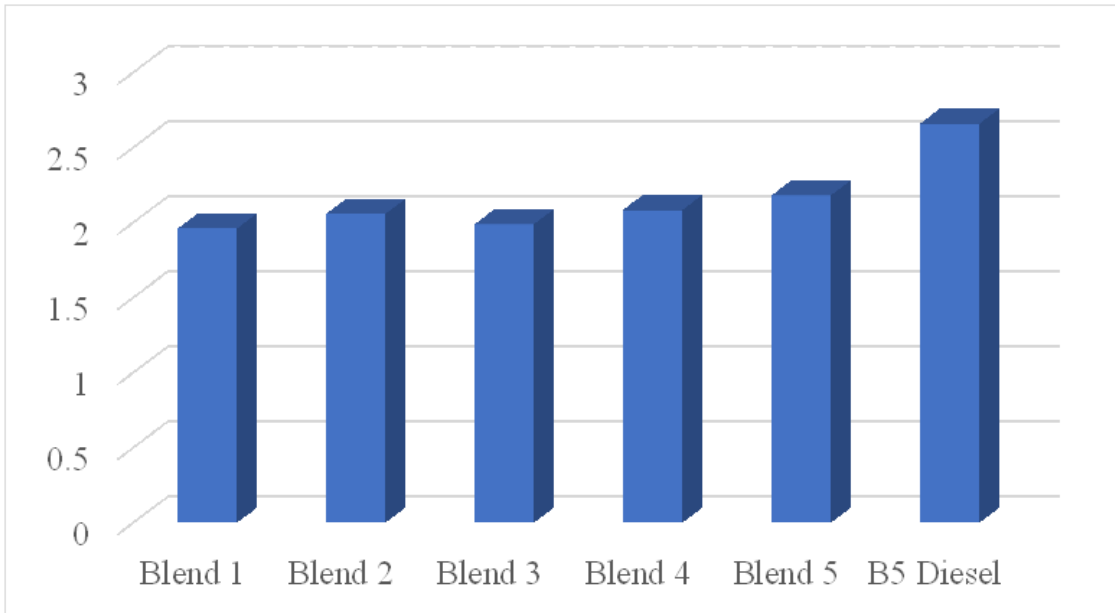


Figure 2.2: CO_2 emission of the tailor-made biofuel blends and B5 diesel based on data from [2], showing that pure Diesel produces a higher amount of CO_2 .

Another important aspect regarding pollutant emissions is the particulate matter that is emitted from these engines. RODRÍGUEZ-FERNÁNDEZ *et al.* [3] cite specifically the regeneration process of diesel and biofuel engines. For that, a size distribution of particulate matter is provided, as seen in Figure 2.3.

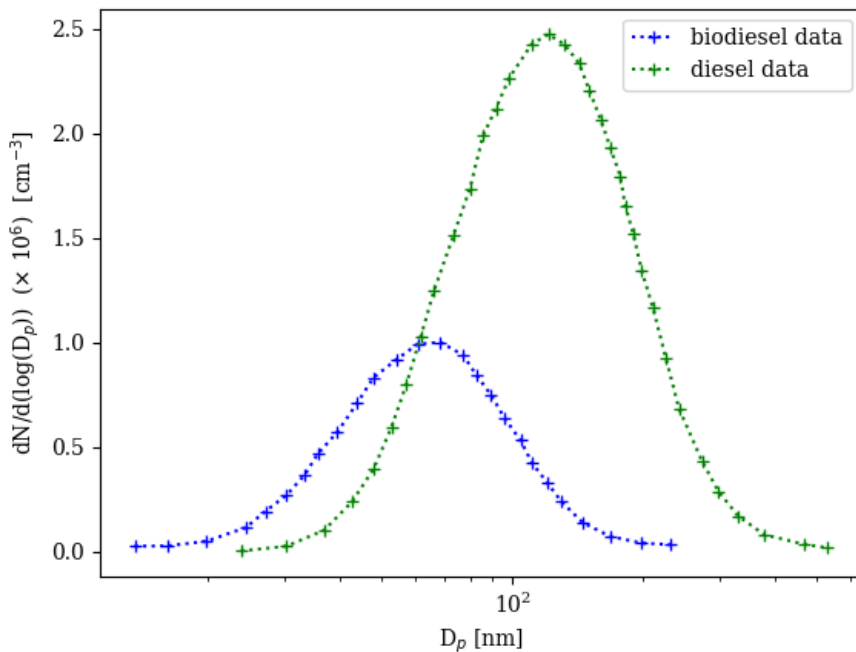


Figure 2.3: Particle size distributions, found in [3], where the differences between diesel and biodiesel particulate distribution are noticeable, since diesel produces larger particles and in a higher concentration.

Throughout the article, pressure drop in the filter is analyzed for the 4 types of fuels used, being pure diesel the most disadvantageous since particulate accumulation generates a higher pressure difference through time. The authors also conclude that biodiesel particles have a better oxidative reactivity of soot when compared to fossil diesel.

2.2 Literature Review on Numerical Methods for Fluid Dynamics and Multiphase Flow

It is widely known, among the scientific mechanical engineering community, that, when it comes to fluid mechanics or flow studies, the Navier-Stokes equations are an important and crucial point to be studied, along with the continuity equation, as presented by BATCHELOR [12]. As can be noticed, this set of equations, in spite of being a powerful way of characterizing the behavior of any sort of flow, has a complex form, mainly due to its non-linearity, with respect to velocity variables. Therefore, the analytical solution for them, as well as for some problems of heat conduction "can only be obtained in some simplified cases" ZHANG *et al.* [13]. Given that most common cases may not be simplified without considerable loss of information and representativeness of the phenomenon, numerical solutions are required.

Analyzing different methods to solve said system of equations, it is important to discuss a few of them. BESSAIH *et al.* [14] proposed a technique for the three-dimensional Navier-Stokes system of equations, which is notably more complex than the two dimensional one, and must be solved for some detailed cases, where the two-dimensional approach will not satisfy all the requisites. This technique consists in introducing a delay in the non-linear term ($\mathbf{u} \cdot \nabla \mathbf{u}$), which, according to BESSAIH *et al.* [14], "introduces a regularizing effect in the equations and allows to prove the uniqueness of weak solutions". ABDELWAHED *et al.* [15] analyze the two-dimensional form of the Navier-Stokes equations and proposes the use of the finite element method to find a solution for them. For that, ABDELWAHED *et al.* [15] use the stream function (ψ) and vorticity (ω) in the z direction formulation, modifying the set of equations to the vorticity form, shown in Eq. (2.1). The correlation $\omega - \psi$ is presented in Eq. (2.2), [15].

$$\frac{\partial \omega}{\partial t} + \mathbf{u} \cdot \nabla \omega - \nu \nabla^2 \omega = \nabla \times \mathbf{f} \quad (2.1)$$

$$\omega + \nabla^2 \psi = 0 \quad (2.2)$$

The boundary conditions, taken from [15], are given by:

$$\psi_d = 0 \quad \text{and} \quad \frac{\partial \psi}{\partial \mathbf{n}} = 0 \quad (2.3)$$

Where ψ_d is the homogeneous Dirichlet stream function boundary condition and \mathbf{n} is the normal vector outward the boundary.

The previous correlation is also presented and developed by DA CUNHA [7], where different cases of flow simulation, such as the lid-driven cavity and the flow past a cylinder are analyzed. TORO *et al.* [16] also make use of the finite element technique, providing examples on both flow and heat transfer phenomena. In this case, instead of using stream function vorticity, the authors simulate a potential flow, therefore an ideal fluid, around a cylinder. The equation for the potential (ϕ) is given by Eq. (2.4).

$$\nabla^2 \phi = \frac{\partial^2 \phi}{\partial x^2} + \frac{\partial^2 \phi}{\partial y^2} = 0 \quad (2.4)$$

Here, x and y are the independent variables and the Laplacian equation defines the velocity potential ϕ . The method proposed by TORO *et al.* [16] is tested for a triangular mesh in the region correspondent to a quarter of the total region and, as stated by TORO *et al.* [16], the example was chosen because it has an analytical solution, which made it easier to validate the numerical method.

Alternatively, BAGAI *et al.* [17] use the stream function-vorticity approach as well but, instead of the finite element method for the numerical solution, the authors use the finite difference approximation for the derivatives. The problem examined to validate the method is the four-sided lid driven cavity, with heat and mass transfer coupled to the fluid mechanics problem. The same method is also used by ZITOUNI *et al.* [18] in a TIG welding, where both thermal and fluid flow phenomena are modeled, evidentiating how broad flow simulation can be.

Besides finite element and finite difference methods, another widely used method in fluid mechanics is the finite volume method. The open source solvers of Open-FOAM use this method to solve systems of partial differential equations found in problems of fluid mechanics and heat transfer. ZHANG *et al.* [13] use these solvers

to investigate heat conduction problems in heterogeneous media. Since OpenFOAM is open source, researchers and average users may modify or even implement their own code in C++ using its solvers. As described by ZHANG *et al.* [13], the heat conduction equation, can be simply implemented by means of the addition of a small piece of code.

The results presented by the authors in their articles are satisfying in terms of showing the method used is adequate. TORO *et al.* [16] validate their simulation with the exact solution, since the problem proposed has analytical solution and is shown by the authors. The verification is given by comparing the input velocity with the values in the left border nodes, where the velocity boundary condition is set, which are close to the expected value. ABDELWAHED *et al.* [15] also compare their method with the exact solution of the quasi-Stokes problem, as shown in the document. The authors compare graphically both solutions, which makes evident how similar and accurate the numerical solution is to the exact one, and plot the total error associated to the simulation, concluding that many engineering problems related to the Navier-Stokes equations can be solved by means of this technique. BAGAI *et al.* [17] validate the four-sided lid driven cavity with values found in the literature, resulting in the plot found in the article, where the literature points are confronted with simulated results, showing that the simulated points are very close to the reference. The verification is made for a Reynolds number of 100, with velocity in both horizontal and vertical directions. Besides, the center of vortices are compared to two other literature sources, for three different Reynolds numbers, with satisfying results. The work also presents interesting streamline contour and vorticity plots to illustrate the example solved. ZHANG *et al.* [13] validate their results with the exact solution and ANSYS Fluent solution. The comparison is presented in the form of a plot as well, where simulated points are extremely close to the analytical solution, for different values of k . OpenFOAM provides excellent results when compared to the commonly used comercial CFD software ANSYS Fluent too. The authors illustrate the case studied with isotherms in different mesh grid distributions, comparing the associated error difference between them and concluding that a 50x50 mesh grid would be accurate enough to simulate the phenomena. This result is interesting due to its mesh analysis, which is very important as a preliminary conclusion in any numerical work, saving time in computer processing. DA CUNHA [7] provides a relevant verification of the lid-driven cavity problem, comparing with the literature, for different Reynolds number, showing that the Stream function-Vorticity formulation generates accurate results. The author also shows graphical results of the flow around a cylinder and the oscillation of the drag force.

The different methods presented in this section are well-known methods for computational fluid mechanics problems. After presenting their results, the next step

is to analyze the different approaches to multiphase flow simulation, which is an important aspect in biofuel particle emission analysis. The step that follows is to couple fluid mechanics study with particles subjected to drag and buoyancy in a flow, analyzing and evaluating methods for such simulation, going through mathematical models that describe and characterize all relevant aspects and phenomena in the fluid-particle interaction.

When solid-liquid mixtures are studied, researchers often come across separation methods, such as centrifuge, cyclones or hydrocyclones. HOFFMANN *et al.* [19] state in their work the importance of hydrocyclones and provides an investigation of its acting on liquids of varying viscosity. HOFFMANN *et al.* [19] offer both numerical and experimental analyses of particle trajectories inside the equipment, which, as described by them, are unexpected. The simulation type used is the large-eddy one (LES). This work is particularly interesting because it denotes a centrifugal flow, where the centrifugal force has great influence on the behavior of particle trajectories. The software used is STAR-CCM+version 6.06.017 from CD-Adapco and, since the technique used is LES, a spatial filter is applied to the flow variables.

Another approach on multiphase flow simulation is presented by BARGHI [20], by means of the commercial package ANSYS-Fluent. The main fluid is air and was modeled with the $\kappa - \epsilon$ model, which is of great importance on turbulent flow study and the values of κ and ϵ are calculated by BARGHI [20] through transport equations. For droplet/particle motion, equation an Euler-Lagrange approach is used, that is Newton's Second Law of motion for the particle subjected to forces made by the air flow (drag and buoyancy) and gravity. The same correlation for the drag coefficient, C_D , which the Shiller and Naumann one, is found in BORELLO *et al.* [21], where the impact and adhesion of particles are modeled. An Euler-Lagrange simulation is made in this work as well. BORELLO *et al.* [21] also provide the kinetic energy equation for the particles that hit the walls in the simulated body. It is an interesting discussion since many particles may be retained through adhesion in the walls and can lead equipments to failure, equivalent to the fouling phenomenon in compressors, as analyzed by BORELLO *et al.* [21]. The authors use LES and RANS (Reynolds Avarage Navier-Stokes Simulation). Eq. (2.5) and Eq. (2.6) show the variation in kinetic energy and the coefficient of restitution (e), respectively.

$$\Delta K = \frac{1}{2}m^*v_{r,n}^2 - \frac{1}{2}m^*v_{i,n}^2 \quad (2.5)$$

$$e^2 = 1 - \frac{\Delta K}{\frac{1}{2}m^*v_{i,n}^2} \quad (2.6)$$

GREIFZU *et al.* [22] present a good comparison between the commercial software ANSYS and OpenFOAM's open source solvers for Euler-Lagrange models using RANS simulation. As observed, ANSYS uses the Shiller and Naumann expression seen in BORELLO *et al.* [21] and BARGHI [20]. OpenFOAM, however has an alternative and slightly different expression for spherical bodies, as seen in GREIFZU *et al.* [22]. The authors also discuss the different kinds of coupling when simulating a multiphase flow, which is whether the liquid phase suffers any influence on its behavior from the solid particle phase. The case analyzed for comparison is the backward-facing step (BFS). BARGHI [20] validated the code by comparing the prill sizes of both measured and CFD analyses, resulting in values of same order. BARGHI [20] also demonstrated simulation results by means of velocity fields of air and droplets extracted from ANSYS, for three different designs and, according to the author "the effects of air flow at the outlet as well as the outlet geometry may also affect the dust escape from the tower", BARGHI [20]. HOFFMANN *et al.* [19] showed an interesting comparison between particle tracks obtained from the camera and the simulated trajectories. Both images are interestingly similar, validating the simulated results. The authors also presented a plot for axial velocity against radial position, confirming that particles and fluid that are closer to the center move upwards (to the overflow exit) and the ones that are closer to the walls, and therefore have a higher density, move downwards. The points are, then, averaged, resulting in a well behaved curve. BORELLO *et al.* [21] also validated their adhesion model through a real experiment comparison. Adhesion field images are shown next to experiment photos, which were executed under the same conditions for compressor blades. One interesting conclusion is that most deposits were induced by the presence of large recirculation. The verification shown by GREIFZU *et al.* [22] is important to prove the effectiveness of OpenFOAM's solvers, when compared to ANSYS's well known Fluent software. Also, experiments generated points that were coherent and form the same particle profile found on both simulation platforms. The main conclusion is that "there are almost no discrepancies between the profiles from OpenFOAM and ANSYS Fluent", [22]. Also, both are able to simulate turbulent flows.

For porous region analysis, the work seen in [4] is used as reference for the Darcy/Forchheimer formulation. The authors describe three different models to describe a mixed region (porous and free) problem. The first one is the Navier-Stokes/Darcy (NSD) model, the Navier–Stokes/Forchheimer (NSF) model and the Penalization (PE) model. For the first two, the formulation is uncoupled, having the interface connected by boundary conditions. As for the PE model, the whole domain

is described with a single equation of momentum conservation, which simplifies the solver. As stated by the authors, the PE method is a good approximation of the physical problem, in spite of interface being more well represented by the first two. This current work will be based on the PE method, since the interface is of low interest for the purpose of this thesis. Figure 2.4 shows the comparison between the models.

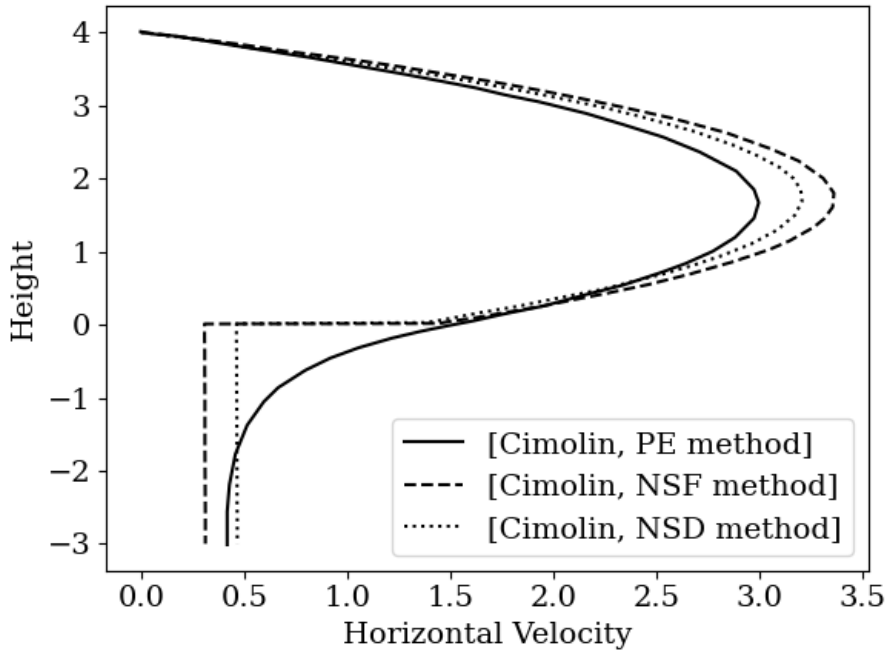


Figure 2.4: Three different models for flow in conjugated porous regions as seen in [4]. When compared, NSD and NSF show sharp transition between the flow and porous media regions, while the PE model presents a smooth transition between regions. Additionally, the PE shows a lower parabolic profile for the poiseuille flow and, as opposite, the NSF model presents an overshooting of the maximum value at Height = 2.

A similar approach is also used by MESQUIDA [8], who makes use of a CFD software to simulate a gasoline particle filter. The same consideration used in this current work, assuming symmetry between the channels of the DPF, is also used by the author, so that a two-dimensional approach could be used. MESQUIDA [8] simulates the flow in a single channel for different Reynolds numbers and also considers different turbulence models, using the Reynolds Average Numerical solution, also referred to as RANS, approach.

After describing different methodologies for particle tracking in a continuous fluid phase, a similar approach, using the finite element analysis for the fluid and a Lagrangian formulation for the solid phase, will be demonstrated and its results for different geometries will be shown throughout this work.

Chapter 3

Governing Equations

3.1 The Continuous Phase

The continuous phase is modeled by following the principles of mass and momentum balances. As seen in [12], the mass of a body is constant in time, which can be represented with the integral below:

$$\frac{d}{dt} \int_V \rho dV = 0 \quad (3.1)$$

Here, t is time, ρ is density and V is the volume occupied by the fluid. Reynolds's Transport Theorem can be applied, resulting in the next sequence, where the divergent theorem is used in the surface integral.

$$\int_V \frac{\partial \rho}{\partial t} dV + \oint_S \rho \mathbf{u} \cdot \mathbf{n} dA = 0$$

Where $\mathbf{u} = (u, v)$ is the velocity field and \mathbf{n} is the normal vector outward the surface S . The divergent theorem, [12], is used in order to transform surface integral into volume integral.

$$\int_V \left[\frac{\partial \rho}{\partial t} + \nabla \cdot (\rho \mathbf{u}) \right] dV = 0$$

Since the volume V is arbitrary, the infinitesimal volume is considered and divided by dV , resulting in:

$$\frac{\partial \rho}{\partial t} + \nabla \cdot (\rho \mathbf{u}) = 0 \quad (3.2)$$

For linear momentum balance, the same theorem can be applied to Newton's second law, as presented next [12]:

$$\frac{d}{dt} \int_V \rho \mathbf{u} dV = \oint_S \mathbf{T} \cdot \mathbf{n} dA + \int_V \rho \mathbf{g} dV$$

\mathbf{T} is the stress tensor and \mathbf{g} the gravitational field. The divergent theorem is used again on all the surface integrals, providing the equation bellow:

$$\int_V \left[\frac{\partial \rho \mathbf{u}}{\partial t} + \nabla \cdot (\rho \mathbf{u} \mathbf{u}) \right] dV = \int_V \nabla \cdot \mathbf{T} dV + \int_V \rho \mathbf{g} dV$$

Combining with Eq. (3.2), and assuming that V is a generic volume, results in:

$$\rho \left[\frac{\partial \mathbf{u}}{\partial t} + \mathbf{u} \cdot \nabla(\mathbf{u}) \right] = \nabla \cdot \mathbf{T} + \rho \mathbf{g} \quad (3.3)$$

The tensor \mathbf{T} is given by the constitutive relation, as seen in [12]:

$$\mathbf{T} = (-p_e + \kappa \nabla \cdot \mathbf{u}) \mathbf{I} + \mu \left(\nabla \mathbf{u} + (\nabla \mathbf{u})^T - \frac{2}{3} (\nabla \cdot \mathbf{u}) \mathbf{I} \right) \quad (3.4)$$

Where μ is the dynamic viscosity, p_e the equilibrium pressure, κ the expansion viscosity and \mathbf{I} the identity second order tensor. If the fluid is considered incompressible, Eq. (3.2) and Eq. (3.3) become the Navier-Stokes equations for incompressible flows, with mass continuity and momentum equations defined, respectively, as follows:

$$\nabla \cdot \mathbf{u} = 0 \quad (3.5)$$

$$\rho \left(\frac{\partial \mathbf{u}}{\partial t} + \mathbf{u} \cdot \nabla \mathbf{u} \right) = -\nabla p + \mu \nabla^2 \mathbf{u} + \rho \mathbf{g} \quad (3.6)$$

Here, p stands for pressure. The dimensionless variables for cases where a characteristic velocity and length, U and L , respectively, are identified, found in an expansion problem, are calculated as follows, where the subscript D indicates the dimensional variable:

$$\begin{aligned} \mathbf{x} &= \frac{\mathbf{x}_D}{L}, & \mathbf{u} &= \frac{\mathbf{u}_D}{U}, & t &= \frac{t_D U}{L}, & \mathbf{g} &= \frac{\mathbf{g}_D}{|\mathbf{g}_{ref}|}, & p &= \frac{p_D}{\rho U^2} \\ \kappa &= \frac{\kappa_D}{\kappa_{ref}}, & c_p &= \frac{c_{p_D}}{c_{p_{ref}}}, & \mu &= \frac{\mu_D}{\mu_{ref}}, & \rho &= \frac{\rho_D}{\rho_{ref}} \end{aligned} \quad (3.7)$$

Where the subscript ref refers to the reference variable to be considered. Replacing the dimensional values by the relations in Eq. (3.7), one may find the continuity and the momentum equations in the dimensionless form as follows:

$$\nabla \cdot \mathbf{u} = 0 \quad (3.8)$$

$$\frac{\partial \mathbf{u}}{\partial t} + \mathbf{u} \cdot \nabla \mathbf{u} = -\nabla p + \frac{1}{Re} \nabla^2 \mathbf{u} + \frac{1}{Fr^2} \mathbf{g} \quad (3.9)$$

$Re = UL/\nu$ is known as the Reynolds number and $Fr = U/\sqrt{gL}$ the Froude number. In addition, for the cases where the characteristic velocity U is not known and there is a temperature gradient ΔT responsible for convective flow, the dimensionless form of \mathbf{u} , t , T and p are given as:

$$\mathbf{u} = \frac{\mathbf{u}_D L}{\nu}, \quad t = \frac{t_D \nu}{L^2}, \quad T = \frac{T_D}{\Delta T}, \quad p = \frac{p_D L^2}{\rho \nu^2} \quad (3.10)$$

The fluid's properties in the dimensionless form for this case remain the same as the previous one. Using Eq. (3.10), one may find the dimensionless form of the continuity and momentum equation for buoyancy dominant effect, where T is the temperature, as:

$$\frac{\partial \mathbf{u}}{\partial t} + \mathbf{u} \cdot \nabla \mathbf{u} = -\nabla p + \nabla^2 \mathbf{u} + (Ga - GrT)\mathbf{g} \quad (3.11)$$

Where $Ga = gL^3/\nu^2$ is the Galileo number and $Gr = gL^3\beta\Delta T/\nu^2$ the Grashof number, with β representing the coefficient of thermal expansion. Then, the generic governing equation for an incompressible fluid phase in its vectorial and dimensionless form is given by Eq. (3.12), for which the dimensionless numbers can be adapted for each case, making $Re = 1.0$ for the convective case and $Ga = 1/Fr^2, Gr = 0$, for the expansion one.

$$\frac{\partial \mathbf{u}}{\partial t} + \mathbf{u} \cdot \nabla \mathbf{u} = -\nabla p + \frac{1}{Re} \nabla^2 \mathbf{u} + (Ga - GrT)\mathbf{g} \quad (3.12)$$

As presented by BATCHELOR [12], the energy (e) balance differential equation may be written as:

$$\rho \frac{De}{Dt} = \mathbf{T} : \nabla u + \nabla \cdot (k \nabla T) \quad (3.13)$$

Where the first term on the right hand side of the equation may be open as:

$$\mathbf{T} : \nabla u = -p_e \nabla \cdot u + \kappa (\nabla \cdot u)^2 + 2\mu \mathbf{S} : \mathbf{S} \quad (3.14)$$

With the tensor \mathbf{S} defined as:

$$\mathbf{S} = \frac{1}{2} (\nabla \mathbf{u} + (\nabla \mathbf{u})^T) - \frac{1}{3} (\nabla \cdot \mathbf{u}) \mathbf{I} \quad (3.15)$$

Here, \mathbf{I} is the identity tensor. If the fluid is considered incompressible and the parcel responsible for mechanical energy dissipation ($2\mu\mathbf{S} : \mathbf{S}$) is neglected, energy balance is reduced to:

$$\rho c_p \left[\frac{\partial T}{\partial t} + \mathbf{u} \cdot \nabla T \right] = k(\nabla^2 T) \quad (3.16)$$

Where c_p is known as the specific heat at constant pressure. Eq. (3.17) completes the system of equations, providing a correlation for energy conservation in its dimensionless form.

$$\frac{\partial T}{\partial t} + \mathbf{u} \cdot \nabla T = \frac{1}{RePr} (\nabla^2 T) \quad (3.17)$$

Here $Pr = \nu/\alpha$ is the Prandtl number. The resulted equations constitute the non-linear system of equations to be solved by means of the finite element method.

3.2 The Porous Medium

As seen in [4], the process of filtration through porous media is modeled by the linear relation between the fluid velocity and the pressure gradient in the porous region, as shown in Eq. (3.18), where the linear coefficient is expressed by a term related to the permeability coefficient, K , and the dynamic viscosity of the fluid, μ .

$$\nabla p = -\frac{\mu}{K} \mathbf{u} \quad (3.18)$$

Eq. (3.18) is known as Darcy Law, [4], which is commonly used for cases where the Reynolds number associated to the characteristic pore size, δ , shown in Eq. (3.19), is below 1.0.

$$Re_p = \frac{\rho U \delta}{\mu} \quad (3.19)$$

A general model, for any value of Re_p , is known as Forchheimer equation, [4], which accounts for the non-linear term $|\mathbf{u}|\mathbf{u}$, as shown below:

$$\nabla p = -\frac{\mu}{K}\mathbf{u} - \frac{\rho C_F}{K}|\mathbf{u}|\mathbf{u} \quad (3.20)$$

Where C_F is the inertial resistance coefficient and ρ , the fluid specific mass.

A diffusive term may also be considered, especially for highly porous media, resulting in the Brinkman-Forchheimer equation, [4]:

$$\nabla p = -\frac{\mu}{K}\mathbf{u} - \frac{\rho C_F}{K}|\mathbf{u}|\mathbf{u} + \mu\nabla^2\mathbf{u} \quad (3.21)$$

A non-linear convective term is then added to Eq. (3.21) in order to have one single formulation for an entire domain, with porous and non-porous media.

$$\rho \left(\frac{\partial \mathbf{u}}{\partial t} + \mathbf{u} \cdot \nabla \mathbf{u} \right) + \left(\frac{\mu}{K}\mathbf{u} + \frac{\rho C_F}{K}|\mathbf{u}|\mathbf{u} \right) \varepsilon = -\nabla p + \mu\nabla^2\mathbf{u} \quad (3.22)$$

Where ε is either 1 or 0, depending if the region of the domain is porous or not, respectively.

By introducing two new dimensionless numbers, the Darcy number (Da) and the Forchheimer number (Fo), defined in Eq. (3.24) and Eq. (3.25), respectively, the final dimensionless equation is obtained, as shown in Eq. (3.23).

$$\frac{\partial \mathbf{u}}{\partial t} + \mathbf{u} \cdot \nabla \mathbf{u} + \frac{1}{Re Da} (\mathbf{u} + Fo|\mathbf{u}|\mathbf{u}) \varepsilon = -\nabla p + \frac{1}{Re} \nabla^2 \mathbf{u} \quad (3.23)$$

$$Da = \frac{K}{L^2} \quad (3.24)$$

$$Fo = \frac{\rho C_F \sqrt{K} U}{\mu} \quad (3.25)$$

3.3 The Solid Phase

Following Newton's second law, particles' motion is modeled through the Lagrangian approach, as described by CROWE *et al.* [5]. Figure 3.1 shows the main forces acting on spherical body subjected to an external flow of velocity \mathbf{u} .

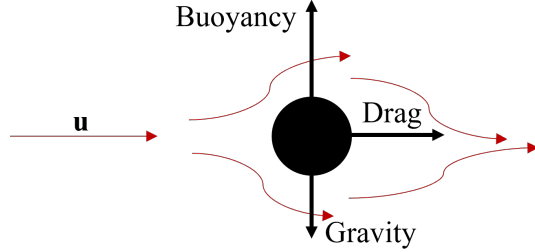


Figure 3.1: Schematic drag and buoyancy forces on a single particle in an incompressible flow that reaches the body with a velocity \mathbf{u} .

The balance between the buoyancy and gravity forces, \mathbf{F}_B , is given by Eq. (3.26) and the drag force, [5], \mathbf{F}_D , is calculated in Eq. (3.27).

$$\mathbf{F}_B = \frac{\pi}{6} D_p^3 (\rho_p - \rho_f) \mathbf{g} \quad (3.26)$$

$$\mathbf{F}_D = \frac{\pi}{8} C_D \rho_f D_p^2 |\mathbf{u}_p - \mathbf{u}| (\mathbf{u}_p - \mathbf{u}) \quad (3.27)$$

The subscripts p and f refer to particle and fluid, respectively, ρ_p and D_p are the particle's specific mass and diameter, in that order, and C_D is the drag coefficient.

Hence, Newton's second law applied to solid bodies leads to:

$$\sum \mathbf{F} = m_p \frac{d\mathbf{u}_p}{dt} \quad (3.28)$$

$$m_p \frac{d\mathbf{u}_p}{dt} = \frac{\pi}{8} C_D \rho_f D_p^2 |\mathbf{u}_p - \mathbf{u}| (\mathbf{u}_p - \mathbf{u}) + \frac{\pi}{6} D_p^3 (\rho_p - \rho_f) \mathbf{g} \quad (3.29)$$

All the geometric parameters, variables and properties are nondimensionalized with respect to the ones in the continuous phase, as follows:

$$\rho_p = \frac{\rho_{p_D}}{\rho_{f_{ref}}}, \quad \mathbf{u}_p = \frac{\mathbf{u}_{p_D}}{u_{ref}}, \quad \mathbf{u} = \frac{\mathbf{u}_D}{u_{ref}}, \quad D = \frac{D_D}{L}, \quad \mathbf{g} = \frac{\mathbf{g}_D}{|\mathbf{g}_{ref}|} \quad (3.30)$$

Thus, Eq. (3.31) represents the dimensionless form of Eq. (3.29).

$$\frac{\pi}{6}\rho_p D_p^3 \frac{d\mathbf{u}_p}{dt} = \frac{\pi}{8} C_D D_p^2 |\mathbf{u}_p - \mathbf{u}| (\mathbf{u}_p - \mathbf{u}) + Ga \frac{\pi}{6} D_p^3 (\rho_p - 1) \mathbf{g} \quad (3.31)$$

Depending on the case studied, u_{ref} can either assume the form U or ν/L . Again, when the reference velocity U is a known quantity, $Ga = 1/Fr^2$. The discretization in time, making the first term in the right-hand side F_D and the second F_B , gives:

$$\frac{\mathbf{u}_p^{n+1} - \mathbf{u}_p^n}{\Delta t} = \frac{\mathbf{F}_D + \mathbf{F}_B}{m_p} \quad (3.32)$$

Where m_p is the term in the left-hand side in Eq. (3.31), multiplying the time derivative. The correlation above consists of Newton's second law using a finite difference method, in which convergence is completely dependent on the fraction $\Delta t/m_p$. The drag coefficient is given by the Shiller and Naumann expression, [5]:

$$C_D = \frac{24}{Re_p} (1 + 0.14 Re_p^{0.687}) \quad (3.33)$$

The graphical representation of Eq. (3.33) is shown in Figure 3.2. For low particle Reynolds number, Re_p , Eq. (3.33) is approximately reduced to:

$$C_D = \frac{24}{Re_p} \quad (3.34)$$

Where the particle Reynolds number is given by:

$$Re_p = Re \frac{D_p |\mathbf{u}_p - \mathbf{u}|}{\mu} \quad (3.35)$$

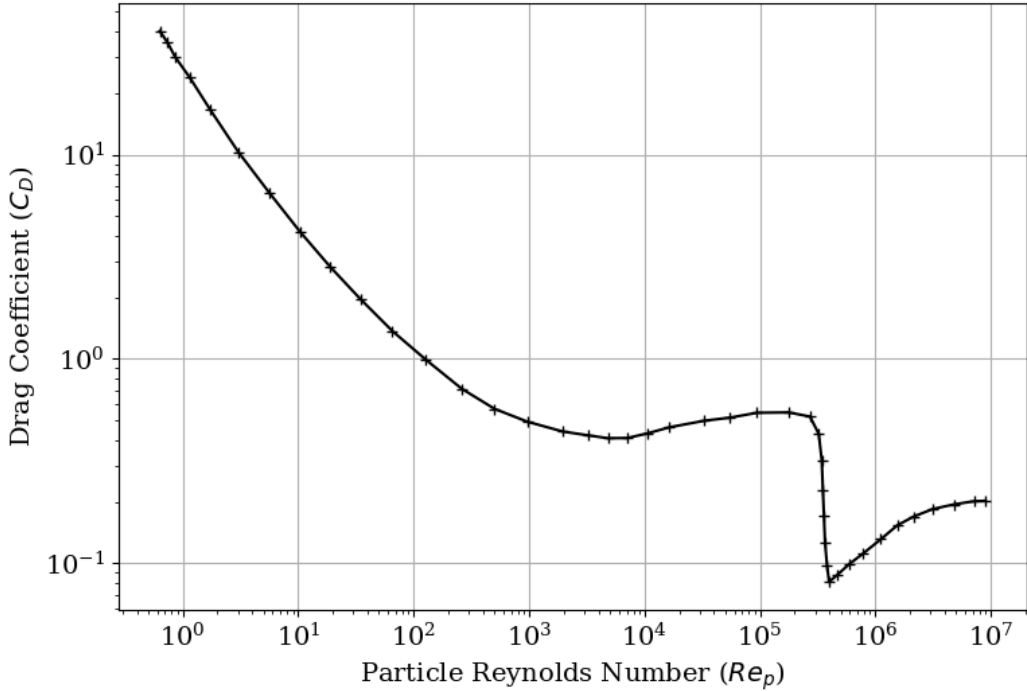


Figure 3.2: Drag coefficient as a function of Re_p , [5].

3.4 The Final Set of Differential Equations

After defining the entire formulation of the problem, the final set of differential equations to be solved by the methods presented throughout this work is:

$$\frac{D\mathbf{u}}{Dt} + \frac{1}{ReDa} (\mathbf{u} + Fo|\mathbf{u}|\mathbf{u}) \varepsilon = -\nabla p + \frac{1}{Re} \nabla^2 \mathbf{u} + (Ga - GrT)\mathbf{g} \quad (3.36)$$

$$\nabla \cdot \mathbf{u} = 0 \quad (3.37)$$

$$\frac{DT}{Dt} = \frac{1}{RePr} (\nabla^2 T) \quad (3.38)$$

$$\frac{\pi}{6} \rho_p D_p^3 \frac{d\mathbf{u}_p}{dt} = \frac{\pi}{8} C_D D_p^2 |\mathbf{u}_p - \mathbf{u}| (\mathbf{u}_p - \mathbf{u}) + Ga \frac{\pi}{6} D_p^3 (\rho_p - 1) \mathbf{g} \quad (3.39)$$

The variable ε is used as a switch between the two possible regions defined below:

- Ω_f : the region where the fluid is free to flow, following the Navier-Stokes equations;
- Ω_p : the region where a porous medium is present and the Darcy/Forchheimer equation governs the problem.

Hence, by observing Eq. (3.36), ε will assume the values of 0 in Ω_p and 1 in Ω_f .

3.4.1 General Boundary Conditions

As described by ANJOS [23], boundary conditions are important aspects to characterize differential equations, such as the ones shown in this work. A brief description of the main boundary conditions used in this work is presented next:

- No-slip condition: The velocity vector is set to null value, characterizing the fluid at rest close to walls, [23];
- Prescribed values of velocity and temperature: Generally, the inlet velocity has a known value and some boundaries may have fixed temperatures. Thus, this kind of boundary condition is used, known as Dirichlet boundary condition for velocity;
- Prescribed value of pressure: Normally set as $p = 0$ in the outflow, this condition is used to determine unknown exit conditions of the flow, as described in [23], where the velocity gradient is null (homogeneous Neumann boundary condition for velocity);
- Symmetry condition: In order to simplify more complex and yet symmetrical geometries, this boundary condition is used, in which only the normal velocity component is prescribed;
- Insulated surface: In this case, there is no heat flux from or to the exterior of the surface. Thus the temperature gradient is null (homogeneous Neumann boundary condition for temperature).

Chapter 4

The Finite Element Analysis

4.1 The Variational Form

As denoted in [24], to determine the variational form, also known as the weak formulation, two classes of functions, from the Sobolev space, must be defined for the trial solutions and the weight functions. The definitions are as follows:

$$H^1(\Omega) = \left\{ u \in L^2(\Omega), \frac{\partial u}{\partial x_i} \in L^2(\Omega), i = 1, 2, \dots, n \right\} \quad (4.1)$$

Where $L^2(\Omega)$ is the space of square-integrable functions:

$$L^2(\Omega) = \left\{ u : \Omega \rightarrow \Re, \int_{\Omega} u^2 d\Omega < \infty \right\} \quad (4.2)$$

Defining:

$$U_{\mathbf{u}_{\Gamma}}(\Omega) = \left\{ \mathbf{u} \in H^1 : \mathbf{u} = \mathbf{u}_{\Gamma} \text{ in } \Gamma_1 \right\} \quad (4.3)$$

$$P_{p_{\Gamma}}(\Omega) = \left\{ p \in H^1 : p = p_{\Gamma} \text{ in } \Gamma_2 \right\} \quad (4.4)$$

$$\tau_{T_{\Gamma}}(\Omega) = \left\{ T \in H^1 : T = T_{\Gamma} \text{ in } \Gamma_3 \right\} \quad (4.5)$$

Where Γ_1 , Γ_2 and Γ_3 are, respectively, the boundaries for velocity, pressure and temperature.

Thus, the weak form is obtained by multiplying each of the governing equation by the weight functions \mathbf{w} , q and r , associated with velocity, pressure and temperature, respectively, whose spaces are defined as:

$$W_{\mathbf{w}_\Gamma}(\Omega) = \{\mathbf{w} \in H^1 : \mathbf{w} = 0 \quad \text{in} \quad \Gamma_1\} \quad (4.6)$$

$$Q_{r_\Gamma}(\Omega) = \{q \in H^1 : q = 0 \quad \text{in} \quad \Gamma_2\} \quad (4.7)$$

$$R_{r_\Gamma}(\Omega) = \{r \in H^1 : r = 0 \quad \text{in} \quad \Gamma_3\} \quad (4.8)$$

The formulation is, then, transformed into the equations below:

$$\begin{aligned} \int_{\Omega} \frac{D\mathbf{u}}{Dt} \cdot \mathbf{w} d\Omega &= - \int_{\Omega} \nabla p \cdot \mathbf{w} d\Omega + \frac{1}{Re} \int_{\Omega} (\nabla^2 \mathbf{u}) \cdot \mathbf{w} d\Omega \\ &\quad + \int_{\Omega} Gag \cdot \mathbf{w} d\Omega - \int_{\Omega} GrT \mathbf{g} \cdot \mathbf{w} d\Omega \end{aligned} \quad (4.9)$$

$$\int_{\Omega} q \nabla \cdot \mathbf{u} d\Omega = 0 \quad (4.10)$$

$$\int_{\Omega} \frac{DT}{Dt} r d\Omega = \frac{1}{RePr} \int_{\Omega} (\nabla^2 T) r d\Omega \quad (4.11)$$

The Green theorem, [24], is applied to the following terms:

$$\int_{\Omega} (\nabla^2 \mathbf{u}) \cdot \mathbf{w} d\Omega = - \int_{\Omega} (\nabla \mathbf{u} : \nabla \mathbf{w}) d\Omega + \int_{\Gamma} (\mathbf{w} \cdot \nabla \mathbf{u} \cdot \mathbf{n}) d\Gamma \quad (4.12)$$

$$\int_{\Omega} (\nabla^2 T) r d\Omega = - \int_{\Omega} (\nabla T \cdot \nabla r) d\Omega + \int_{\Gamma} (r \nabla T \cdot \mathbf{n}) d\Gamma \quad (4.13)$$

$$\int_{\Omega} \nabla p \cdot \mathbf{w} d\Omega = - \int_{\Omega} p \nabla \cdot \mathbf{w} d\Omega + \int_{\Gamma} (p \mathbf{w} \cdot \mathbf{n}) d\Gamma \quad (4.14)$$

Since, in this work, all boundary conditions are either Dirichlet or homogeneous Neumann and the prescribed pressure is null, the final variational form is given by:

$$\begin{aligned} \int_{\Omega} \frac{D\mathbf{u}}{Dt} \cdot \mathbf{w} d\Omega &= \int_{\Omega} p \nabla \cdot \mathbf{w} d\Omega - \frac{1}{Re} \int_{\Omega} (\nabla \mathbf{u} : \nabla \mathbf{w}) d\Omega \\ &\quad + \int_{\Omega} G \mathbf{a} \mathbf{g} \cdot \mathbf{w} d\Omega - \int_{\Omega} G r T \mathbf{g} \cdot \mathbf{w} d\Omega \end{aligned} \quad (4.15)$$

$$\int_{\Omega} q \nabla \cdot \mathbf{u} d\Omega = 0 \quad (4.16)$$

$$\int_{\Omega} \frac{DT}{Dt} r d\Omega = -\frac{1}{RePr} \int_{\Omega} (\nabla T \cdot \nabla r) d\Omega \quad (4.17)$$

4.2 The Galerkin Method

The Galerkin Method, [24], consists of an approximation of the continuous variable to a discrete representation. Then, the shape functions, N_i , are used, in order to interpolate the values in the nodes seen in Figure 4.1, for the MINI and the quadratic elements, where i and j are the local number of the point, corresponding to the global value k .

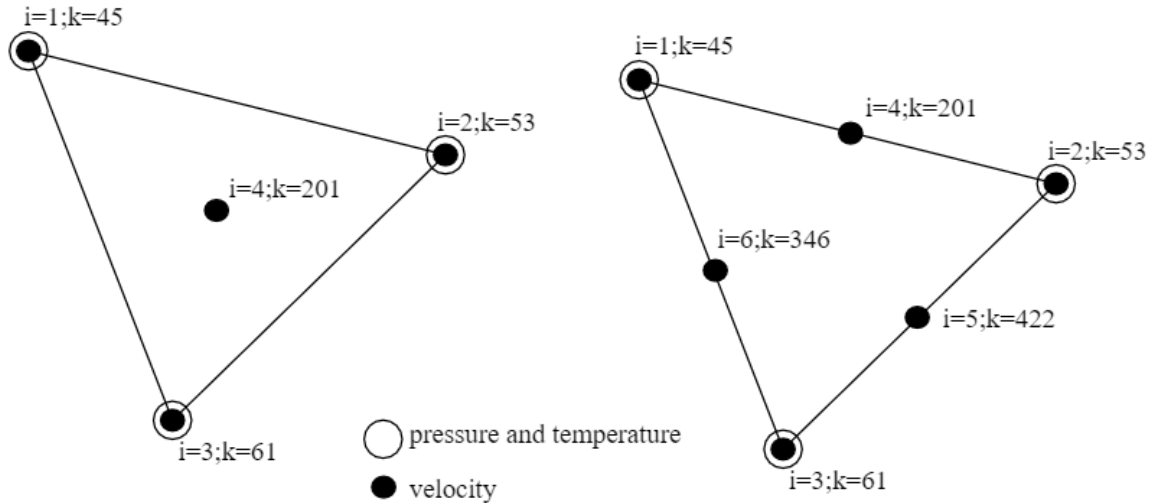


Figure 4.1: Element's nodes representation, with local (i) and respective global (k) numbers, for the MINI (left) and quadratic (right) kinds. The scheme also denotes the points where pressure, temperature and velocity are calculated.

Given the element, it is composed by a total of NP points, for which the velocities u and v are calculated, and NV vertices, where pressure and temperature are associated. The difference between the two is that NV does not account for the centroid, in the MINI element, or the mid-points, in the quadratic one, seen in Figure 4.1. The total values of vertices and points in the mesh are referred to as NV_{total} and NP_{total} , respectively. For each element, the variables and weight functions may be approximated by:

$$u \approx \sum_{i=1}^{NP} N_i(x, y) u_i, \quad v \approx \sum_{i=1}^{NP} N_i(x, y) v_i, \quad p \approx \sum_{i=1}^{NV} L_i(x, y) p_i, \quad T \approx \sum_{i=1}^{NV} L_i(x, y) T_i$$

$$\mathbf{w} \approx \sum_{j=1}^{NP} N_j(x, y) \mathbf{w}_j, \quad q \approx \sum_{j=1}^{NV} L_j(x, y) q_j, \quad r \approx \sum_{j=1}^{NV} L_j(x, y) r_j$$

Where the shape functions N_i of the MINI element, for $i = 1, 2, 3$, are determined by:

$$N_i = L_i - 9L_1L_2L_3, \quad i = 1, 2, 3$$

$$N_4 = 27L_1L_2L_3$$

As for the quadratic elements, the shape functions are defined as:

$$N_i = (2L_i - 1)L_i, \quad i = 1, 2, 3$$

$$N_4 = 4L_1L_2, \quad N_5 = 4L_2L_3, \quad N_6 = 4L_1L_3$$

The L_i terms, for $i = 1, 2, 3$, are the linear element's shape functions, calculated by means of the barycentric coordinate system. Therefore, the elements used in this work, called MINI and quadratic, are from the Taylor-Hood family and the first one represents the most simple triangular element that satisfies the Ladyzhenskaya–Babuška–Brezzi (LBB) condition, [23], so that no artificial stability is added

to the Navier-Stokes equations. For the base element, in the (L_1, L_2) coordinate system , shown in Figure 4.2, the appropriate shape functions are shown in Figures 4.3 and 4.4 for the MINI and quadratic kinds, respectively.

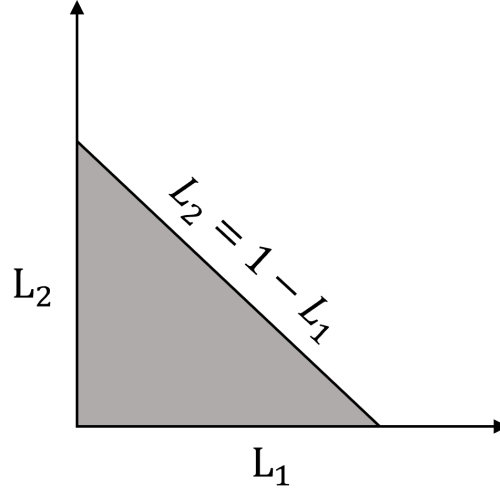


Figure 4.2: Base element in the (L_1, L_2) coordinate system. This coordinate system is chosen to coincide with the linear element's shape functions, denominated L_1 , L_2 and $L_3 = 1 - L_1 - L_2$.

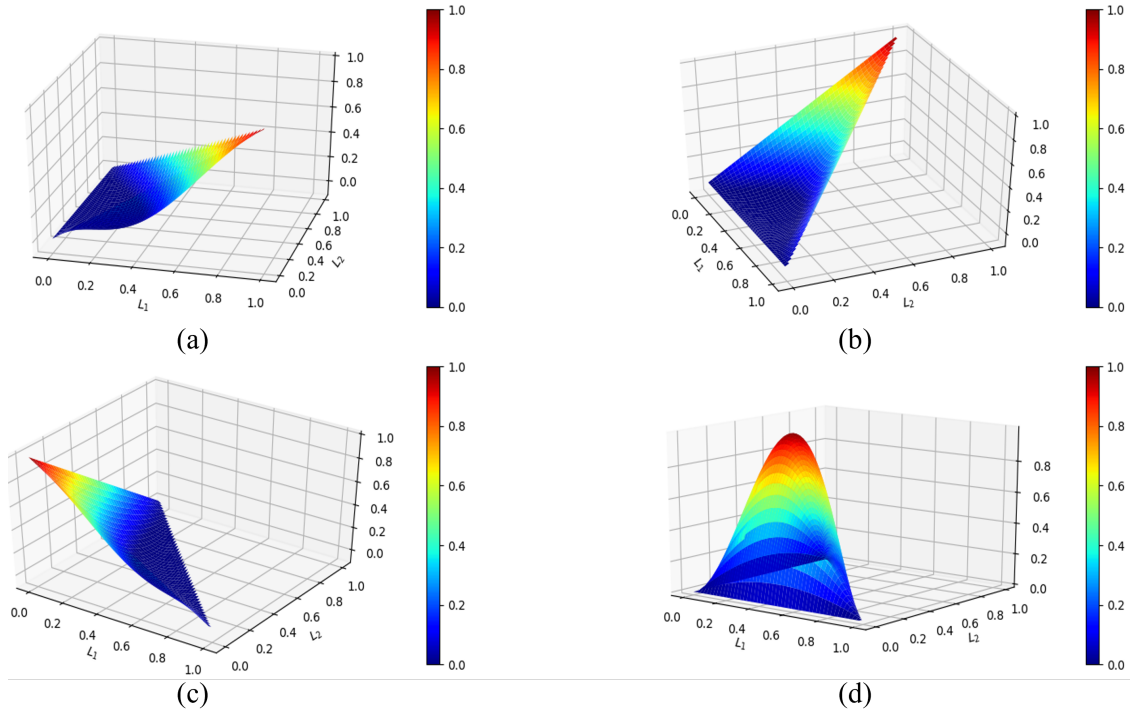


Figure 4.3: MINI element shape functions, (a) N_1 , (b) N_2 , (c) N_3 , (d) N_4 , as functions of L_1 and L_2 , the coordinate system of the base triangle.

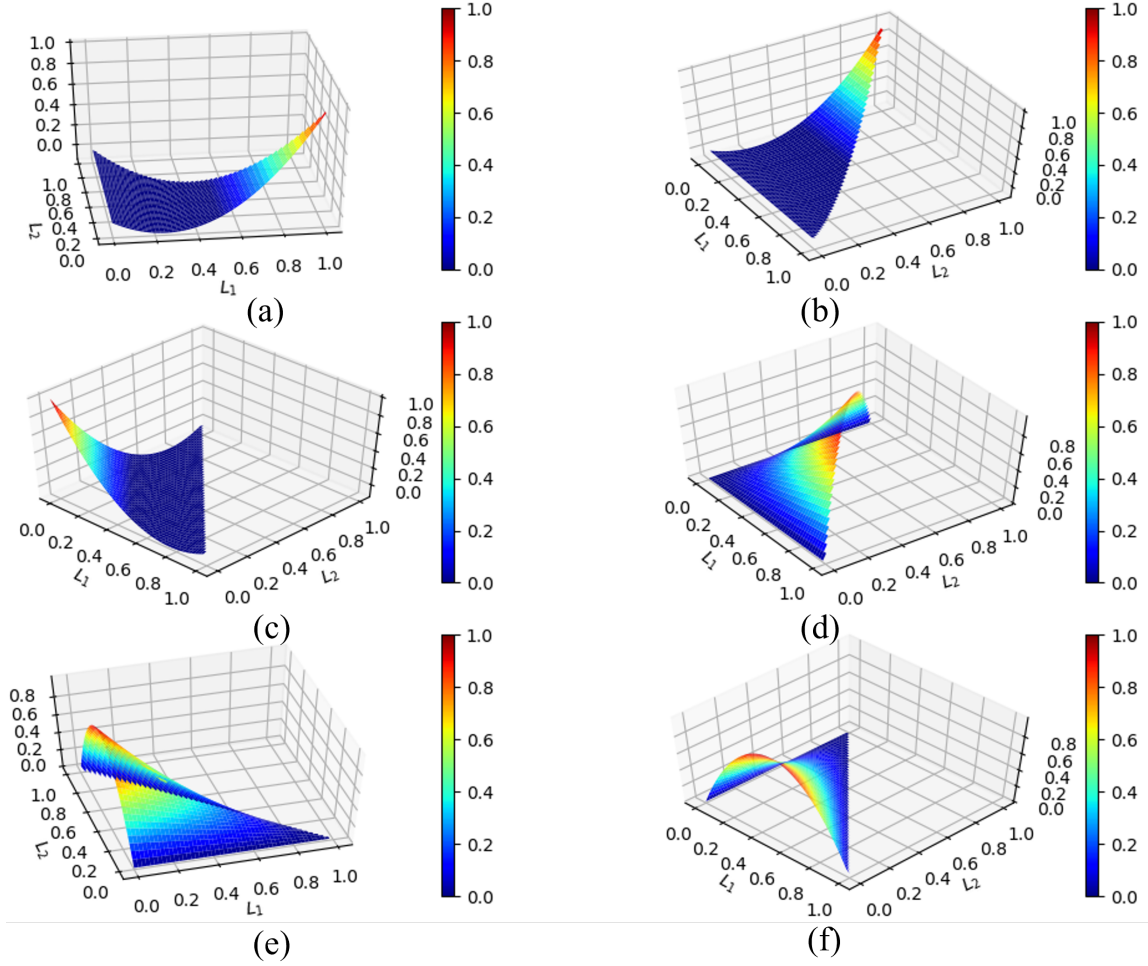


Figure 4.4: Quadratic element shape functions, (a) N_1 , (b) N_2 , (c) N_3 , (d) N_4 , (e) N_5 , (f) N_6 , as functions of L_1 and L_2 , the coordinate system of the base triangle.

Substituting the approximated variables, as well as the weight functions approximated form, into the governing equations and using the index notation leads to:

$$\begin{aligned} \sum_e \int_{\Omega_e} \frac{DN_i u_i}{Dt} N_j w_{x_j} d\Omega - \sum_e \int_{\Omega_e} \frac{\partial N_i w_{x_i}}{\partial x} L_j p_j d\Omega + \frac{1}{Re} \sum_e \int_{\Omega_e} (\nabla N_i u_i \cdot \nabla N_j w_{x_j}) d\Omega \\ - \sum_e \int_{\Omega_e} G a N_i g_{x_i} N_j w_{x_j} d\Omega + \sum_e \int_{\Omega_e} G r N_i T_i^+ g_x N_j w_{x_j} d\Omega = 0 \quad (4.18) \end{aligned}$$

$$\begin{aligned} \sum_e \int_{\Omega_e} \frac{DN_i v_i}{Dt} N_j w_{y_j} d\Omega - \sum_e \int_{\Omega_e} \frac{\partial N_i w_{y_i}}{\partial y} L_j p_j d\Omega + \frac{1}{Re} \sum_e \int_{\Omega_e} (\nabla N_i v_i \cdot \nabla N_j w_{y_j}) d\Omega \\ - \sum_e \int_{\Omega_e} G a N_i g_{y_i} N_j w_{y_j} d\Omega + \sum_e \int_{\Omega_e} G r N_i T_i^+ g_y N_j w_{y_j} d\Omega = 0 \quad (4.19) \end{aligned}$$

$$\sum_e \left(\int_{\Omega_e} L_i q_i \frac{\partial N_j u_j}{\partial x} d\Omega + \int_{\Omega_e} L_i q_i \frac{\partial N_j v_j}{\partial y} d\Omega \right) = 0 \quad (4.20)$$

$$\sum_e \left(\int_{\Omega_e} \frac{DL_i T_i}{Dt} L_j r_j d\Omega + \frac{1}{RePr} \int_{\Omega_e} (\nabla L_i T_i \cdot \nabla L_j r_j) d\Omega \right) = 0 \quad (4.21)$$

The term T^+ is the temperature interpolated at the centroid or mid-point nodes of the elements, by interpolating the temperature values in the vertices, using the respective shape functions of each element. Since the weight functions appear on both sides of each respective equation, they may be eliminated. Grouping and rearranging the terms, the matrices of the linear systems are presented as follows:

$$\begin{aligned} M_{ij} &= \sum_e \left(\int_{\Omega_e} N_i N_j d\Omega \right), & K_{ij} &= \sum_e \left(\int_{\Omega_e} \nabla N_i \cdot \nabla N_j d\Omega \right) \\ G_{x_{ij}} &= \sum_e \left(\int_{\Omega_e} \frac{\partial N_i}{\partial x} L_j d\Omega \right), & G_{y_{ij}} &= \sum_e \left(\int_{\Omega_e} \frac{\partial N_i}{\partial y} L_j d\Omega \right) \\ M_{ij}^* &= \sum_e \left(\int_{\Omega_e} L_i L_j d\Omega \right), & K_{ij}^* &= \sum_e \left(\int_{\Omega_e} \nabla L_i \cdot \nabla L_j d\Omega \right) \end{aligned}$$

Finally, the coupled linear system for pressure and velocity, in matrix form, may be written as:

$$\{\mathbf{M}\} \frac{D\{\mathbf{u}\}}{Dt} + \frac{1}{Re} \{\mathbf{K}\} \{\mathbf{u}\} - \{\mathbf{G}_x\} \{\mathbf{p}\} = Ga\{\mathbf{M}\} \{\mathbf{g}_x\} - Gr\{\mathbf{M}\} \{\mathbf{T}^+\} g_x \quad (4.22)$$

$$\{\mathbf{M}\} \frac{D\{\mathbf{v}\}}{Dt} + \frac{1}{Re} \{\mathbf{K}\} \{\mathbf{v}\} - \{\mathbf{G}_y\} \{\mathbf{p}\} = Ga\{\mathbf{M}\} \{\mathbf{g}_y\} - Gr\{\mathbf{M}\} \{\mathbf{T}^+\} g_y \quad (4.23)$$

$$\{\mathbf{D}_x\} \{\mathbf{u}\} + \{\mathbf{D}_y\} \{\mathbf{v}\} = 0 \quad (4.24)$$

Where $\mathbf{D}_x = \mathbf{G}_x^T$ and $\mathbf{D}_y = \mathbf{G}_y^T$. The temperature is calculated from a separate linear system, as follows:

$$\{\mathbf{M}^*\} \frac{D\{\mathbf{T}\}}{Dt} + \frac{1}{RePr} \{\mathbf{K}^*\} \{\mathbf{T}\} = 0 \quad (4.25)$$

4.3 The Semi-Lagrangian Formulation

After discretizing the spacial derivatives through the finite element method, time derivatives must be discretized as well. Since the material derivative of the velocity results in a non-linear term, a lagrangian approach for that term is used, considering a generic variable ψ , that can either be u , v or T . The Lagrangian formulation is, then:

$$\frac{D\psi}{Dt} \approx \frac{\psi - \psi_d}{\Delta t} \quad (4.26)$$

Where the subscript d denotes the variable's value at the previous time step in the location the fluid particle occupied (x_d) at the previous time step. Figure 4.5 explicits how the semi-lagrangian method is made for one arbitrary node.

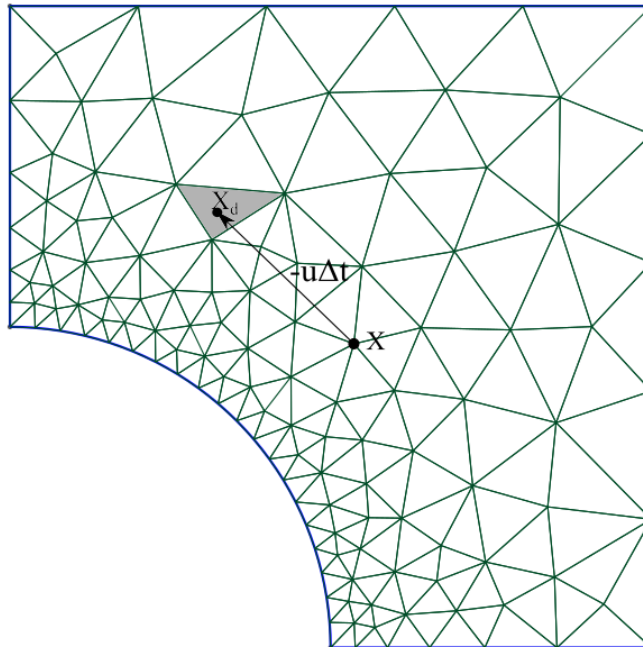


Figure 4.5: Scheme of the semi-lagrangian formulation showing how the position \mathbf{x}_d , at the previous time step t_d , is determined. The vector $-\mathbf{u}\Delta t$ is used for said calculation, where \mathbf{u} is the velocity of the fluid particle located at the position \mathbf{x} of the node.

After determining the position $\mathbf{x}_d = \mathbf{x} - \mathbf{u}\Delta t$, where \mathbf{u} is the fluid velocity and \mathbf{x} , the mesh node's position, the variables u_d , v_d and T_d are calculated by means of the interpolation of such variables' values in the points of the element that contains the fluid particle at time t_d . For u and v , an extra step is taken, that consists in interpolating the values found in the vertices for the centroids, in the case of the MINI elements, or mid-points, for the quadratic ones.

A search algorithm was built in order to optimize the element mapping to find where the position \mathbf{x}_d is located in the mesh, by calculating nearest distances from \mathbf{x}_d to the neighbor points' coordinates. Such step is repeated in a loop, for each point in the mesh, until all the \mathbf{x}_d positions are attributed to their respective containing element. The implemented algorithm has the ability to handle possible unwanted phenomena, such as when the point determined at time t_d , with coordinate \mathbf{x}_d , is outside the domain. In that case, the nearest point to the one located at \mathbf{x}_d will be located in the boundary after at least three iterations, leading to the conclusion that \mathbf{x}_d does not belong to the domain and, therefore, the nearest boundary values will be attributed to this point. Another optimization implemented is with respect to points located on the walls of the domain, where the no-slip condition is imposed ($\mathbf{u} = 0$). In this case, the semi-Lagrangian step is skipped for said points, as well as for the ones located in an in-flow boundary, where the velocity is constant.

Finally, the main system of equations, with respect to velocities and pressure, is fully determined:

$$\begin{bmatrix} \frac{\mathbf{M}}{\Delta t} + \frac{\mathbf{K}}{Re} & \mathbf{0} & -\mathbf{G}_x \\ \mathbf{0} & \frac{\mathbf{M}}{\Delta t} + \frac{\mathbf{K}}{Re} & -\mathbf{G}_y \\ \mathbf{D}_x & \mathbf{D}_y & \mathbf{0} \end{bmatrix} \begin{bmatrix} u \\ v \\ p \end{bmatrix} = \begin{bmatrix} \frac{\mathbf{M}}{\Delta t} u_d + Ga\mathbf{M}g_x - Gr\mathbf{M}T^+g_x \\ \frac{\mathbf{M}}{\Delta t} v_d + Ga\mathbf{M}g_y - Gr\mathbf{M}T^+g_y \\ \mathbf{0} \end{bmatrix} \quad (4.27)$$

The total dimensions of the matrix at the left-hand side is, therefore, $(2NP_{total} + NV_{total}) \times (2NP_{total} + NV_{total})$. Similarly, the temperature system, with dimensions $NV_{total} \times NV_{total}$, is set to be as follows:

$$\left[\begin{array}{c} \frac{1}{\Delta t} \mathbf{M}^* + \frac{1}{RePr} \mathbf{K}^* \\ \end{array} \right] \left[\begin{array}{c} T \\ \end{array} \right] = \left[\begin{array}{c} \frac{1}{\Delta t} \mathbf{M}^* T_d \\ \end{array} \right] \quad (4.28)$$

After building the assembly, the Dirichlet boundary conditions are imposed to the system and the final solution is calculated.

The formulation presented in this section for non-porous media, using the Navier-Stokes formulation can be easily adapted for porous or mixed flows by modifying the left-hand side of Eq. (4.27) as follows:

$$\left[\begin{array}{ccc} \frac{\mathbf{M}}{\Delta t} + \frac{\mathbf{K}}{Re} + \frac{\mathbf{M}}{ReDa} (\mathbf{I} + Fo\mathbf{U}) \varepsilon & \mathbf{0} & -\mathbf{G}_x \\ \mathbf{M} & \frac{1}{\Delta t} + \frac{\mathbf{K}}{Re} + \frac{\mathbf{M}}{ReDa} (\mathbf{I} + Fo\mathbf{U}) \varepsilon & -\mathbf{G}_y \\ \mathbf{D}_x & \mathbf{D}_y & \mathbf{0} \end{array} \right] \quad (4.29)$$

Here, \mathbf{U} and ε are the diagonal matrices of the modulus of the velocity at the previous time step and the ε values, respectively, in each point of the discrete domain, and \mathbf{I} , the identity matrix of order $NP_{total} \times NP_{total}$. The right-hand side of the system of equations remains unaltered.

The complexity of the integrals that define the block matrices seen above depends on the type of element used. In this work, the analytical solution for the MINI element was compared to the numerical one, using the Gaussian Quadrature, [25]. Although the accuracy of the numerical method was high, approaching to the values obtained analytically, the computational cost was considerably higher. Thus for this element, the analytical solution was used.

As for the quadratic elements, the complexity of the element required the use of the same numerical method, that had been proven to be accurate for the previous element. Even with a higher computational cost, a quadratic element is preferable over the MINI element, due to numerical diffusivity reduction, providing better results.

Chapter 5

Computational Implementation

5.1 Code Organization

The computational implementation of the Finite Element Method solver is made by means of the programming language *Python*, [6]. Said language is a script-type language and provides several advantages among others, due to its simplicity in implementation and robust Object Oriented Programming (OOP) features. *Python* also has a variety of packages that provide efficient linear algebra calculations and graphical features with libraries like *Numpy*, *Scipy*, *Matplotlib* and *PyQt*, among others.

The entire structure of the code was made using OOP, making possible its easy adaptation to improvements, such as the Darcy/Forchheimer inclusion. Figure 5.1 shows how the class hierarchy was thought and implemented.

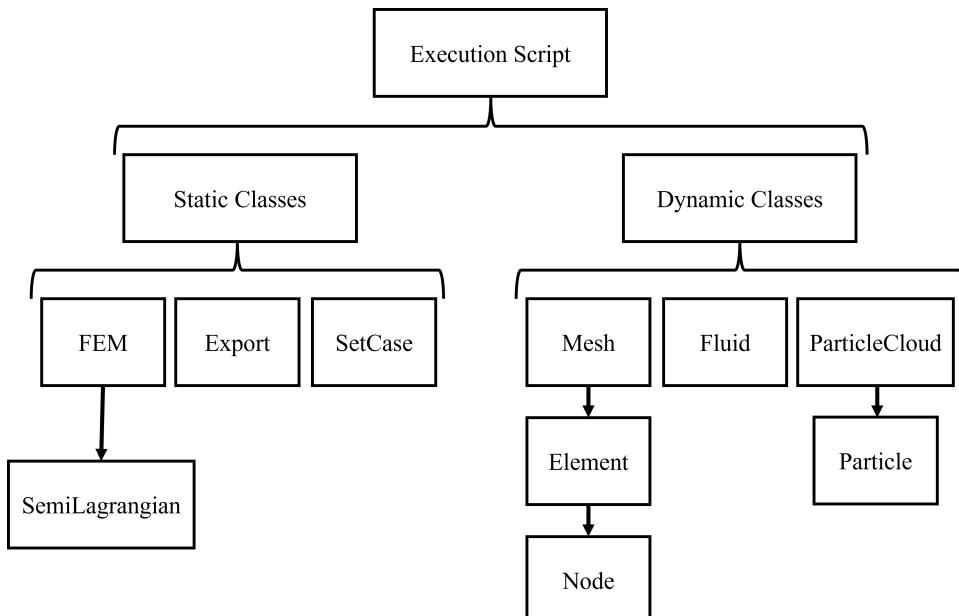


Figure 5.1: Chart representing the classes in the code implementation using Object Oriented Programming (OOP) in *Python*, [6].

A brief summary of each main classes presented above, as well as how they interact. is presented next:

- **FEM** is a static class where the entire Finite Element Method is implemented. All the global matrices are built and contour and initial conditions are applied. The system of equations is then solved.
- **SemiLagrangian** contains the semi-lagrangian formulation used by the **FEM** class to calculate time derivatives for u and T .
- **Export** is the class used to export results of all fields and particles in the *.vtk* format to be post-processed.
- **SetCase** is responsible for receiving the input parameters, initial and boundary conditions, that are given via an *.xml* file. It also loads specific *.vtk* with the fields if the initial condition is set to be from a specific time step other than the initial one.
- **Mesh** class loads the *.msh* file generated in the software *Gmsh* and generates the structures necessary to be received by the **FEM** class. It also builds lists of nodes and elements.
- **Element** is designed to receive all the information regarding each element of the mesh, such as nodes, centroids and other neighbor elements.
- **Node** is similar to the element class, but stores information related to each node in the mesh, including the elements it belongs to.
- **Fluid** objects receive not only fluid parameters, like dimensionless numbers, but also the lists of field values for each time step, such as velocity, temperature and pressure.
- **ParticleCloud** is responsible for storing all the parameters related to particles and create a list of **Particle** objects. It also determines, for each time step, the element where each particle occupies.
- **Particle** takes each particle's characteristics, like diameter, density, position and velocity.

The *.msh* file, to be loaded by the **Mesh** class is obtained through the open source software *Gmsh*. An example of mesh can be seen in Figure 5.2.

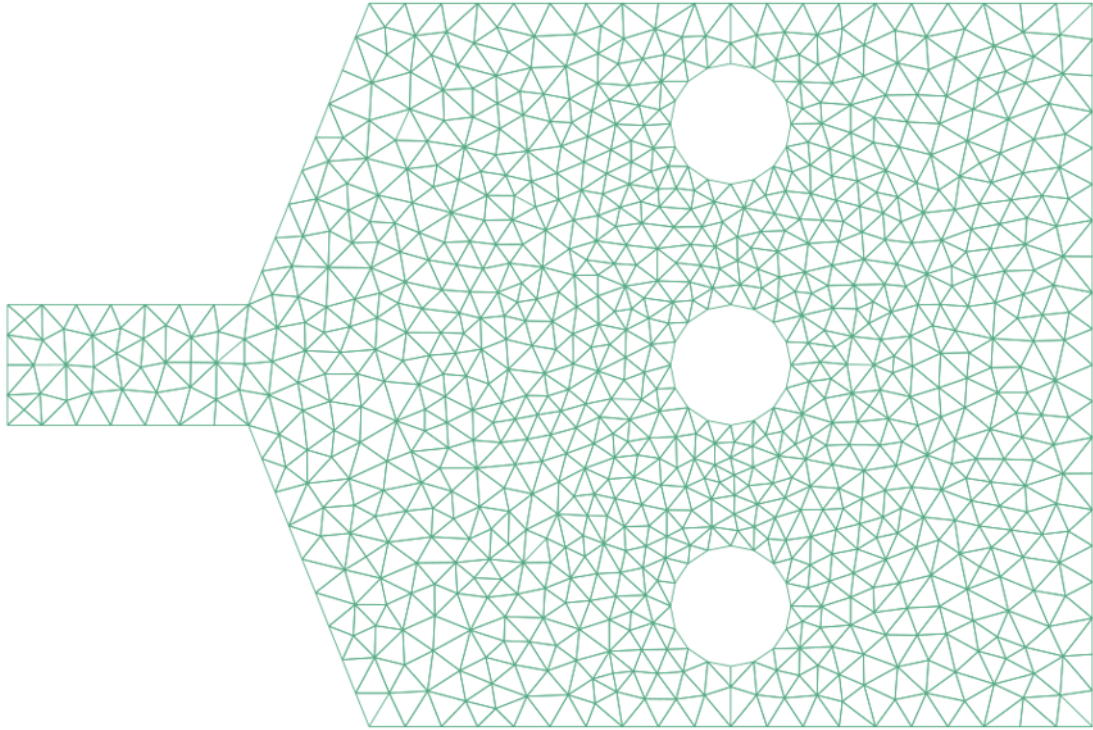


Figure 5.2: Unstructured mesh of a complex geometry containing 1626 elements and 883 vertices from *Gmsh*.

All the inputs of the simulation are defined in an *.xml* file and an example is shown in Figure 5.3.

```
<?xml version="1.0" ?>
<Case name="poiseuille">
  <Parameters Fr="100" Re="228" Gr="0" Pr="0.7" Fr_flag="True" particles="True"/>
  <BoundaryCondition>
    <Boundary name="wall" vx="0" vy="0" p="None" T="0"/>
    <Boundary name="outFlow" vx="None" vy="None" p="0" T="None"/>
    <Boundary name="inFlow" vx="1" vy="0" p="None" T="1"/>
  </BoundaryCondition>
  <OutFlow>
    <OF name="outFlow"/>
  </OutFlow>
  <InitialCondition vx="0" vy="0" p="0" T="0"/>
</Case>
```

Figure 5.3: Input example from *.xml* file showing parameters and boundary conditions for the analyzed case. The mesh used is shown in the parameter called "name".

An example of the solver calling from command line for an initial time step of 10, an end time step of 100 and an interval of 0.1 is shown below:

```
FEMsolver -i 10 -e 100 -t 0.1 -f "Cases/poiseuille/poiseuille.xml"
```

5.2 The Graphical User Interface (GUI)

A Graphical User Interface (GUI) was developed to help with *.xml* file manipulation, such as saving and loading features implementations that enhance user experience. Users may run the GUI version and either fill up all the text boxes corresponding to parameters, mesh file's path and boundary conditions or load them from a previously saved simulation. Figure 5.4 shows the software main tab.

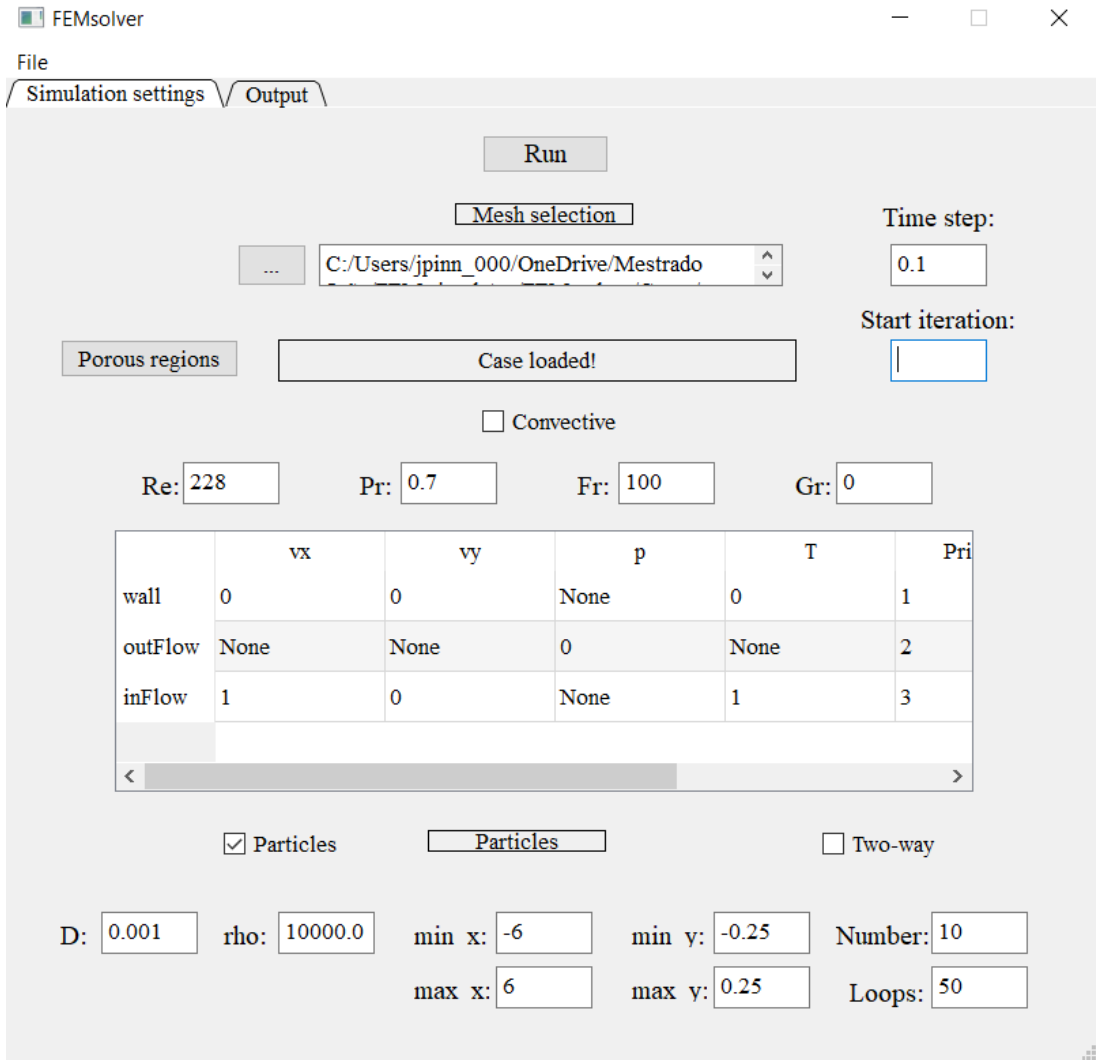


Figure 5.4: Graphical User Interface (GUI) main tab, where all simulation parameters can be set, as well as boundary conditions. Both can be saved in a *.xml* file and loaded to this tab.

Since the library *PyQt* was used, the software is cross-platform, which means it can be run in different operational systems, like Windows and Linux.

When the "Run" button is hit, the simulation starts and goes on until the "Stop" button, now replacing the "Run", is pressed. As soon as the first results are generated, the simulation can be watched in real time by switching to the "Output" tab

on the top left corner of the main window. An example of simulation is shown in Figure 5.5.

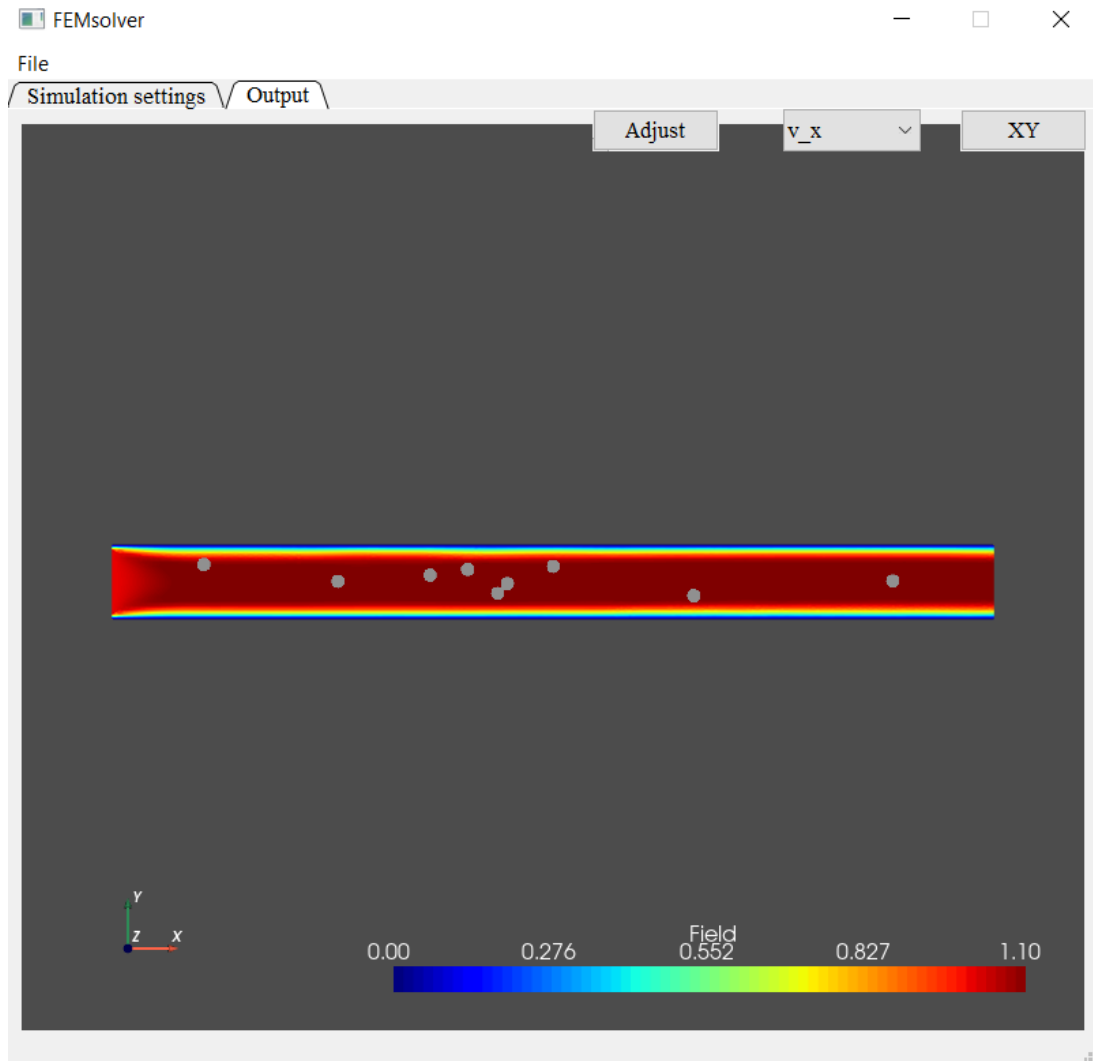


Figure 5.5: Graphical User Interface (GUI) output tab, where the real-time simulation can be observed. In this example, a Poiseuille flow with particles is being run.

The buttons to the upper right corner of the tab are for scale adjustment, field selection and normal plane selection. Thus, even though the data can be analyzed in a software like *Paraview* afterwards, preliminary analysis can be made beforehand with this tool.

Chapter 6

Verification and Physical Analysis

The implementation was made and run using an Intel(R) Core i7-4510U processor, with 8.0 GB RAM. A mesh with 2000 MINI elements in average took about 2 s/iteration to run in said device, while the quadratic mesh, with the same number of elements would take about 3.5s/iteration. The initial results are presented next.

6.1 The Lid-driven Cavity

This common CFD problem consists in a cavity, where the upper boundary moves with constant horizontal velocity. This induces a velocity field along the cavity, for $Re = 100$. For this case $Gr = 0$ and $Ga = 1/Fr^2 = 10^{-4}$, where $Fr = U/\sqrt{gL}$ is the Froude number. The mesh used has 2744 quadratic elements and 5625 points. Figure 6.1 shows the boundary conditions for this case, considering that the fluid starts at completely null velocity field, with a characteristic length $L = h$.

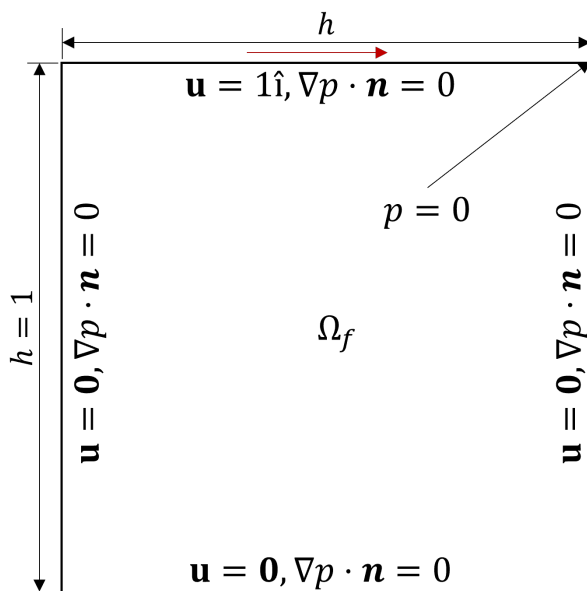


Figure 6.1: Boundary conditions for the lid-driven cavity problem, for $Re = 100$.

Since all pressure boundary conditions are of the type homogeneous Neumann, a reference point must be assigned with a value, like $p = 0$.

The simulated results for horizontal and vertical velocities are shown in Figure 6.2.

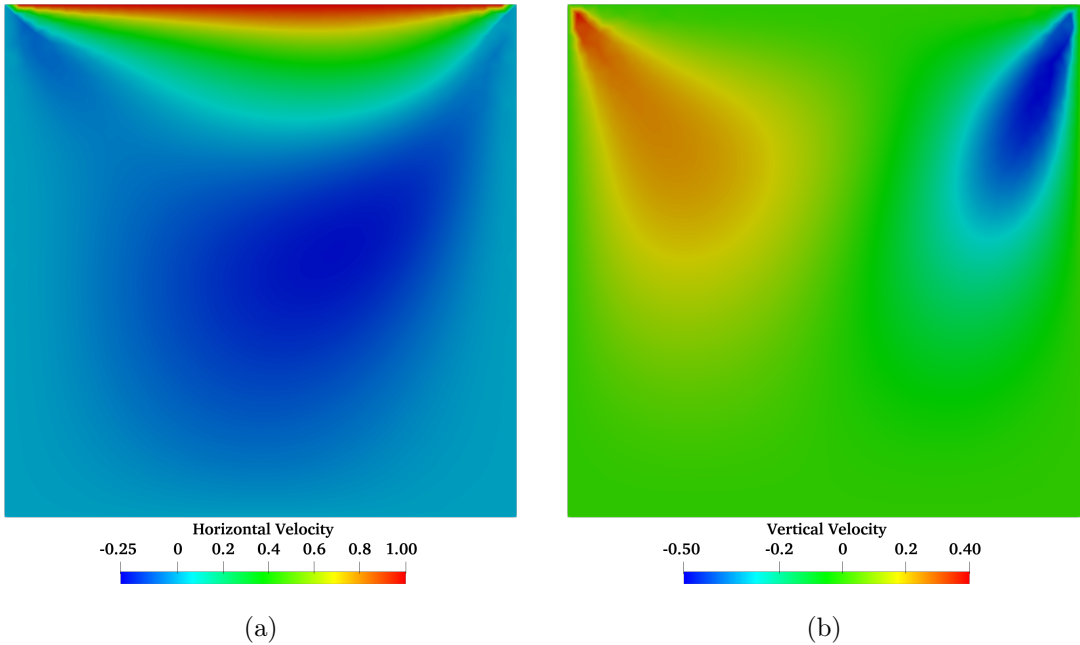


Figure 6.2: Velocity fields in the (a) horizontal and (b) vertical directions for the lid-driven cavity problem, for $Re = 100$.

The velocity fields along the vertical and horizontal lines that pass through the midpoint of the square domain are compared to the results seen in [7]. Figure 6.3 shows the comparison between the current work, using MINI and quadratic elements, and the literature.

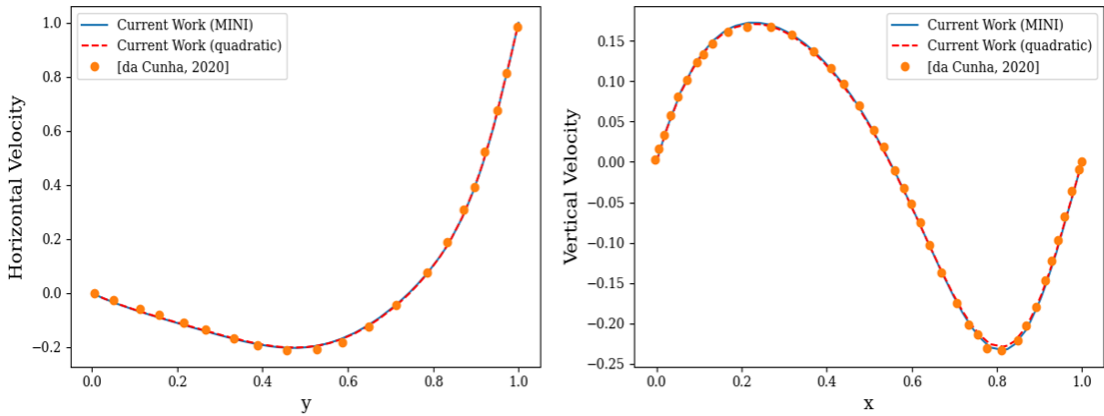


Figure 6.3: Verification of the lid-driven cavity problem, for $Re = 100$, with [7].

The result presented is double-validated, since DA CUNHA [7] also validates his simulation with the literature, and shows that the implementation in this work was

adequate, for both kinds of elements. The ideal number of elements was obtained with a mesh convergence analysis based on the maximum vertical velocity:

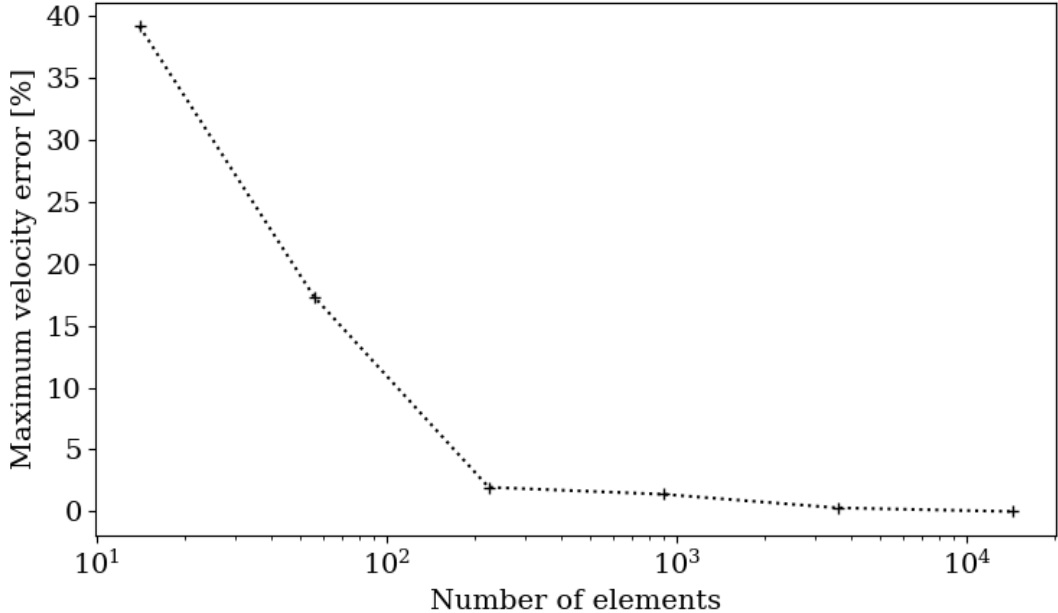


Figure 6.4: Mesh convergence analysis for the lid-driven cavity problem, doubling the size of the mesh at each analysis. Mesh convergence analysis is useful to determine the ideal number of elements in the mesh, avoiding computational processing waste.

6.2 The Backward-facing Step Problem

The next common case known in the literature is the Backward-facing Step, where the fluid enters in a fully developed regime into the entry channel, which is the Poiseuille profile, as shown in [9]. In Figure 6.5, the scheme of the domain and boundary conditions is shown, where the velocity profile is given by:

$$\mathbf{u} = u_m \left[1 - \left(\frac{2y}{h} \right)^2 \right] \hat{\mathbf{i}} \quad (6.1)$$

Where u_m is the maximum velocity in the fully developed regime, with y ranging from $-h/2$ to $h/2$. For the Poiseuille problem [12], such value is calculated as:

$$u_m = \frac{3}{2} u_0 \quad (6.2)$$

Here, u_0 is the average velocity, corresponding to the inviscid flow velocity with the same mass flow rate as this one.

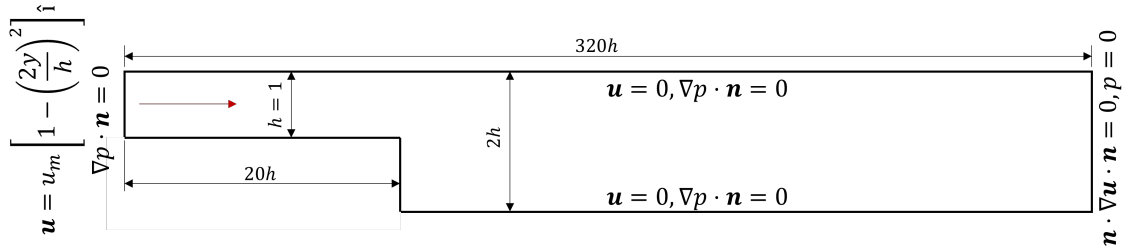


Figure 6.5: Boundary conditions for the backward-facing step problem.

The results were evaluated and compared to the ones obtained by ERTUK [9], for a Reynolds number of 800. Figure 6.6 shows the horizontal velocity field along with the stream lines for when the permanent regime is reached for part of the entire domain considered. A 164311 element mesh was used in the same domain used in [9], with a time step of 0.01.

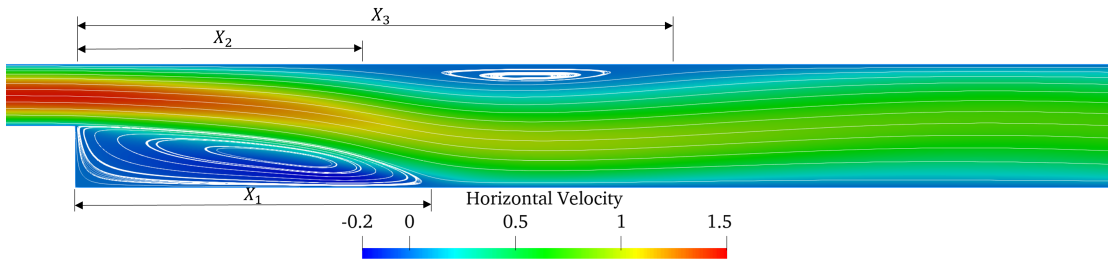


Figure 6.6: Horizontal velocity field and stream lines for the backward-facing step problem, for $Re = 800$. The recirculation positions, X_1, X_2 and X_3 , are also shown.

As can be seen, the fluid goes down the backward-facing step and, in order to obey mass conservation, the maximum velocity is reduced by the end of the channel, with a bigger cross-sectional area. Two recirculation zones are observed, as predicted in [9], for a Reynolds number as high as 800. It is noticeable that, for regions that are located away from the step, the flow resembles a Poiseuille profile. Although qualitatively the stream lines seem adequate, with two recirculation zones, the lengths diverge from the ones found in [9]. Table 6.1 shows the comparison.

Table 6.1: Comparison of recirculation lengths, X_1, X_2 and X_3 , with [9].

	Present Study	Literature [9]
X_1	7.5	11.8
X_2	5.2	9.5
X_3	11.9	20.6

The divergence of the results shows that numerical diffusion is still present in this work and, in spite of the low time step, quadratic elements used and refined mesh, in cases like this, become somehow relevant.

6.3 Flow in a Channel with Obstacle

Another common study case is the flow in a channel with a cylindrical obstacle, as presented by DA CUNHA [7], in a similar study. For this example, a permanent regime is never reached, since it is expected an oscillating flow past the cylinder. A quadratic 2202 element mesh was used, with $Re = 1000$.

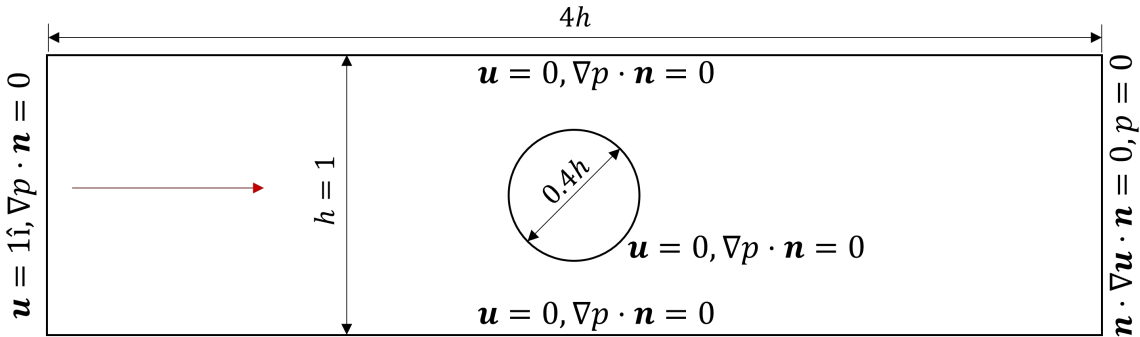
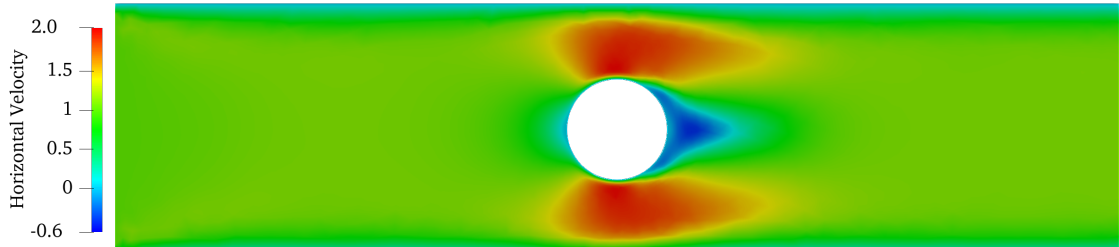
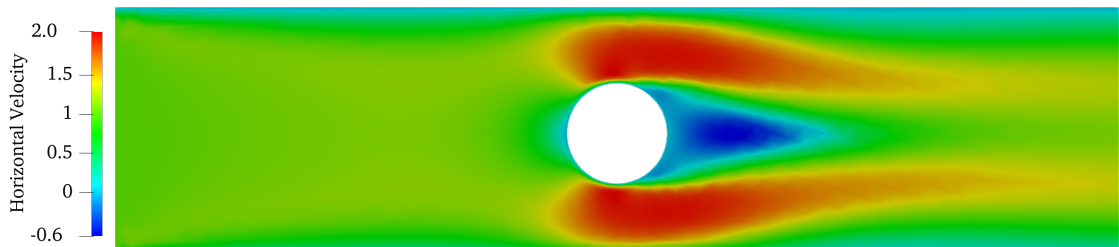


Figure 6.7: Boundary conditions for the in a channel with obstacle.

The transient results are shown in Figure 6.8, for different time steps.



(a) $t = 5$



(b) $t = 30$

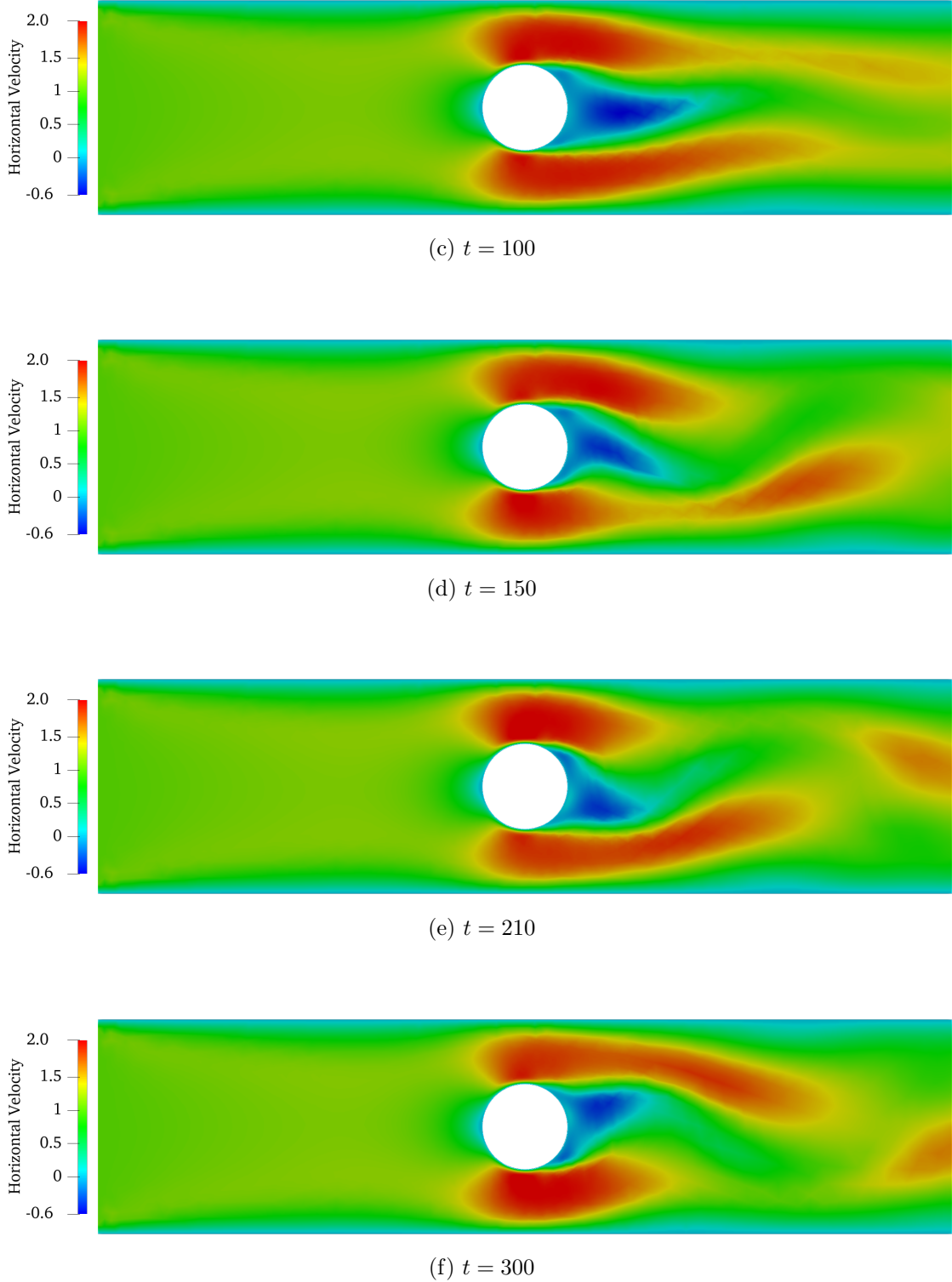


Figure 6.8: Horizontal velocity field for the flow in a channel with obstacle, with $Re = 1000$ and $Ga = 1/Fr^2 = 10^{-4}$.

As can be noticed, the flow past the cylinder oscillates, for a Reynolds number of 1000. A similar conclusion is shown in the work developed by DA CUNHA [7], where the stream function-vorticity formulation is used. Such behavior of the fluid is also responsible for drag, lift and vorticity oscillation, as shown in [7].

6.4 The Cavity with Natural Convection

The problem consists in a confined recipient with a temperature difference between the two side walls. Figure 6.10 shows the stream lines induced by temperature gradient, for $Re = 1$, $Pr = 70.0$, $Ga = 10$ and $Gr = 100$, in a mesh with 1134 elements and 568 vertices. The boundary conditions are shown in Figure 6.9.

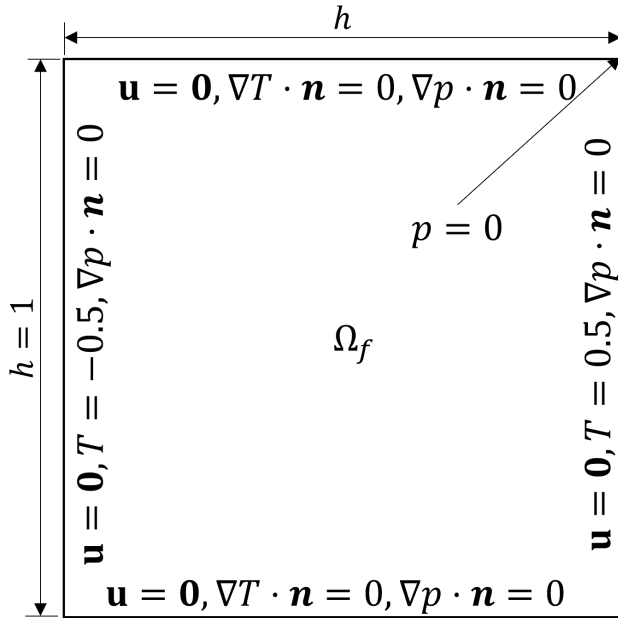


Figure 6.9: Boundary conditions for the natural convection problem.

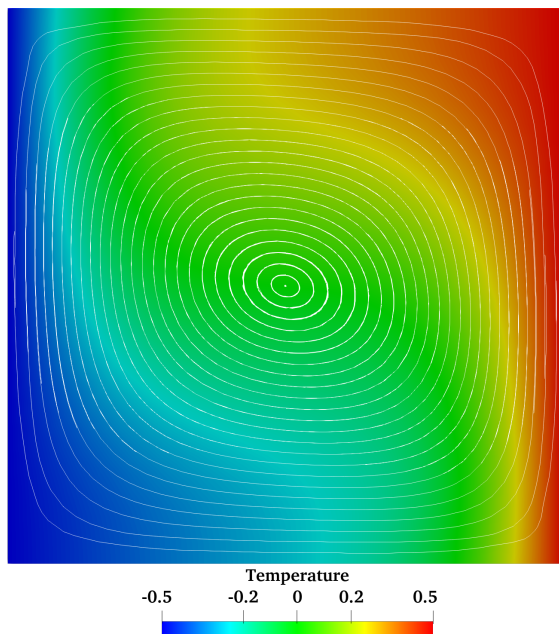


Figure 6.10: Temperature field with stream lines in the natural convection problem.

The horizontal and vertical velocity fields that generate the stream lines above

are shown in Figure 6.11.

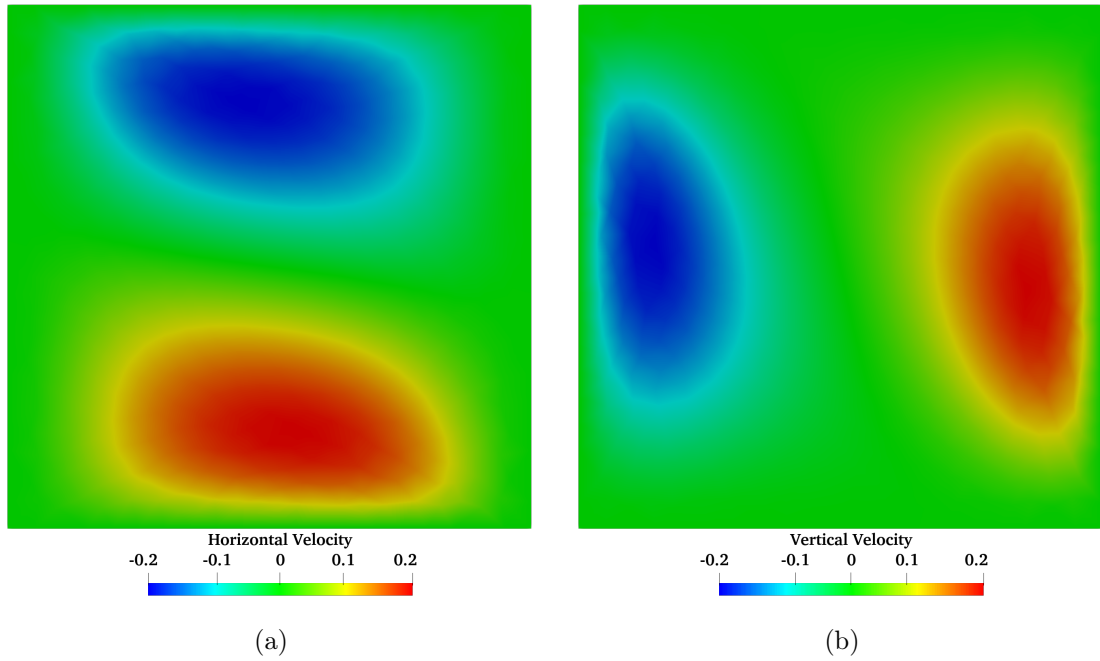
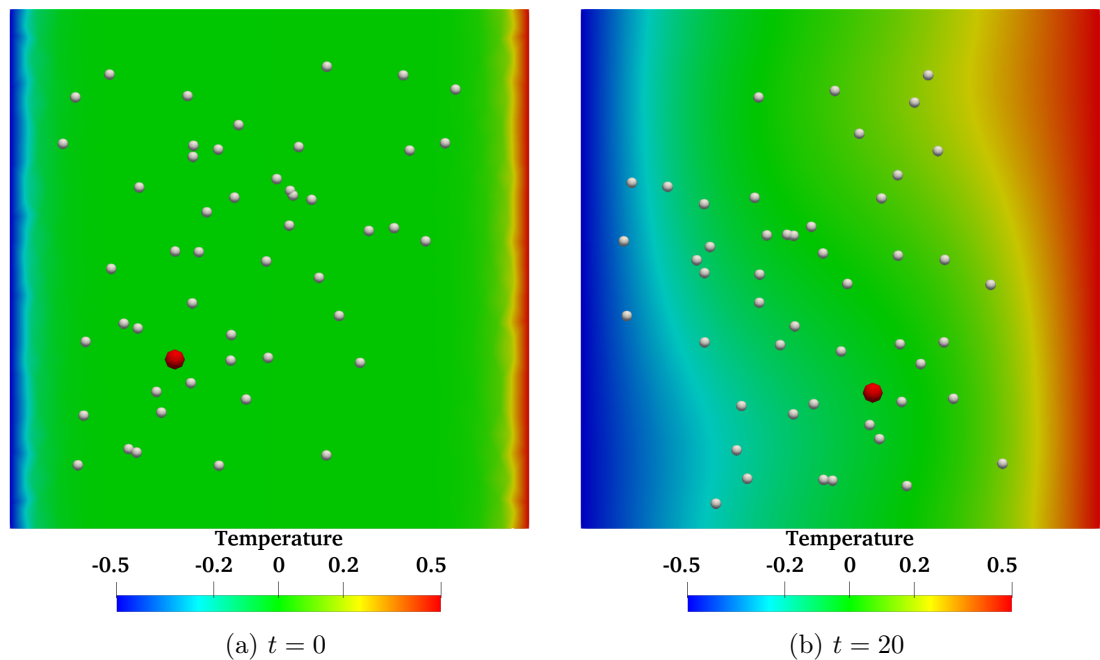


Figure 6.11: Velocity fields in the (a) horizontal and (b) vertical directions for the cavity with natural convection problem.

Figure 6.12 shows how particles behave when the induced velocity field starts to act over them. Particles tend to rotate around the mid point of the domain, as was expected when analyzing the stream lines. A single particle is highlighted in red for better visualization. For this and future example, the time step for particulate positions calculations is 1/10 of the simulation time step.



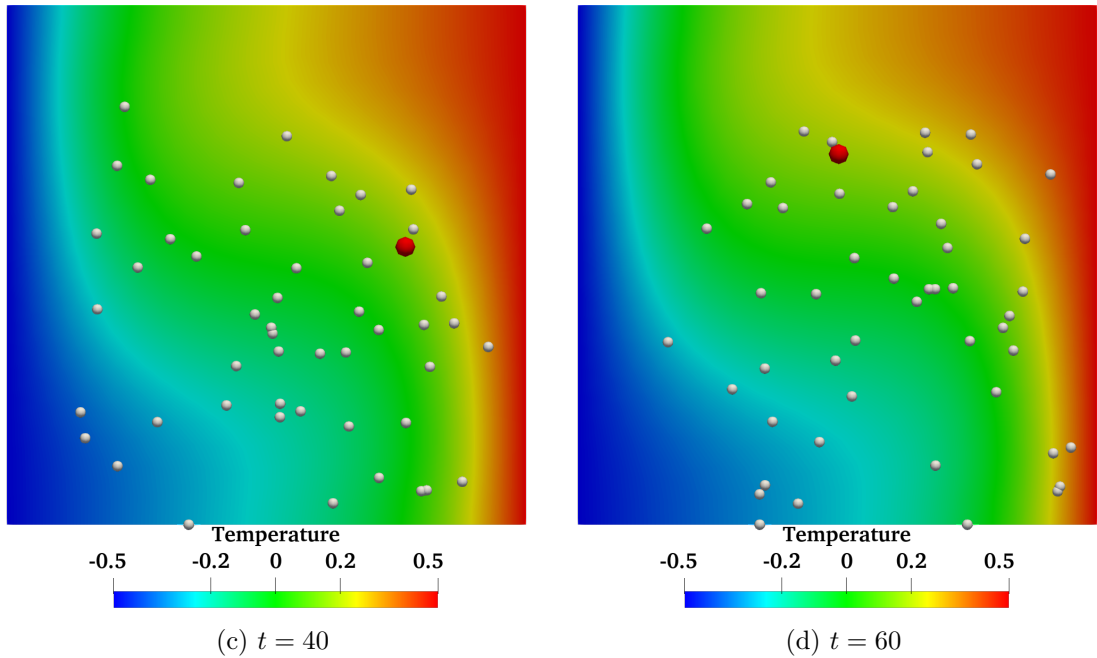


Figure 6.12: Particles' motion at different time steps for the natural convection problem.

As the velocity field is induced by the temperature gradient, the randomly distributed particles start to move in the cavity, according to the natural convective flow.

6.5 The Expansion with Heat Transfer

This case study shows the behavior of fluid and solid phases when subjected to an increase in cross section area to the main flow. Figure 6.13, with the boundary conditions, shows that the fluid enters the chamber at null dimensionless temperature and the three cylinders, at $T = 1.0$, heat up the fluid, as shown in Figure 6.15, for a mesh with 1770 elements and 883 vertices.

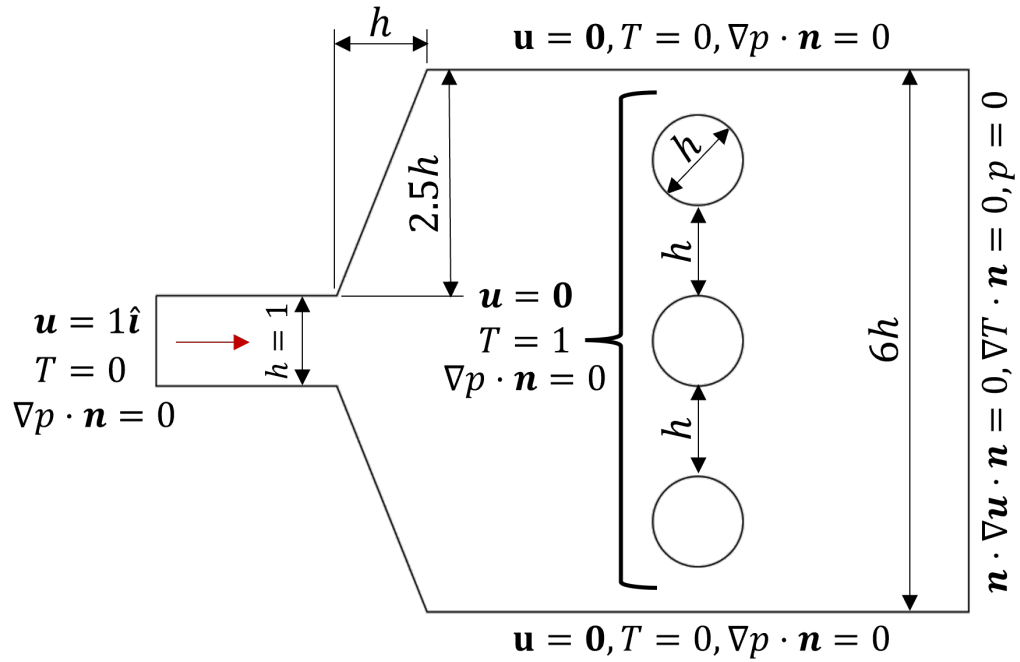


Figure 6.13: Boundary conditions for the expansion problem.

Figure 6.14 describes the stream lines for $Re = 1000$, $Pr = 0.7$, $Gr = 0$ and $Ga = 1/Fr^2 = 10^{-4}$. Recirculation regions appear as the fluid hits the region with a bigger cross-sectional area, mainly due to a high Reynolds Number.

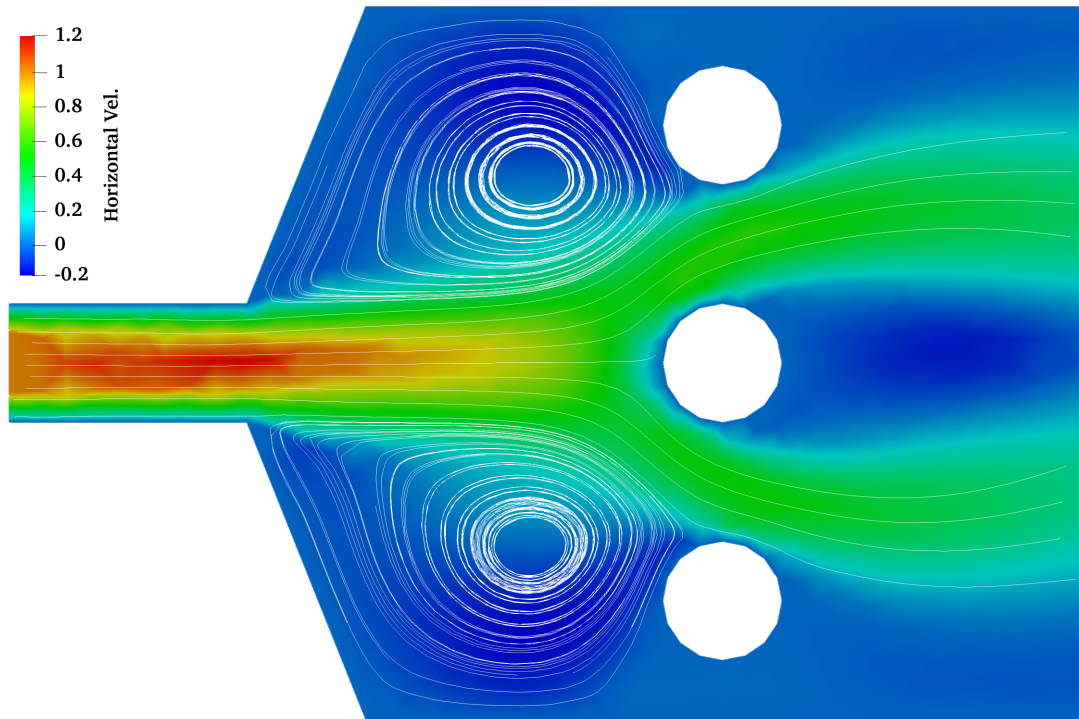


Figure 6.14: Stream lines in the expansion problem, for $Re = 1000$.

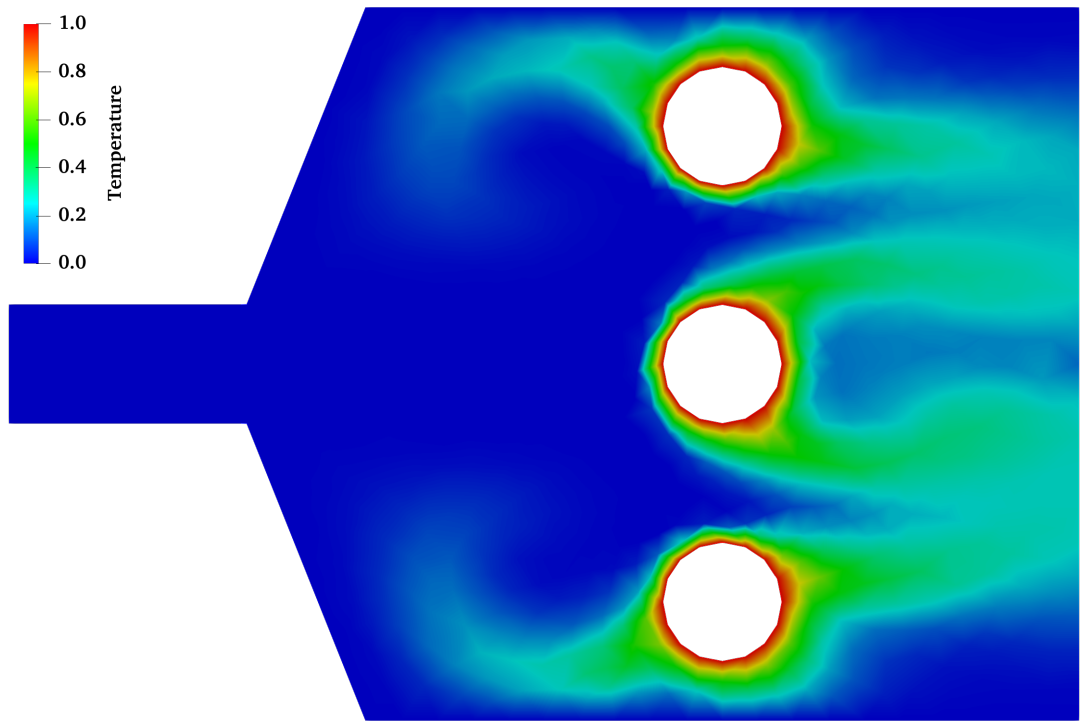
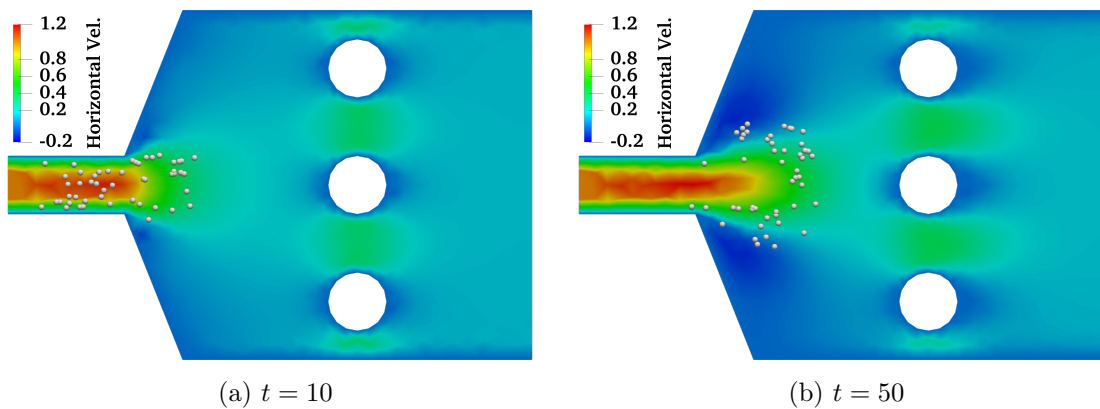


Figure 6.15: Temperature field in the expansion problem, for $Re = 1000$ and $Pr = 0.7$.

It is noticeable that the temperature field follows the stream lines' behavior, especially in the recirculation region. Such behavior is also seen in particles' motion, as presented in Figure 6.16.



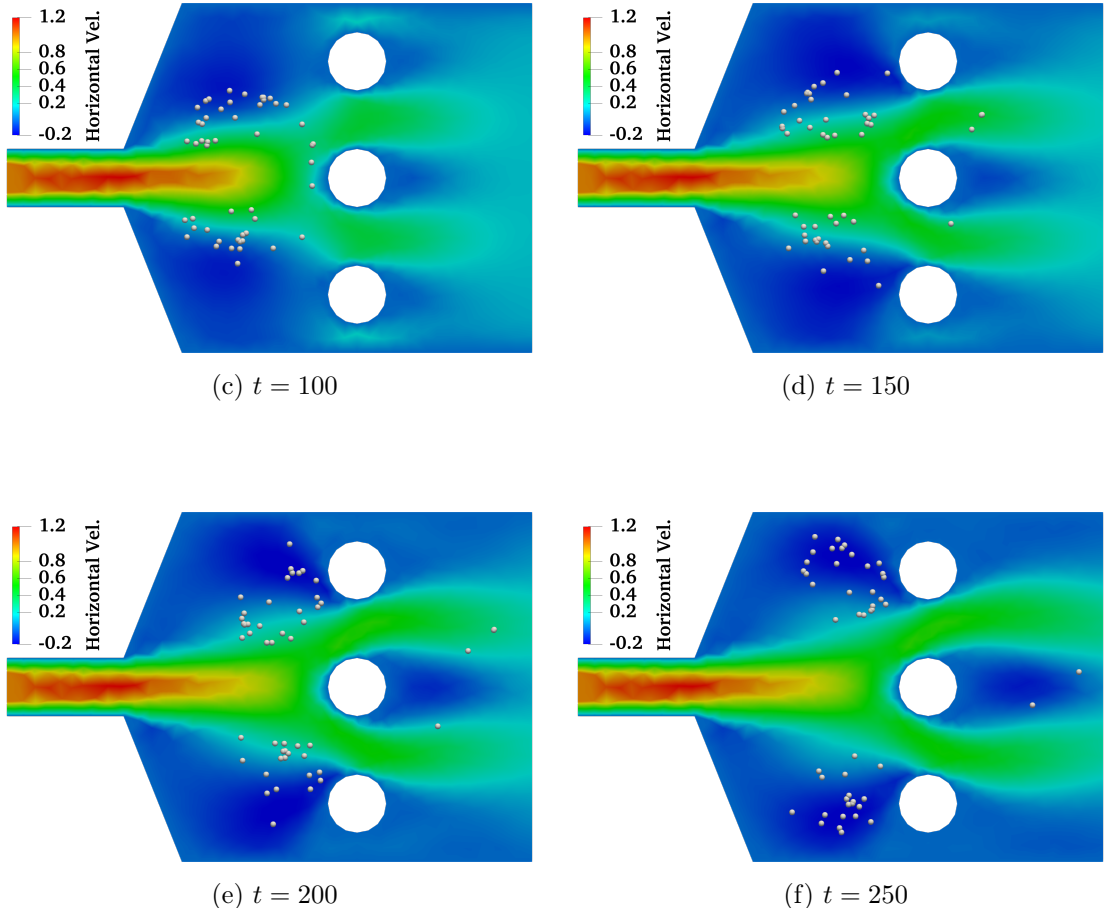


Figure 6.16: Particles' motion at different time steps, for $Re = 1000$.

The sequence shows how light particles end up trapped in the recirculation region and only a few of them get passed through the cylinders. In terms of particle pollution control, that represents an important result as emission to atmosphere may be reduced with a simple mechanism.

6.6 The Poiseuille with Porous Region Flow

As a first example of the Darcy/Forchheimer model described in this work, the simplest case was chosen, which is the Poiseuille problem with two regions: Ω_f , for the free flow, and Ω_p , for the porous one. As shown in Figure 6.17, in the inlet boundary, the velocity was assumed as the fully developed value as seen in the backward-facing step case.

The porous medium used in this work is considered to be a continuous medium, where the parameter of porosity is responsible for the pressure gradient. Also, for particle retention, in the next examples, the cut-off velocity, for which the particle is retained, is defined as 5% of the inlet fluid's velocity.

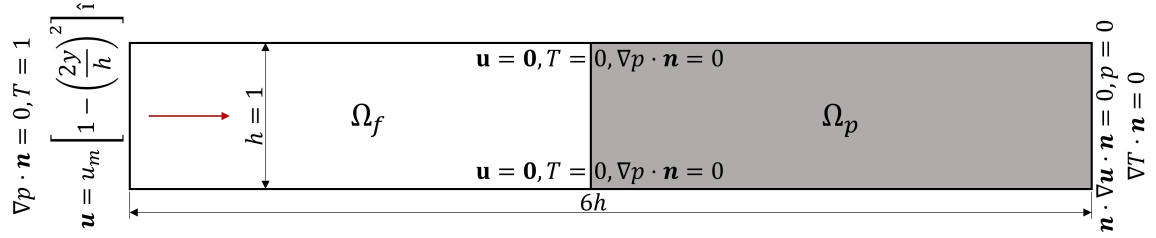


Figure 6.17: Boundary conditions for a Poiseuille with porous region flow, for $Re = 100$.

The simulation was made using a quadratic element mesh, with 3966 elements and a total of 8167 points. In Figure 6.18, it is noticeable the transition between regions, since the velocity profile in the porous region is expected to have a lower peak. For this example, $Re = 100$, $Ga = 1/Fr^2 = 10^{-4}$, $Da = 0.025$, $Fo = 2.0$ and $Pr = 0.7$.

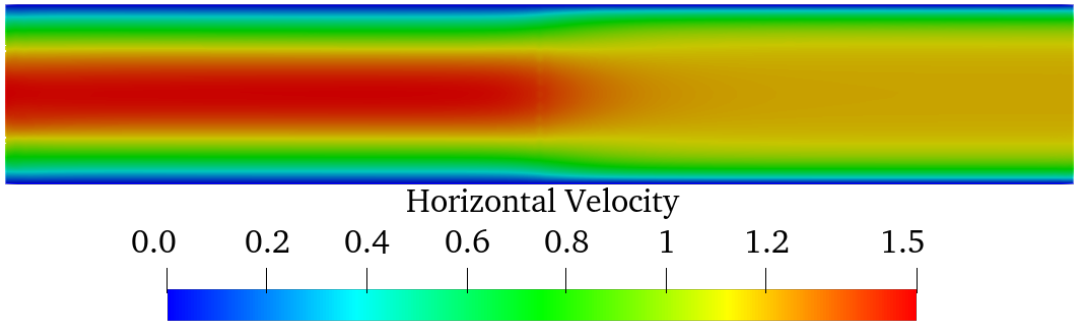


Figure 6.18: Horizontal velocity field for the Poiseuille with porous region flow, for $Re = 100$, $Da = 0.025$ and $Fo = 2.0$.

The temperature field, as noticed in Figure 6.19, is considerably affected by the porous medium, since there is a change in velocity, which influences the convective term of the energy equation.

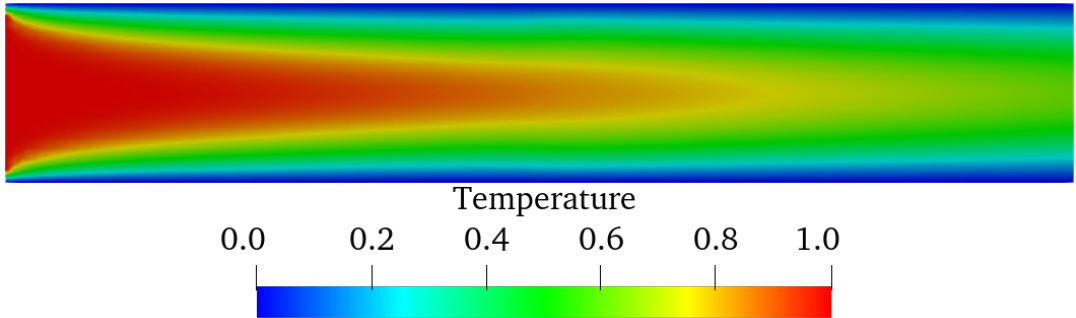


Figure 6.19: Temperature field for the Poiseuille with porous region flow, for $Re = 100$, $Da = 0.025$, $Fo = 2.0$ and $Pr = 0.7$.

Figures 6.20 and 6.21 show the horizontal velocity and pressure variations along

the horizontal mean line of the domain ($y = 0$) for different values of the Darcy number, Da .

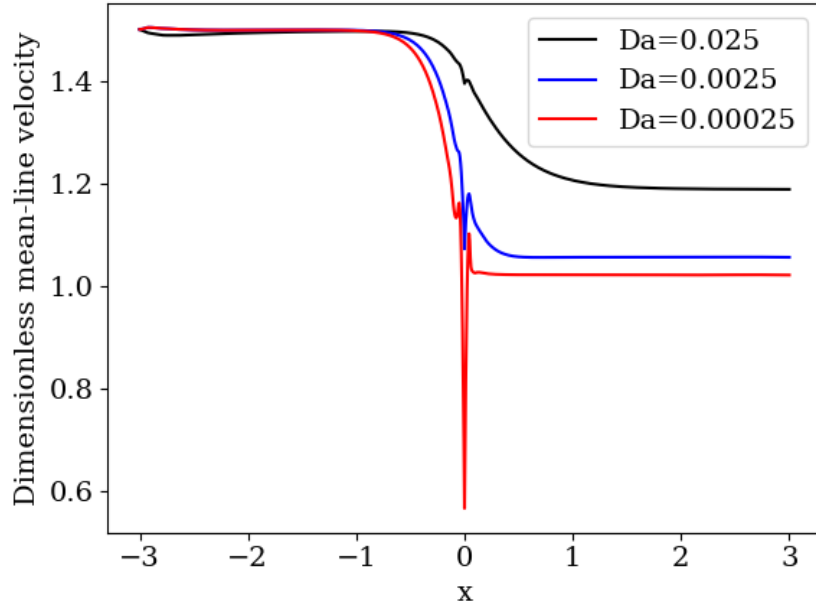


Figure 6.20: Velocity field along the horizontal axial line for the Poiseuille with porous region flow, for different values of Darcy number (Da).

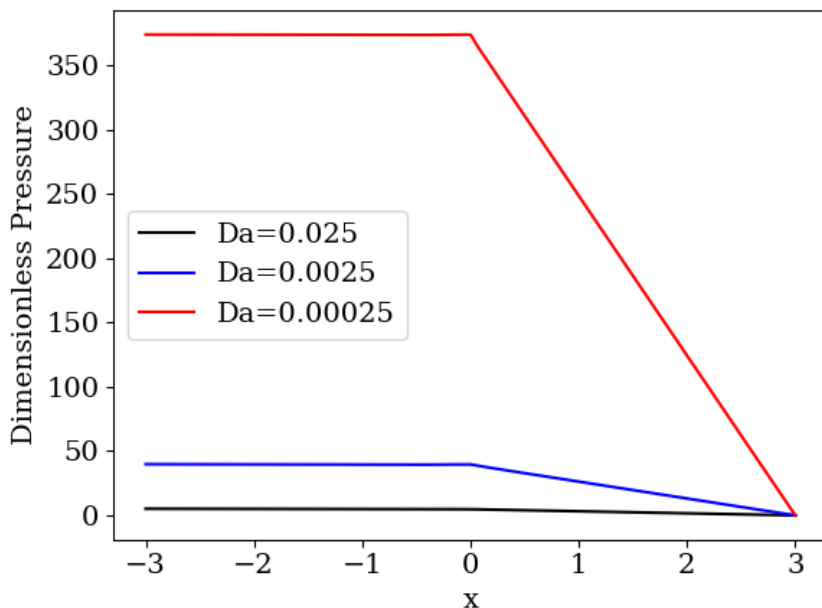


Figure 6.21: Pressure field along the horizontal axial line for the Poiseuille with porous region flow, for different values of Darcy number (Da).

As expected, in the Ω_p region ($x > 0$), pressure values drop in a steeper rate

than that seen in Ω_f ($x < 0$). That is due to the resistance imposed by the Darcy and Forchheimer terms in Eq. (3.23), which are null in Ω_f . Also, due to the change in the differential equation from one region to the other, the frontier may cause instabilities in the velocity field, as shown in Figure 6.20, depending on the value of the Darcy number. If the case to be studied requires a low Darcy number, special treatments on the frontier must be considered, mainly in cases where the velocity field is normal to the surface, like this one. The numerical instability occurs due to the sudden change of resistance imposed by the Darcy/Forchheimer term, containing a non-linear parcel.

6.7 The Flow over Porous Medium

After analyzing qualitatively the Darcy/Fochheimer model for mixed porous/free media in the previous example, this section is intended to compare the results obtained from [4] and the ones simulated in this current work. For that, a quadratic element mesh with 9248 triangular elements and a total of 18879 points was used. Figure 6.22 shows the domain analyzed.

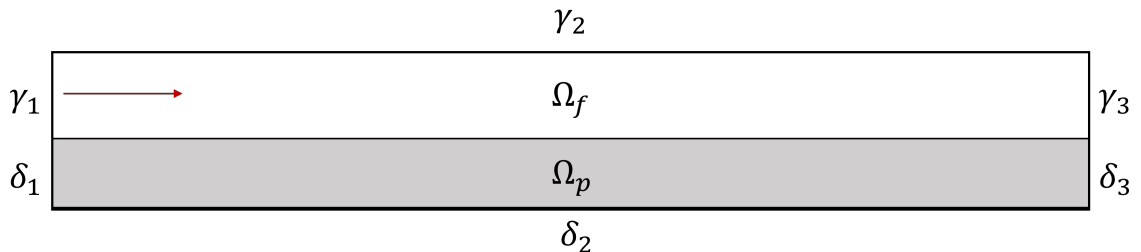


Figure 6.22: Boundary conditions for the flow over porous medium, for $Re = 6, 38$, $Da = 0.373$, $Fo = 1.952$ and $Ga = 1/Fr^2 = 10^{-4}$.

In order to describe the boundary conditions for each boundary, Table 6.2 was built, according to [4].

Table 6.2: Boundary conditions for the flow over porous medium problem, [4].

Boundary	Horizontal vel.	Vertical vel.	Pressure
γ_1	$u = y(4 - y)$	$\nabla v \cdot \mathbf{n} = 0$	$\nabla p \cdot \mathbf{n} = 0$
γ_2	$u = 0$	$v = 0$	$\nabla p \cdot \mathbf{n} = 0$
γ_3	$\nabla u \cdot \mathbf{n} = 0$	$\nabla v \cdot \mathbf{n} = 0$	$p = 0$
δ_1	$u = 0$	$\nabla v \cdot \mathbf{n} = 0$	$\nabla p \cdot \mathbf{n} = 0$
δ_2	$\nabla u \cdot \mathbf{n} = 0$	$v = 0$	$\nabla p \cdot \mathbf{n} = 0$
δ_3	$\nabla u \cdot \mathbf{n} = 0$	$\nabla v \cdot \mathbf{n} = 0$	$p = 0$

As seen in Table 6.2, in walls δ_1 and δ_2 only the non-penetrability condition for velocity is imposed ($\mathbf{u} \cdot \mathbf{n} = 0$) and not the no-slip one. Also, the total length of the channel is 50 and the total height 7, being the horizontal axis located at the interface of the media, located 3 units of length above the bottom interface, so that the Poiseuille condition at γ_1 is $u = y(4 - y)$. The simulation for $Re = 6, 38$, $Pr = 0.7$, $Da = 0.373$, $Fo = 1.952$ and $Ga = 1/Fr^2 = 10^{-4}$ is presented below, in Figure 6.23.

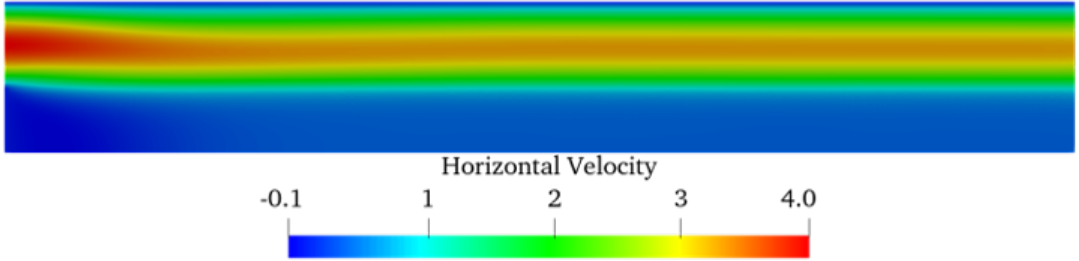


Figure 6.23: Horizontal velocity field for the flow over porous medium, for $Re = 6.38$, $Da = 0.373$, $Fo = 1.952$ and $Ga = 1/Fr^2 = 10^{-4}$.

The velocity field resembles the Poiseuille flow for the Ω_f region due to the high resistance imposed by the porous medium Ω_p . However, as shown in Figure 6.24, in the region close to the inlet boundary, the velocity field is present, as can be seen by vector representation.

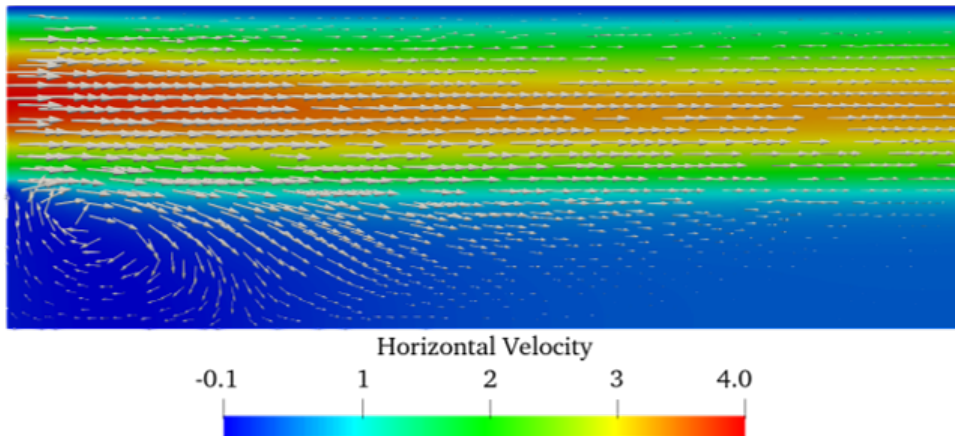


Figure 6.24: Velocity field represented by vectors in the entry region for the flow over porous medium, for $Re = 6, 38$, $Da = 0.373$, $Fo = 1.952$ and $Ga = 1/Fr^2 = 10^{-4}$.

A recirculation zone is formed near the entry boundary, although with modest values of velocity, since it happens in the porous medium. Along the channel, the flow reaches a fully developed regime, so the outlet boundaries are analyzed and compared to [4].

The models presented in [4] were previously presented in the Literature Review section. As stated by the authors, the penalization method (PE), equivalent to the

one used in this work, is a good approximation, in spite of the inaccurate result along the interface of the regions. The horizontal velocity profile of the simulation is then plotted along with the ones obtained by the authors in [4] at the outlet composed by $\gamma_3 \cup \delta_3$, in Figure 6.25.

The NSF and the NSD models explained in [4] are taken as reference, since, according to the authors, they provide a more accurate solution to the problem. Hence, in spite of the PE method's graphical result is not comprised between those two lines, for most of the Ω_f region, the equivalent developed in this work is, except for the portion near the interface, as was already expected. In the Ω_p region, this solution approaches to the PE method's one, for values of y away from the interface.

The model presented here is, therefore, considered accurate enough to simulate not only porous systems but also mixed systems where both porous and free regions are present.

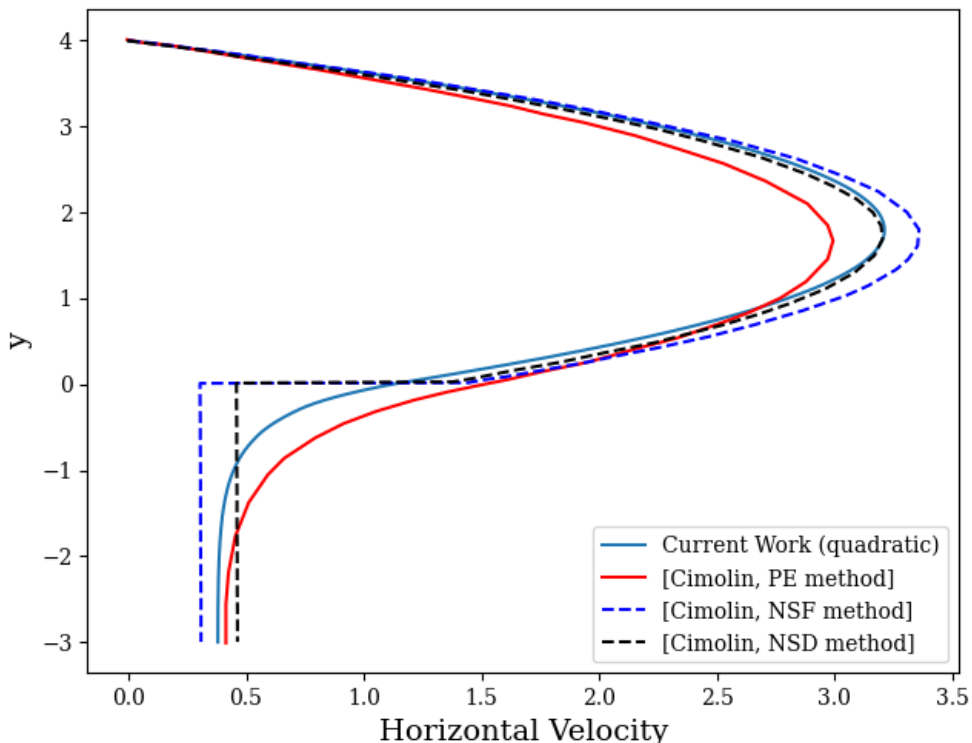


Figure 6.25: Verification of the Darcy/Forchheimer model implemented, [4], for $Re = 6,38$, $Da = 0.373$, $Fo = 1.952$ and $Ga = 1/Fr^2 = 10^{-4}$.

It is important to say that, despite the divergences, all models must respect mass conservation rule. For that reason, the PE method presents a peak in velocity lower than the others but a less steep velocity decay in the Ω_p domain and also the NSF model has the highest maximum velocity and the lowest constant velocity in Ω_p .

Chapter 7

The Diesel Particulate Filter (DPF)

7.1 The Structure of the DPF

Diesel-powered engines are responsible for a major source of air pollution, according to WANG [26]. Besides pollution caused by gas emissions, like NO_x and CO , [27], there is also the one caused by particulate matter that is also emitted in the process. Hence, a wall-flow type of filter, [26], is used, in order to retain part of the soot that comes from the engine.

The DPF is composed by small parallel channels, generally of square cross-sectional area, [26], through which the air filled with solid particles flow and, when in contact with the walls and the pressure gradient, gets filtered as particles are captured by the structure of the porous wall. Figure 7.1 shows the schematic drawing of the DPF structure.

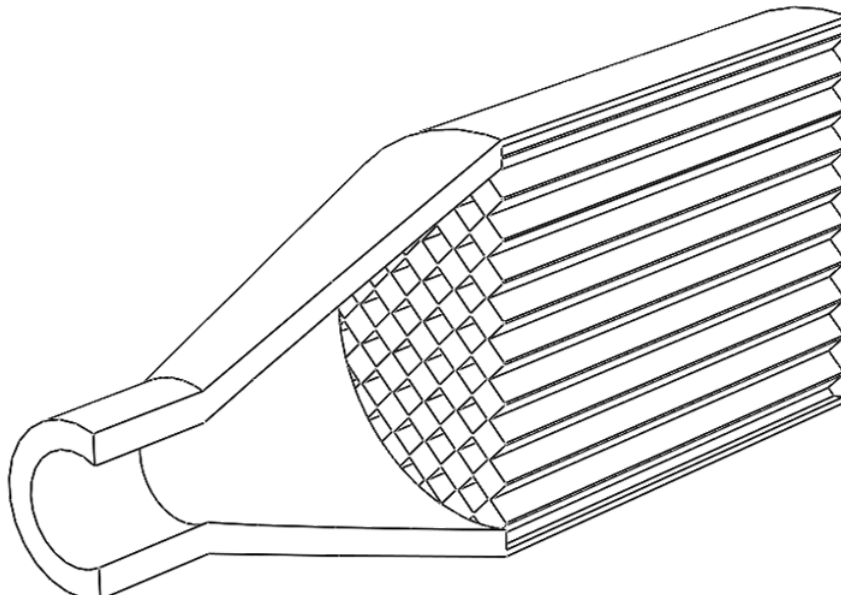


Figure 7.1: Schematic drawing of the DPF. The structure resembles a honeycomb, through which the fluid enters and gets filtered.

The structure presented in Figure 7.1 resembles a honeycomb, where the square-shaped cross-sectional area is visible through an axial cut view. As described in [8], the DPF is located downstream a Diesel Oxidation Catalyst (DOC), which is responsible for oxidizing hydrocarbons (*HC*) and carbon monoxides (*CO*). The DPF and the DOC compose a system of filtration of gases that are emitted to atmosphere. A closer view of a single channel is shown in Figure 7.2, where the fluid's and particles' trajectories are described.

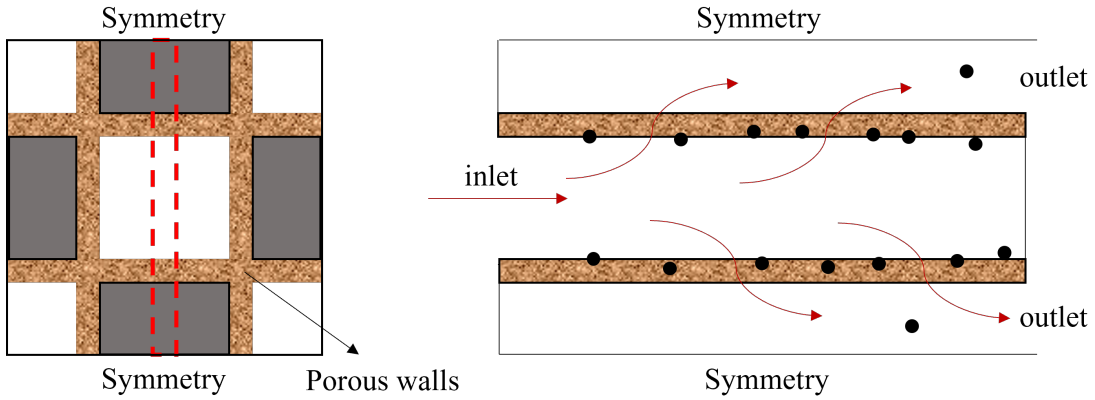


Figure 7.2: Schematic drawing of the DPF's channel, [8], where the filtration system is evidenced. The analyzed region is comprised within the dashed red line.

Although most particles are retained in the porous walls, some amount make their way through the outlet channels. A single channel is used to simulate the flow behavior and particle filtration. For that, the region used is the one inside the dashed rectangle in Figure 7.2, which is a small portion of a single channel, away from both side walls, so that a two-dimensional approach is adequate. Since channels are placed respecting a pattern, symmetry lines on the upper and lower boundaries are considered.

7.2 Particulate Size Distribution

In order to evaluate the size distribution of the particulate matter emitted from both diesel and biodiesel engines, a few concepts on statistics need to be defined. As shown in Figure 2.3, [3], the size distributions have the aspect of a log-normal distribution, in which the logarithm of the diameter (D_p) follows the normal curve, described by PINHEIRO *et al.* [28]. Hence, the curve to be approximated is defined in Eq. (7.2).

$$\frac{dN}{d[\log(D_p)]} = \frac{N}{\sqrt{2\pi}\log(\sigma_g)} \exp\left(-\frac{\log(D_p) - \log(\bar{D}_{pg})}{2\log^2(\sigma_g)}\right) \quad (7.1)$$

Here, N is the total number of particles in the distribution per unit of volume and \bar{D}_{pg} and σ_g are the geometric mean diameter and standard deviation, respectively. For discrete distributions the geometric properties are obtained from the mean diameter logarithm and its standard deviation, as follows:

$$\overline{\log(D_p)} = \sum_{i=1}^N \frac{\log(D_{pi})}{N} \quad (7.2)$$

Using the property of the sum of logarithms leads to:

$$\overline{\log(D_p)} = \log \left(\prod_{i=1}^N D_{pi} \right)^{\frac{1}{N}} \quad (7.3)$$

Where the geometric mean diameter is given by:

$$\bar{D}_{pg} = \left(\prod_{i=1}^N D_{pi} \right)^{\frac{1}{N}} \quad (7.4)$$

The logarithm of the geometric standard deviation of the diameter is given by:

$$\log(\sigma_g) = \sqrt{\sum_{i=1}^N \frac{(\log(D_{pi}) - \overline{\log(D_p)})^2}{N}} \quad (7.5)$$

$$\log(\sigma_g) = \sqrt{\sum_{i=1}^N \frac{\left[\log \left(\frac{D_{pi}}{\bar{D}_{pg}} \right) \right]^2}{N}} \quad (7.6)$$

After adjusting the curve's parameters in Eq. (7.2) to fit the data obtained from

[3], the plots in Figure 7.3 are obtained.

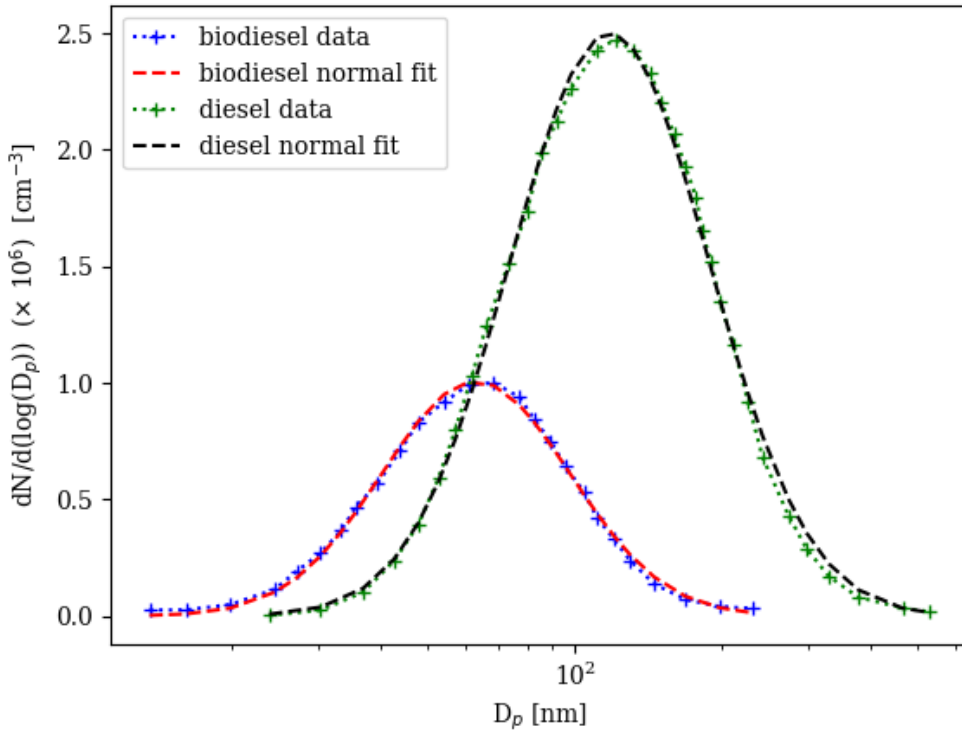


Figure 7.3: Normal curves and their data fit for diesel and biodiesel, based on [3]. The curve fit is used to quantify the normal distribution of particles emitted by both fuels. The mean diameter of biodiesel particles are noticed to be smaller than diesel ones, with a lower concentration as well.

As expected the curve-fit to a log-normal distribution was appropriate and led to the parameters in Table 7.1.

Table 7.1: Curve-fit parameters for diesel and biodiesel particles size distribution.

Fuel	N	$\log(\bar{D}_{pg})$	$\log(\sigma_g)$
Diesel	2.502	2.071	0.204
Biodiesel	1.007	1.798	0.192

MESQUIDA [8] provides a classification table according to the particulate size, as shown in Table 7.2. Observing the curves in Figure 7.3 and Table 7.1, it is possible to evaluate the ranges of aerodynamic diameters for both diesel and biodiesel.

Table 7.2: Classification of particulate size, [8].

Classification	Particulate size
Large particles	$> 10 \mu m$
Coarse particles	$2.5 - 10 \mu m$
Fine particles	$0.1 - 2.5 \mu m$
Ultra-fine particles	$50 - 100 nm$
Nanoparticles	$< 50 nm$

For biodiesel, most particles are concentrated within the ultra-fine particle range, including the mean diameter of $63 nm$. As for diesel, most of them are concentrated within the fine particle range, since the mean diameter measures $118 nm$. This data shows that diesel's particles are, in average, almost twice as large as biodiesel's. Another important data is the area below the curves, represented by the parameter N , that suggests that the number of particles emitted by diesel engines is about 2.5 times as many as the number of particles emitted by biodiesel-powered engines.

7.3 The DPF Flow Simulation

The first simulation of the DPF system is made to compare with the one obtained by MESQUIDA [8] with a commercial software. For that, the same parameters and domain were used, with a 189794 triangular MINI element mesh. The proportion between the total length and the entry channel is 118.8 and the dimensionless numbers are: $Re = 228$, $Ga = 1/Fr^2 = 10^{-4}$, $Pr = 0.7$, $Da = 5.92 \times 10^{-5}$ and $Fo = 1.0$.

As for boundary conditions, the inlet velocity is prescribed as $\mathbf{u} = 1.0\hat{\mathbf{i}}$, a no-slip condition is imposed on the walls and a prescribed null pressure is attributed to the outlet channels. Both symmetry lines have the same boundary conditions, with null Neumann for the horizontal velocity ($\nabla u = 0$) and null Dirichlet for the vertical one ($v = 0$). Figure 7.4 shows the horizontal velocity field and Figure 7.5, a comparison with the literature for the horizontal velocity in the mean line of the geometry.

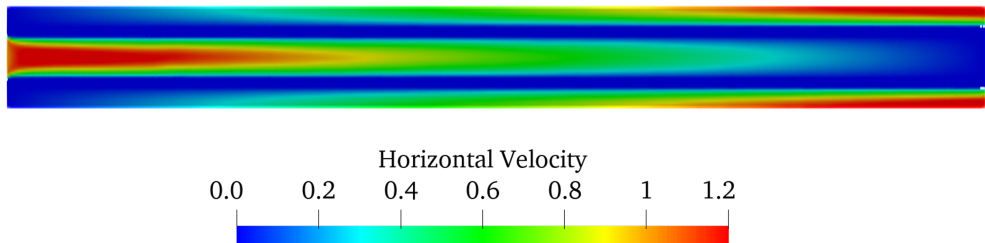


Figure 7.4: DPF flow simulation, based on [8], with a proportion between the total length and the entry channel of 118.8.

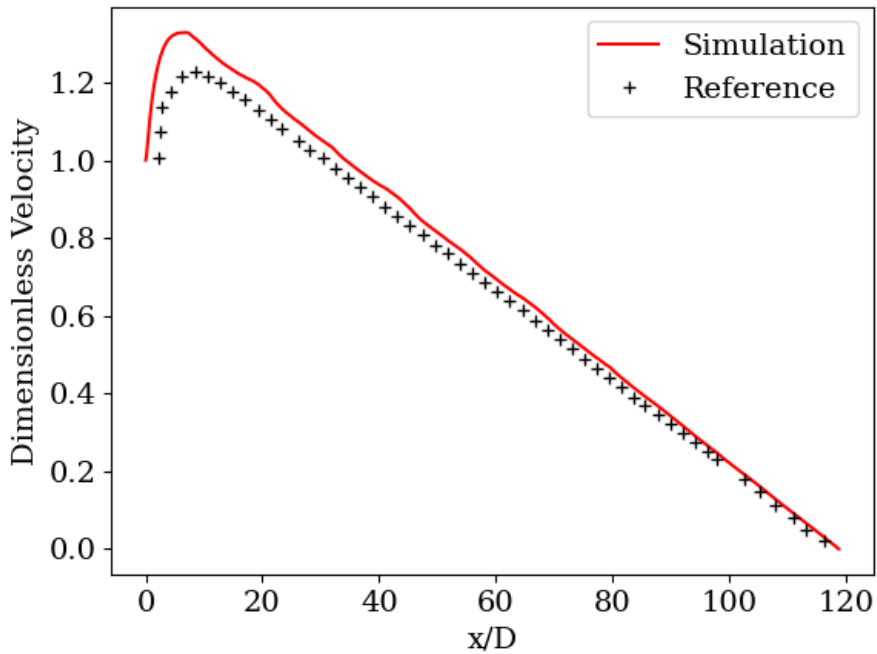


Figure 7.5: DPF mean-line horizontal velocity compared to [8], with $Re = 228$.

The plot of the horizontal velocity field and the mean-line horizontal velocity along the axial direction seen in Figures 7.4 and 7.5, respectively, are in accordance to the ones shown in [8], for the same Reynolds number of 228, using a laminar model, especially for regions that are closer to the inner part of the channel. The highest velocity field regions are the inlet and the outlet, which is reasonable, since the mass of the system must be conserved. the wall located at the very end of the channel, opposite to the inlet, is where the pressure gradient is higher and, therefore, there is a higher trend that particles escape through the final portion of the DPF, impelled by the fluid pushed through the porous medium.

7.4 The Particle-laden Multiphase Flow in the DPF

In this section, the behavior of soot particles, from both diesel and biodiesel, in a DPF will be evaluated, considering and tracking a constant amount of particles in accordance with each fuel's particulate matter concentration seen in Figure 7.3. For this simulation, a smaller ratio between the channel's length and the entry channel was considered, with the value of 8.0. The mesh used has 13244 elements and the scheme is shown in Figure 7.6, where the shaded areas represent the porous regions. The characteristic length, $L = 1$, is the inlet channel's average width.

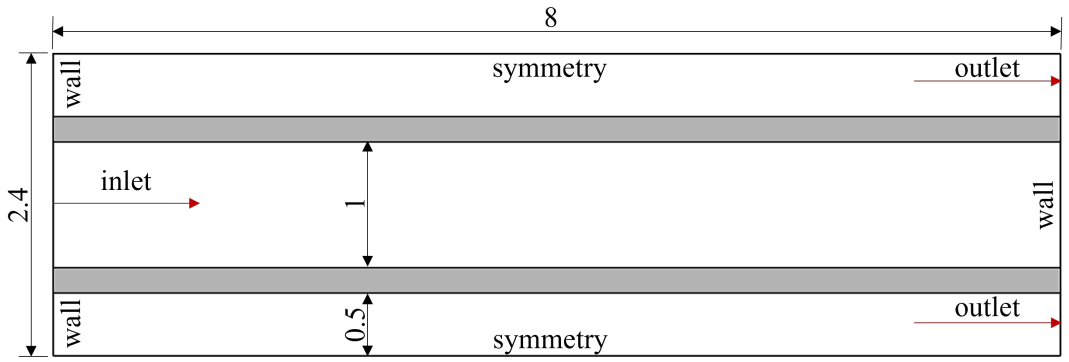
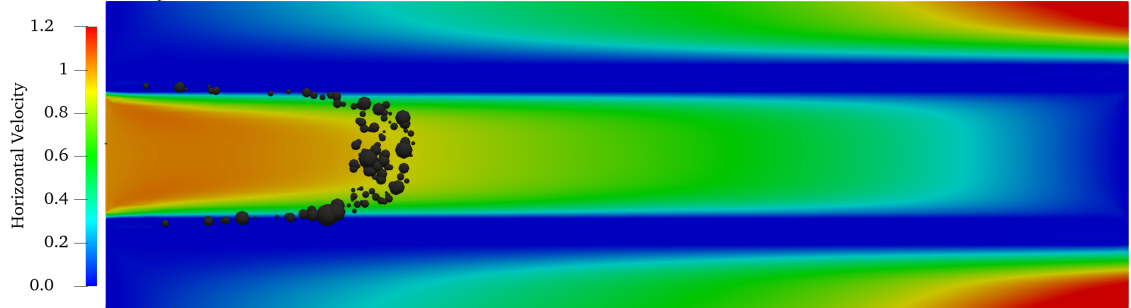


Figure 7.6: Scheme of the DPF and its dimensions.

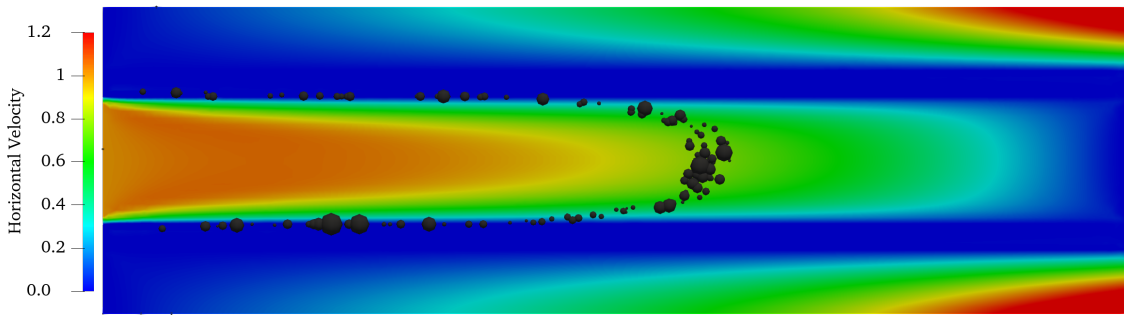
Figure 7.7 shows the flow and particles' behavior in a transient regime for the diesel fuel.



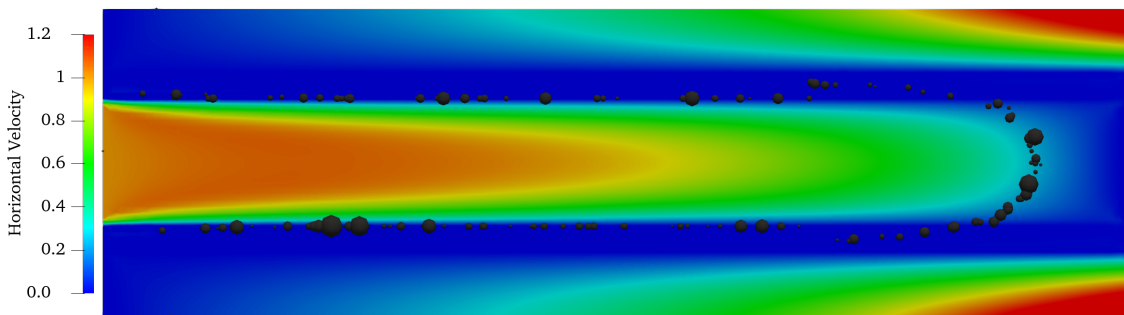
(a) $t = 0$



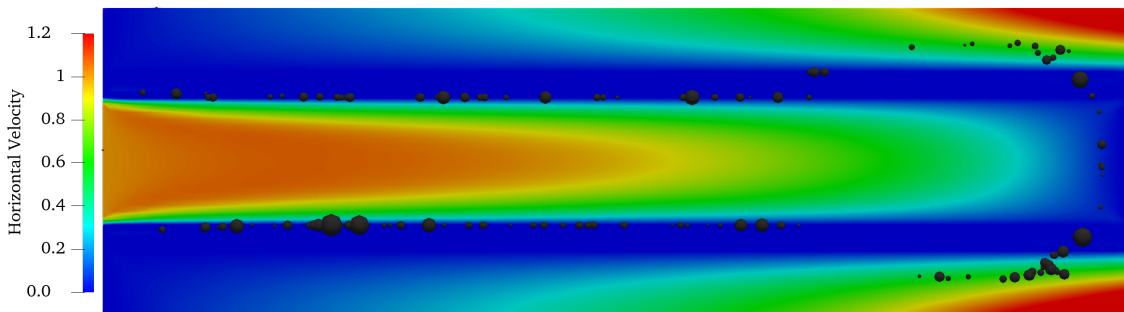
(b) $t = 20$



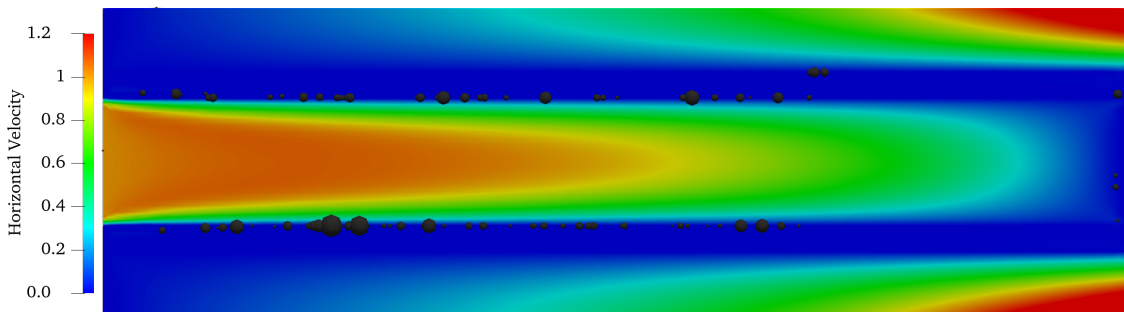
(c) $t = 50$



(d) $t = 100$



(e) $t = 140$



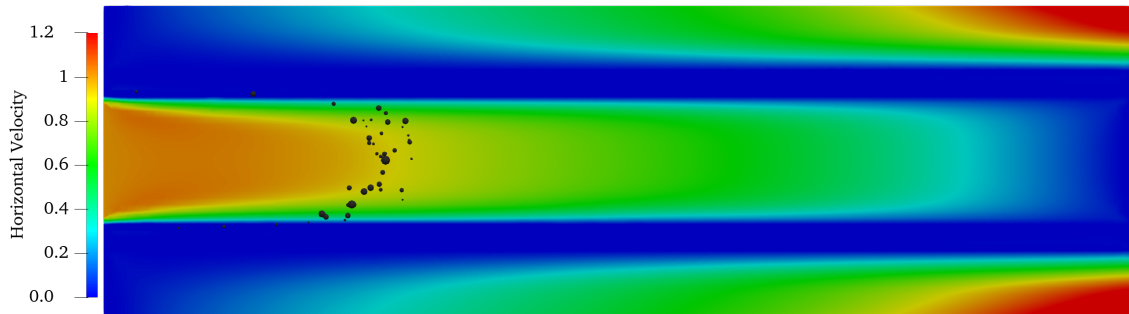
(f) $t = 180$

Figure 7.7: Horizontal velocity field and particles' trajectories at different time steps of the diesel DPF, for $Re = 228$, $Da = 10^{-4}$, $Fo = 2.0$ and $Ga = 1/Fr^2 = 10^{-2}$.

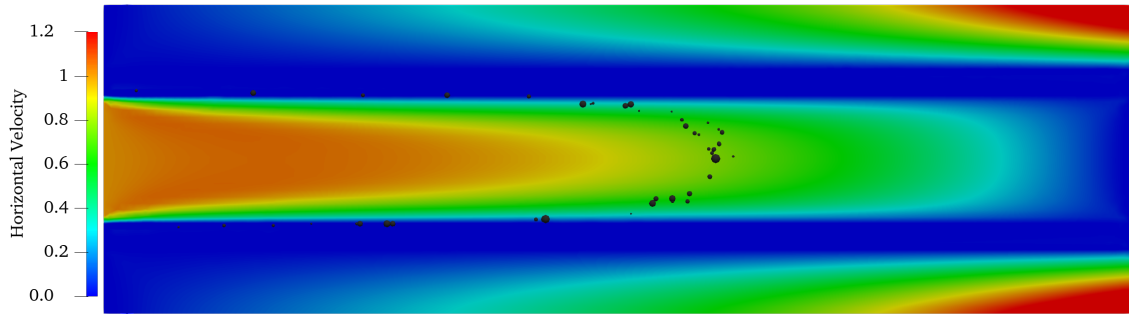
In a similar way, biodiesel particulate is also analyzed under the same conditions, considering a lower concentration, as suggested in Figure 7.3. The plots are shown in Figure 7.8.



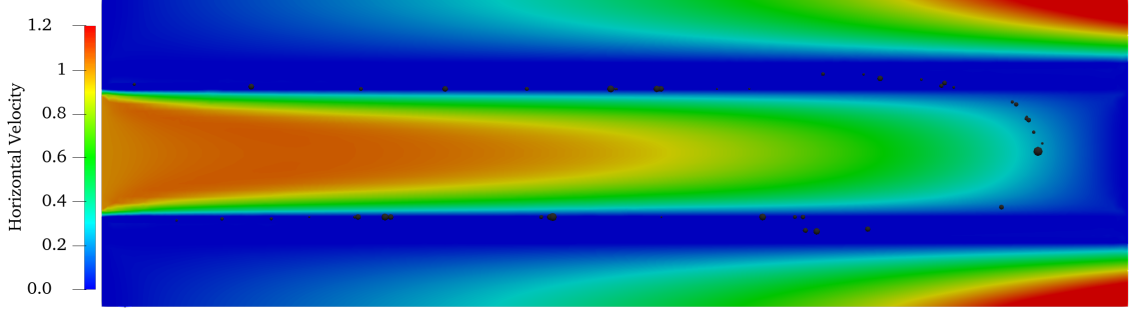
(a) $t = 0$



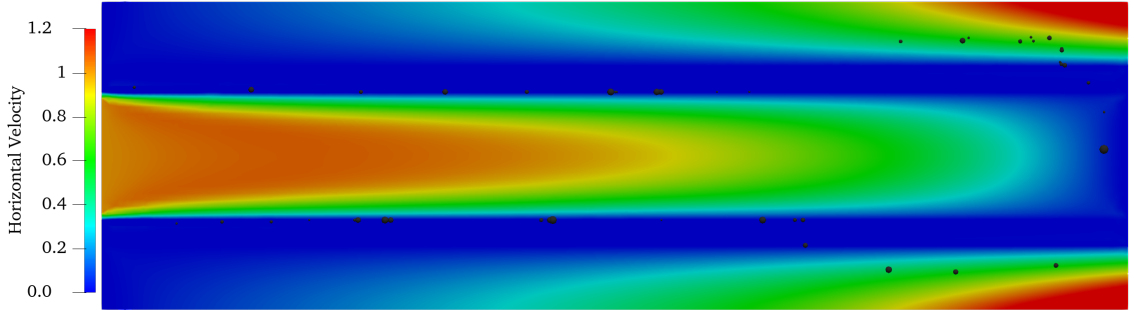
(b) $t = 20$



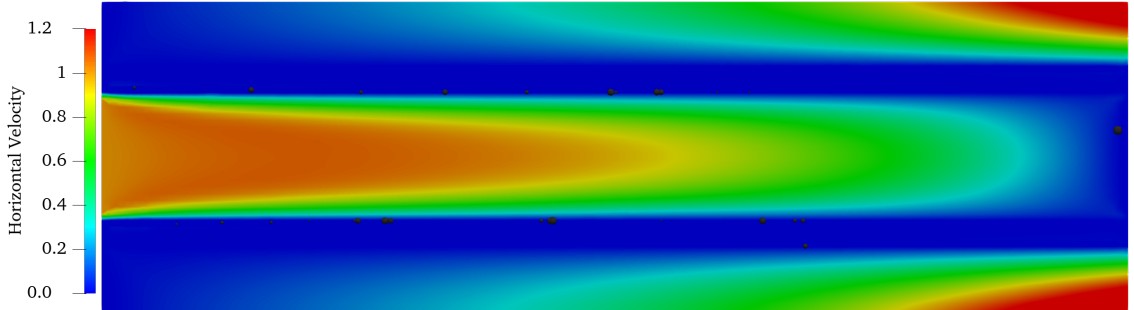
(c) $t = 50$



(d) $t = 100$



(e) $t = 140$



(f) $t = 180$

Figure 7.8: Horizontal velocity field and particles' trajectories at different time steps of the biodiesel DPF, for $Re = 228$, $Da = 10^{-4}$, $Fo = 2.0$ and $Ga = 1/Fr^2 = 10^{-2}$.

Comparing and analyzing Figures 7.7 and 7.8, one can easily conclude that diesel's soot is present in a higher concentration than biodiesel's. Also biodiesel particles are, in average, smaller, as shown in Figure 7.3. All particles are out of scale in order to be visible in the channel, since their diameter is about 10^{-6} smaller than the entry channel's height.

For both systems, particles that make their way through the final portion of the channel end up escaping the filter and exiting through the exit channels. That occurs due to the increase of pressure near the stagnation points that are located at

the opposite wall of the entry interface. The pressure gradient can be seen in Figure 7.9.

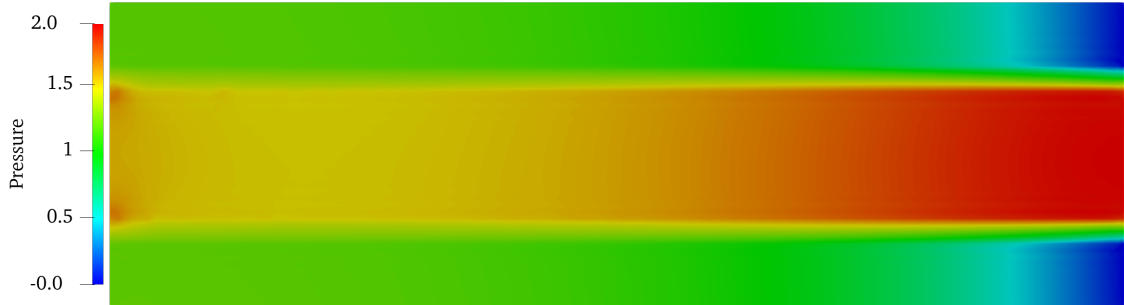


Figure 7.9: DPF pressure field, for $Re = 228$, $Da = 10^{-4}$ and $Fo = 2.0$.

By zooming in to the region close to the exit channels in the velocity field plot, shown in Figure 7.10, it is possible to detect that velocity field vectors become more vertical and, therefore, the fluid passes in a higher speed through the final portions of the porous layers. That explains why particles in Figures 7.7 and 7.8 escape through the filter more easily in said final portion of the channel.

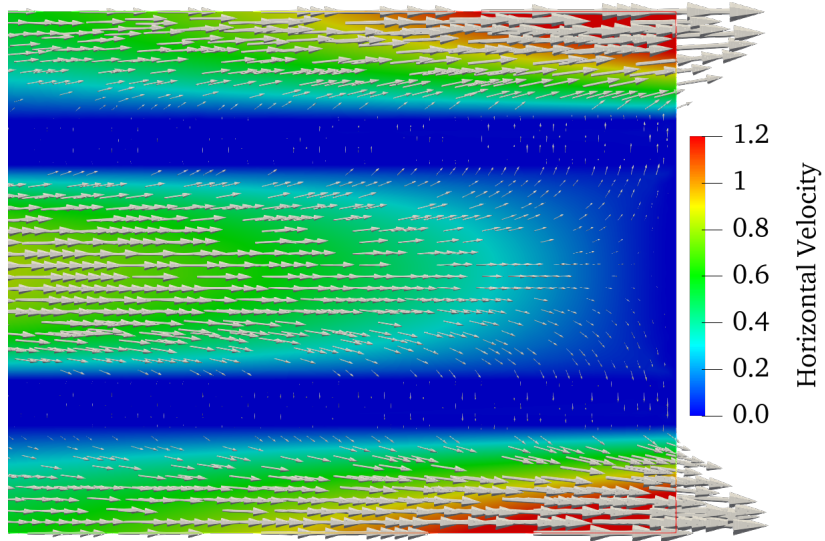


Figure 7.10: DPF velocity field near the exit, for $Re = 228$, $Da = 10^{-4}$ and $Fo = 2.0$.

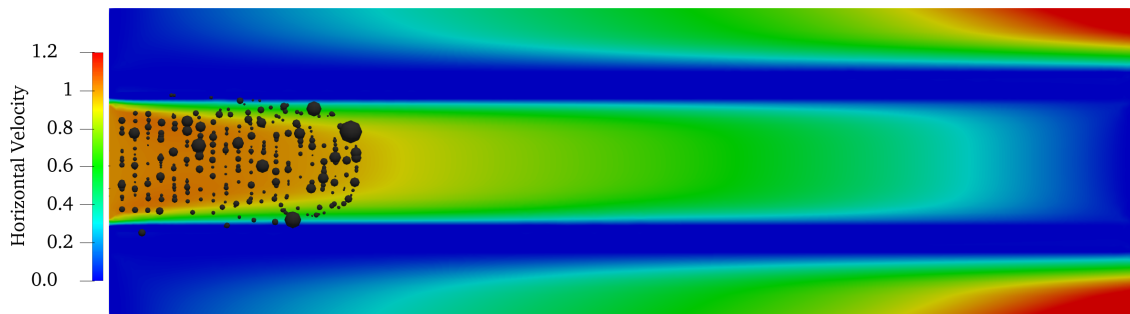
7.5 The DPF with Continuous Particulate Injection

This section is intended to simulate the actual behavior of a particle-laden DPF system, where the injection of particles is made in a continuous form, for which 17 particles are injected at each time step for the diesel DPF and 6, for the biodiesel one, according to their previously defined concentration and size distribution. Figure

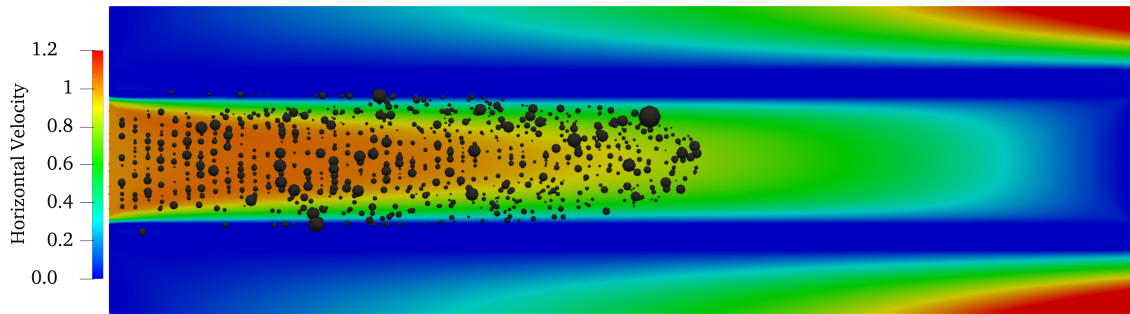
7.11 shows the simulation for the diesel fuel, where particles are, once again, out of scale for better visualization.



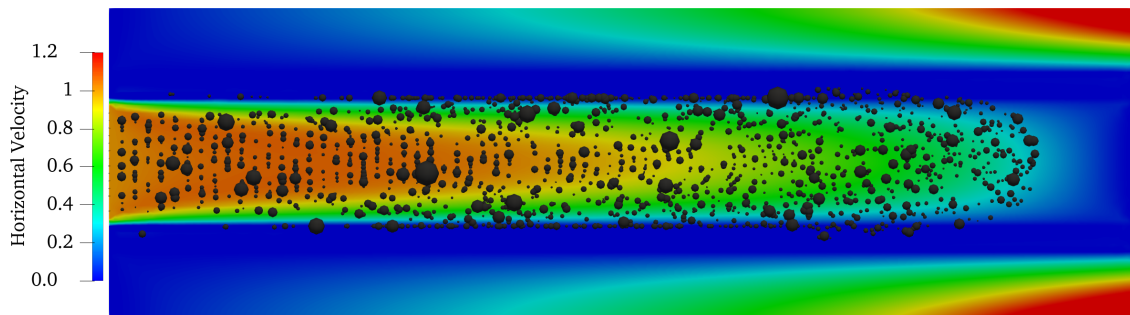
(a) $t = 0$



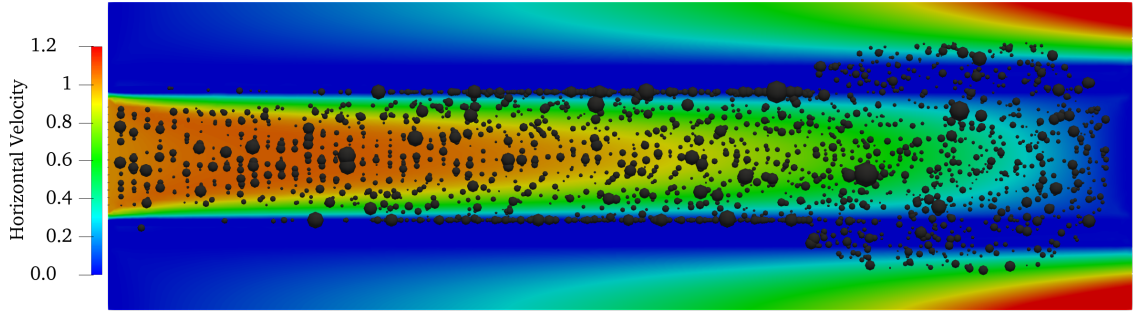
(b) $t = 20$



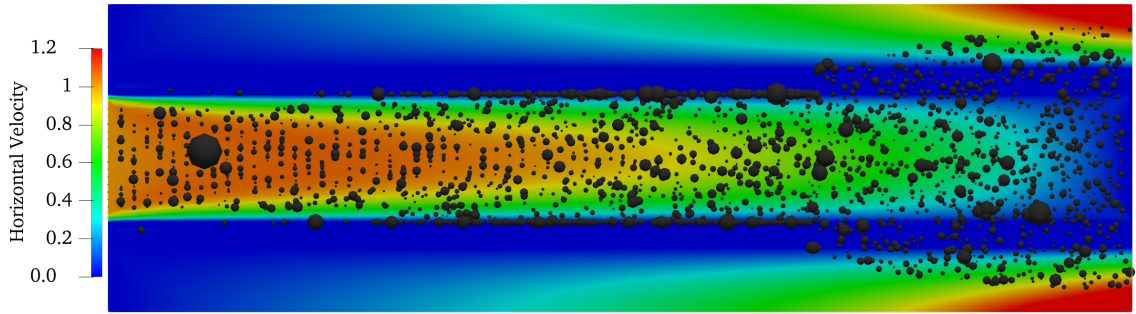
(c) $t = 50$



(d) $t = 100$



(e) $t = 140$



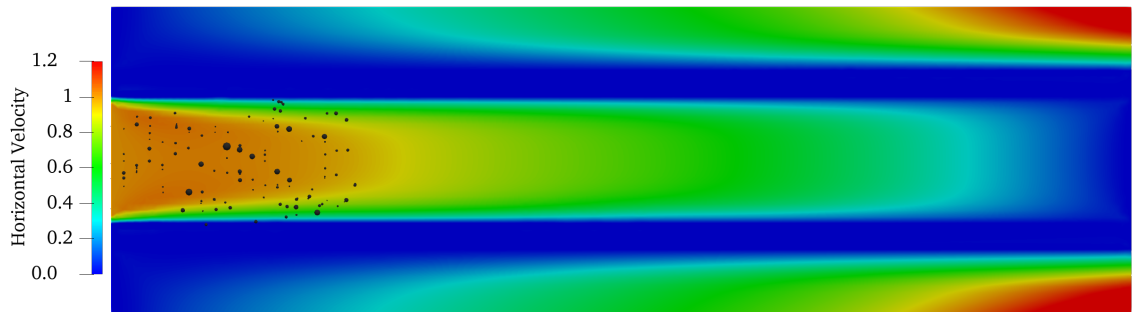
(f) $t = 180$

Figure 7.11: Horizontal velocity field and particles' trajectories at different time steps of the diesel DPF for a continuous injection, for $Re = 228$, $Da = 10^{-4}$, $Fo = 2.0$ and $Ga = 1/Fr^2 = 10^{-2}$.

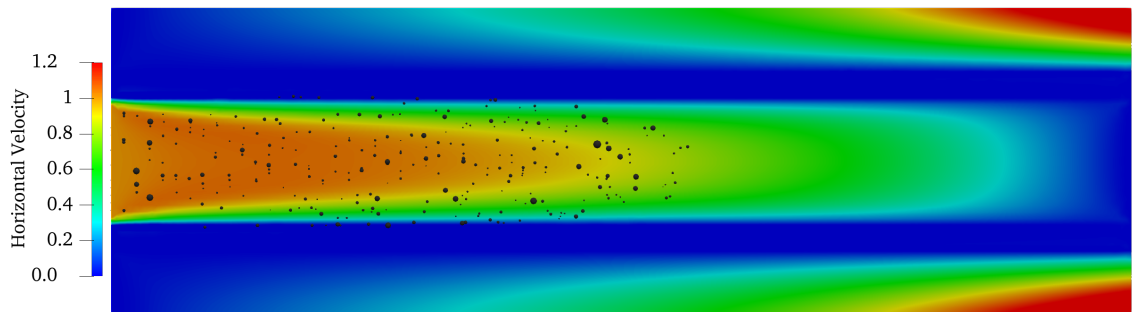
Similarly, the flow in the DPF for a biodiesel-powered engine is shown in Figure 7.12.



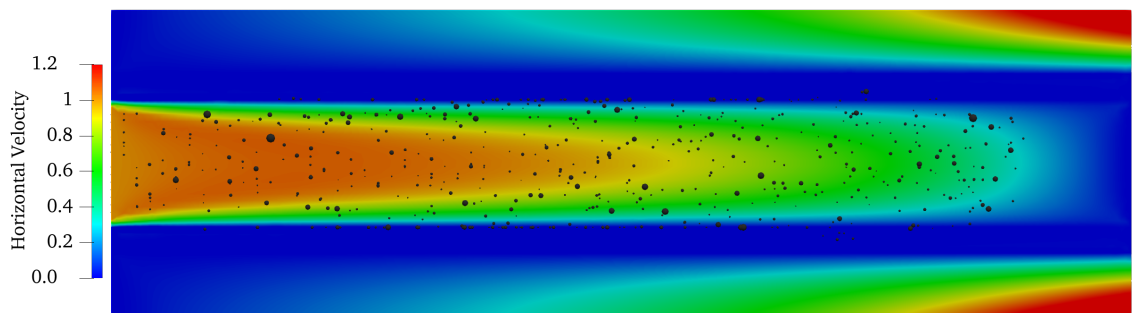
(a) $t = 0$



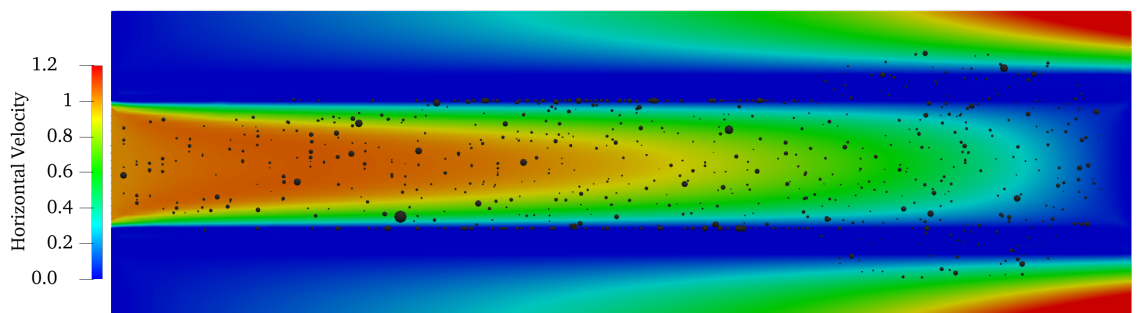
(b) $t = 20$



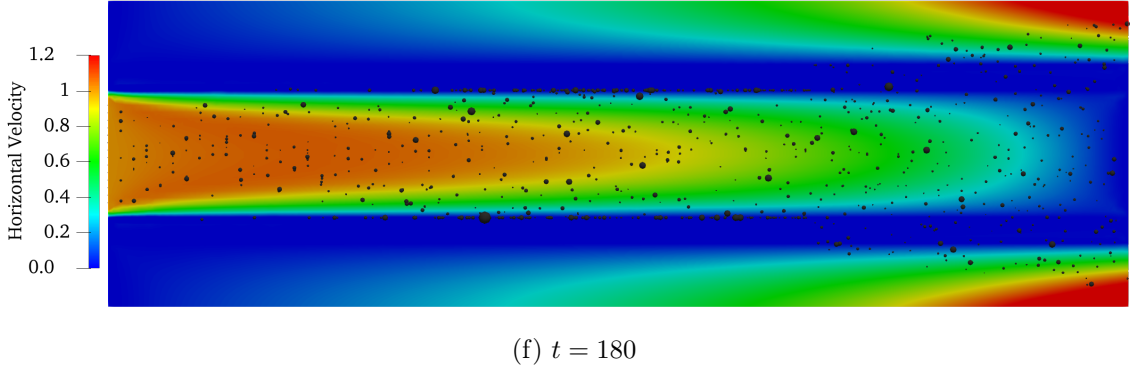
(c) $t = 50$



(d) $t = 100$



(e) $t = 140$



(f) $t = 180$

Figure 7.12: Horizontal velocity field and particles' trajectories at different time steps of the biodiesel DPF for a continuous injection, for $Re = 228$, $Da = 10^{-4}$, $Fo = 2.0$ and $Ga = 1/Fr^2 = 10^{-2}$.

This simulation specifically shows how the filter works in a real scenario, where particles are constantly injected into the channels, carried by the fluid. In the beginning of the filter, particles that are led to the porous sides of the domain are more likely to get stuck to it. That happens due to the high resistance imposed by the filter associated with a not so high pressure gradient between both sides of the filter, as seen in Figure 7.9, which causes a low velocity component normal to the porous region, which is responsible for carrying particulate matter from the inlet to the outlet channels. As particles reach the end of the filter, the pressure gradient increases and, even though the filter resistance is the same, the high velocities proportioned by said gradient are able to break their way into the outlet channel.

Comparing the two fuels studied here, it is evident that biodiesel produces much less particulate matter than pure diesel, a fossil fuel. For that reason, although less particles are retained in the porous media in biodiesel-powered engines, the emission rate to atmosphere is also lower, as shown in Figure 7.12(f), compared to Figure 7.11(f), at which the permanent regime had already been reached. It is, however, concerning the fact that finer particles are emitted by biodiesel consumption, that are mostly within the range of nanoparticles and cause more injuries to human health when inhaled and penetrate the respiratory system.

Figures 7.13 and 7.14 show, respectively, for diesel and biodiesel, the number of particles exiting and entering the channel.

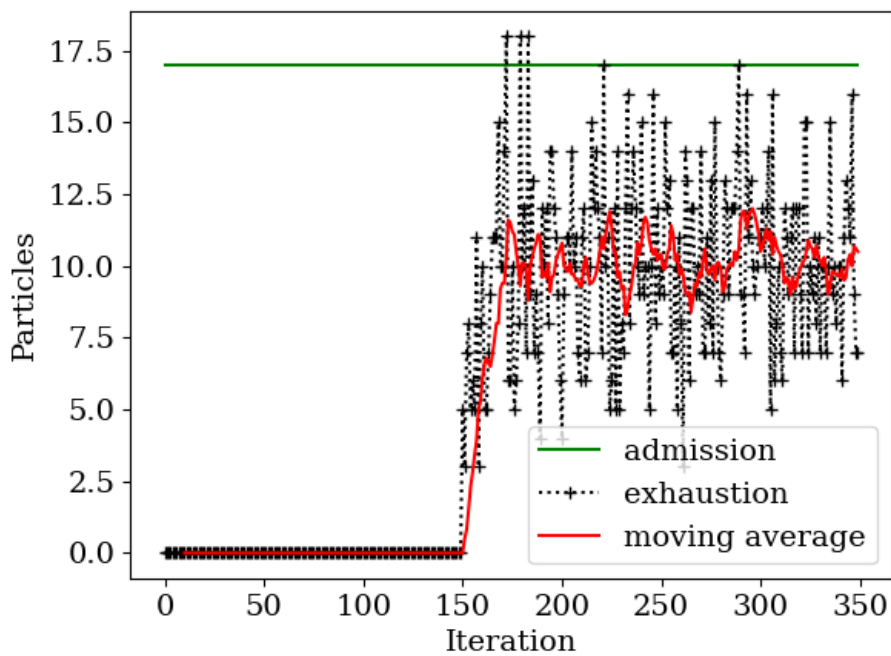


Figure 7.13: Particles' admission and exhaustion rates for diesel-powered engines.

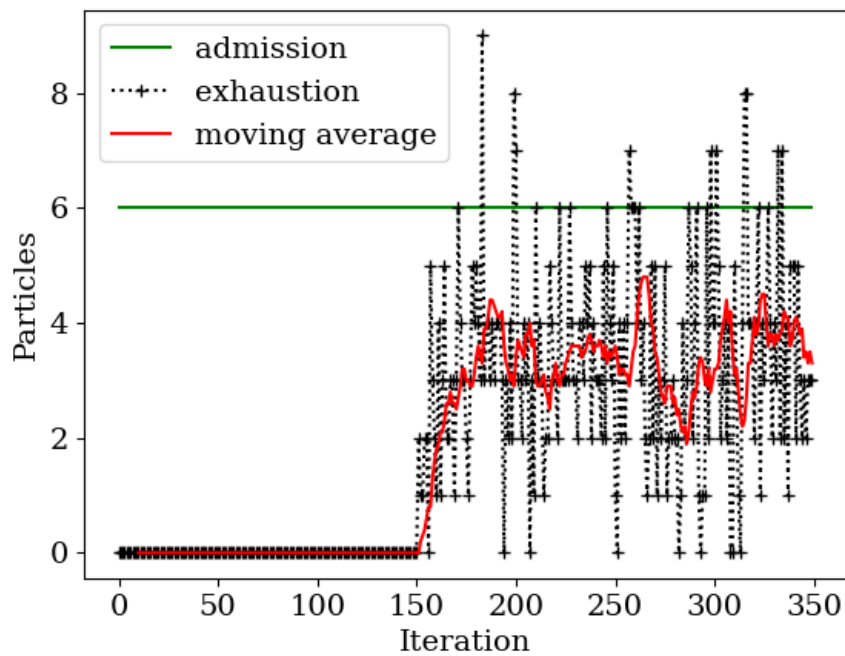


Figure 7.14: Particles' admission and exhaustion rates for biodiesel-powered engines.

In order to smooth the data, the moving average, which is the average between the last 10 points (since the time step used was 0.1) for each iteration, is plotted. As can be seen, for diesel, as more particles are injected in each iteration, more

particles exit when the permanent regime is reached. Comparing both systems, for the filter presented, diesel DPF presented a 40% efficiency of filtration and a similar percentage, of 43%, was calculated for the biodiesel DPF. This efficiency (η) was calculated considering the mean exhaustion rate, N_e , and the admission rate, N_a , as shown below:

$$\eta = \frac{N_a - N_e}{N_a} \quad (7.7)$$

7.6 Analysis of the Filter's Geometry

In order to determine whether the geometry of the channel influences on the effectiveness of the filter, six new filters were used, as will be presented next. The mean thickness of the filter is maintained in all of them.

7.6.1 The Internal Steep Edge

For this geometry, the scheme can be seen in Figure 7.15, where a convergent channel is formed.

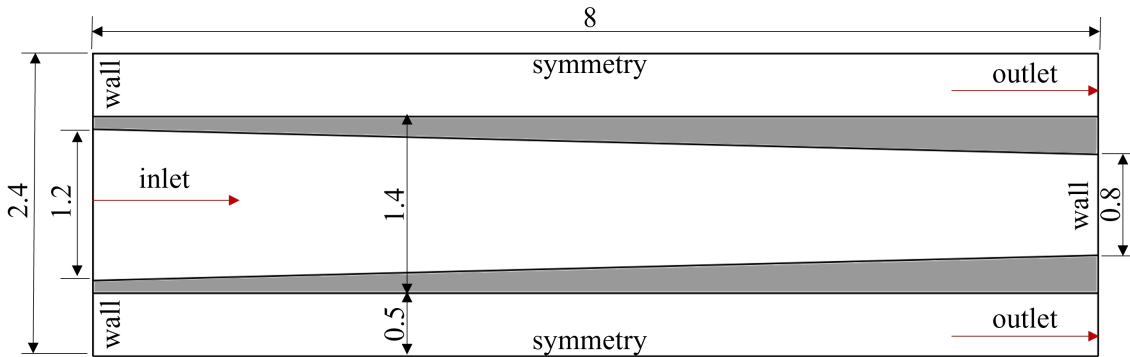


Figure 7.15: Scheme of the DPF with internal steep edge.

After the systems reach the permanent regime, the horizontal velocity field and particle distribution are analyzed, as seen in Figures 7.16 and 7.17, for diesel and biodiesel, respectively.

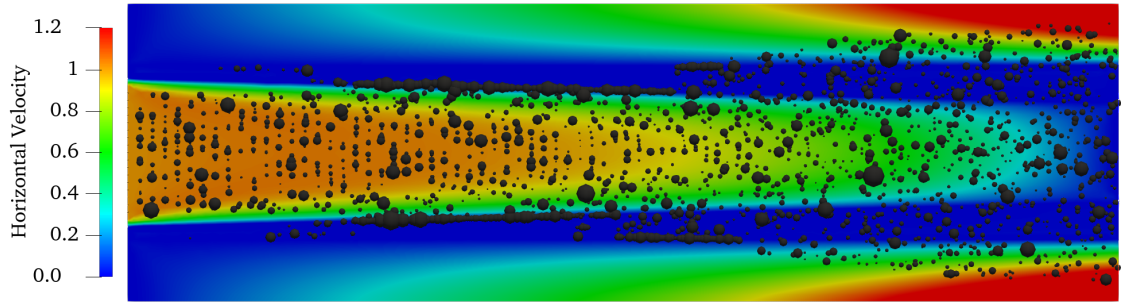


Figure 7.16: Velocity field and particle distribution in the permanent regime for the diesel DPF with an internal steep edge.

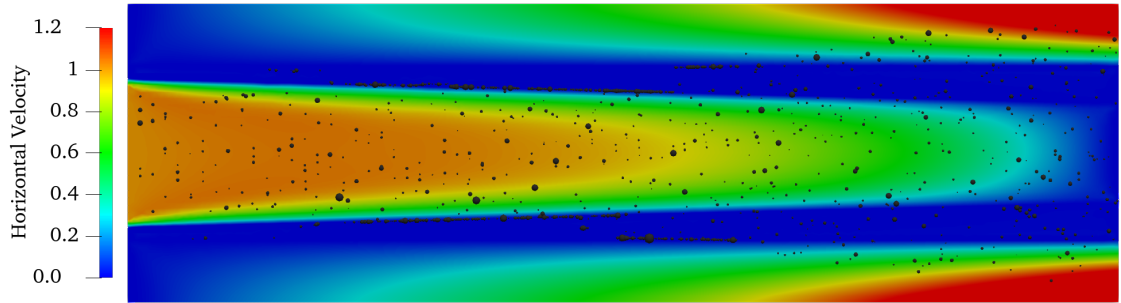


Figure 7.17: Velocity field and particle distribution in the permanent regime for the biodiesel DPF with an internal steep edge.

The exhaustion rates are shown next, for each fuel:

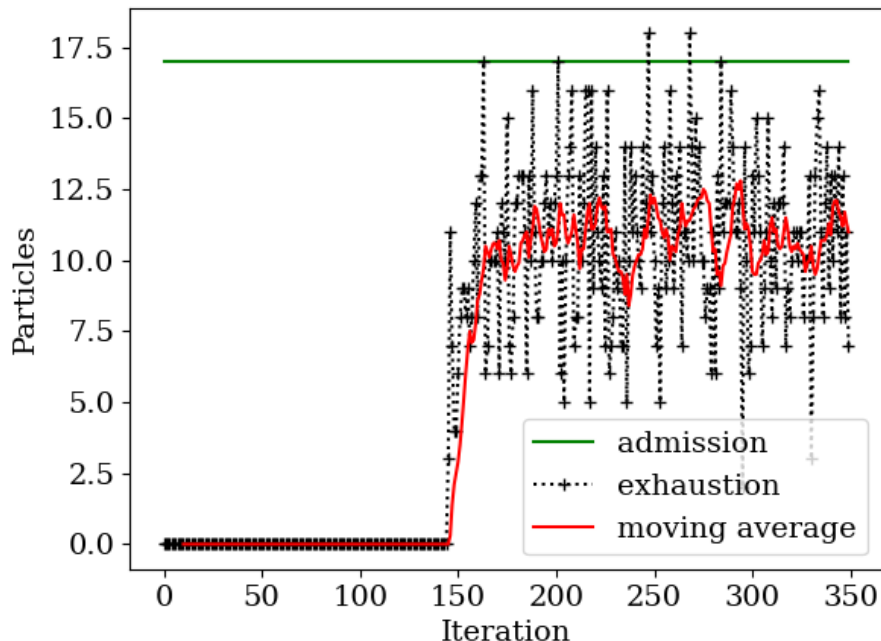


Figure 7.18: Particles' admission and exhaustion rates for diesel-powered engines, for a DPF with an internal steep edge.

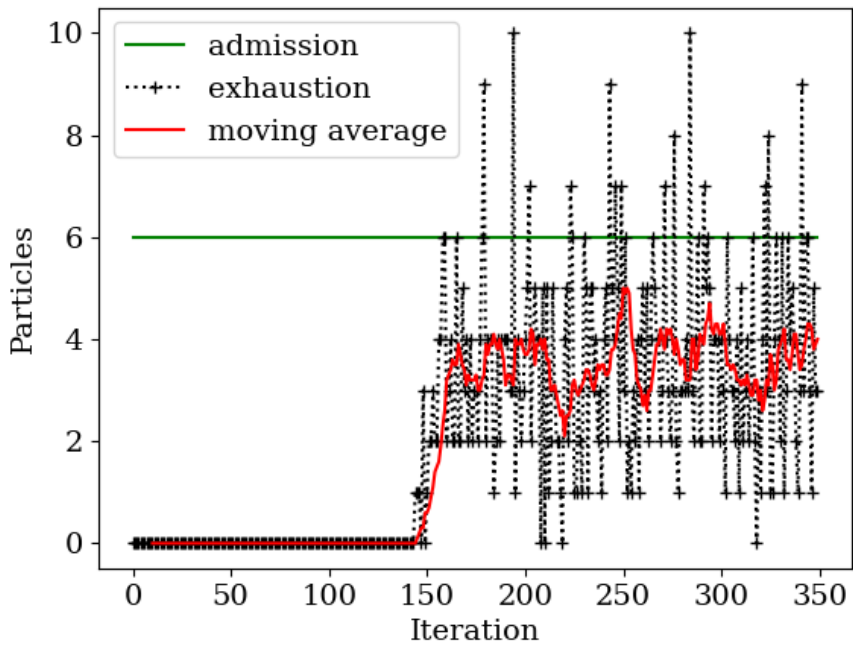


Figure 7.19: Particles' admission and exhaustion rates for biodiesel-powered engines, for a DPF with an internal steep edge.

The filtration efficiencies for diesel and biodiesel were calculated as 35% and 40%, respectively, showing that this geometry brings no contribution concerning a better filtration of particulate matter. In fact, it is possible to notice a decrease in filtration efficiency.

7.6.2 The External Steep Edge

As for the external steep edge, the scheme is shown in Figure 7.20, where a convergent channel is formed. This time, the main channel and the opposite wall remain unaltered, so that the only difference from the original geometry is the linear increase of the filter's thickness, but with the same average value.

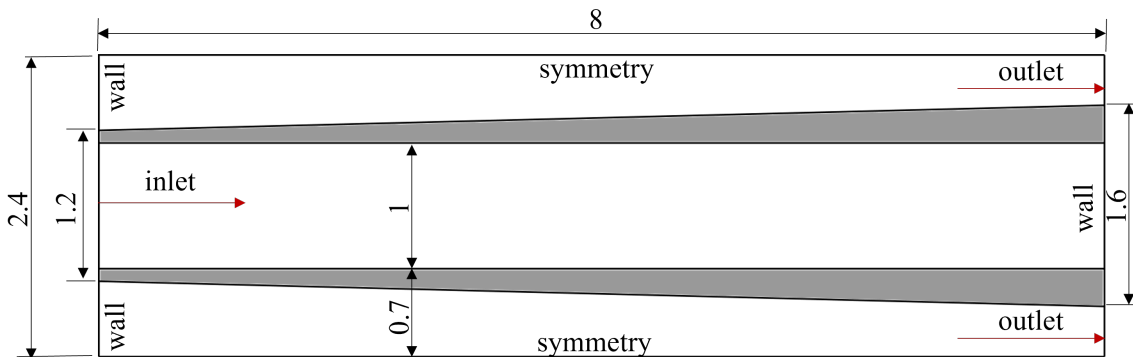


Figure 7.20: Scheme of the DPF with external steep edge.

When the permanent regime is reached, the horizontal velocity field and particle distribution are as shown in Figures 7.21 and 7.22, for diesel and biodiesel, respectively.

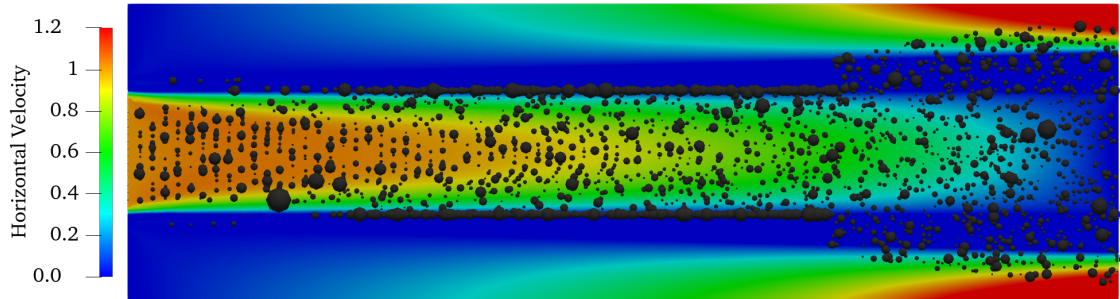


Figure 7.21: Velocity field and particle distribution in the permanent regime for the diesel DPF with an external steep edge.

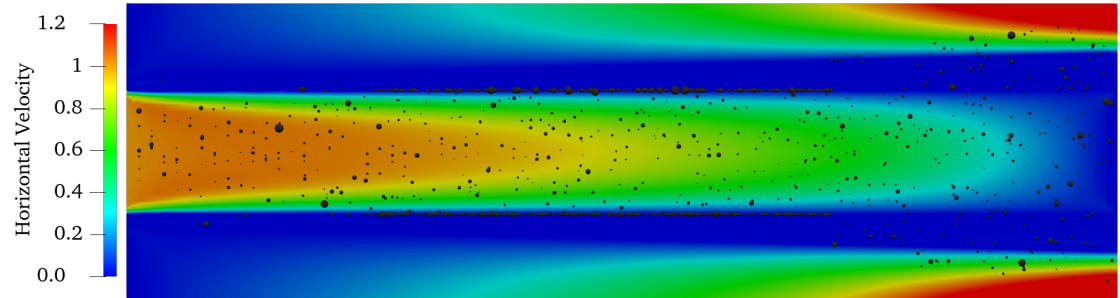


Figure 7.22: Velocity field and particle distribution in the permanent regime for the biodiesel DPF with an external steep edge.

Particulate rates for this geometry are shown next, where, once again, the moving average is used to smooth the data:

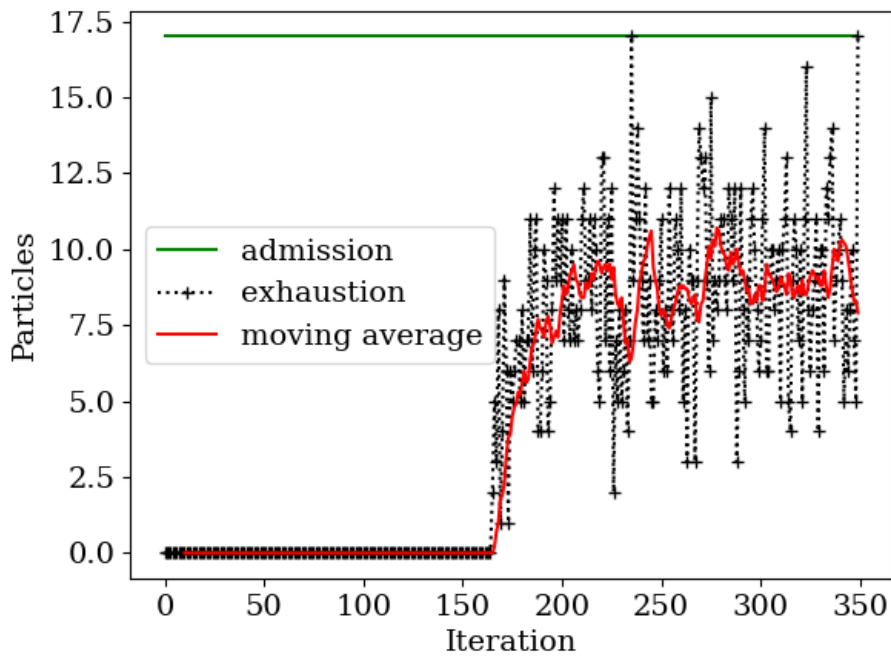


Figure 7.23: Particles' admission and exhaustion rates for diesel-powered engines, for a DPF with an external steep edge.

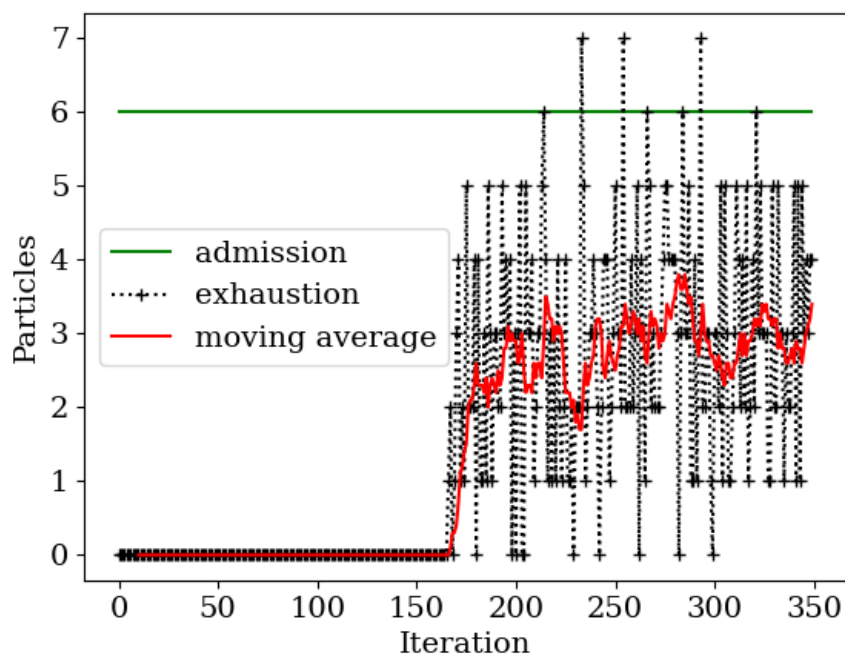


Figure 7.24: Particles' admission and exhaustion rates for biodiesel-powered engines, for a DPF with an external steep edge.

For this case, the filtration efficiencies for diesel and biodiesel were determined to

be 47% and 51%, respectively. Hence, this change in geometry generated an increase of 17.5% for the diesel DPF and 18.6% for the biodiesel one.

Such result is in accordance to what was expected, since most particles exit in the final portion of the channel due to the higher pressure gradient. In this design, this final portion has a thicker filter layer. For the initial portion, the layer thickness is reduced to maintain the average thickness for comparison and this reduction does not seem to cause any alteration in particle retention.

7.6.3 The Internal Step-shaped Edge

In this third analysis of the filter, internal steps, forming cavities along the geometry, are added to the original geometry, as seen in Figure 7.25.

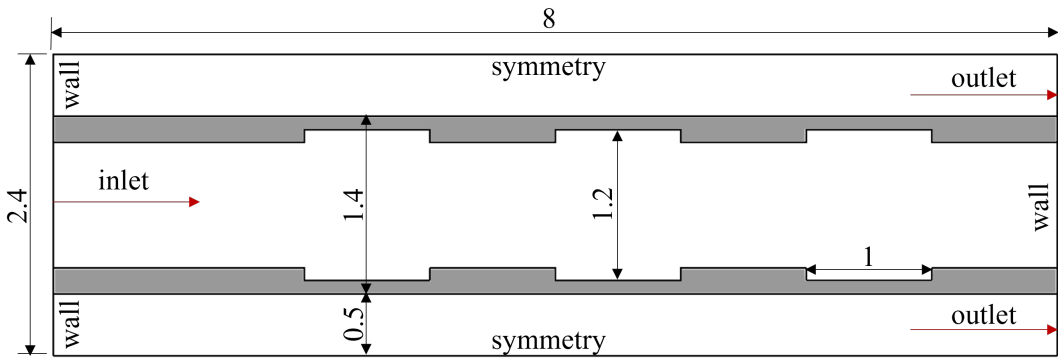


Figure 7.25: Scheme of the DPF with internal step-shaped edge.

Once again, after the system reaches a permanent regime, the results are shown as follows:

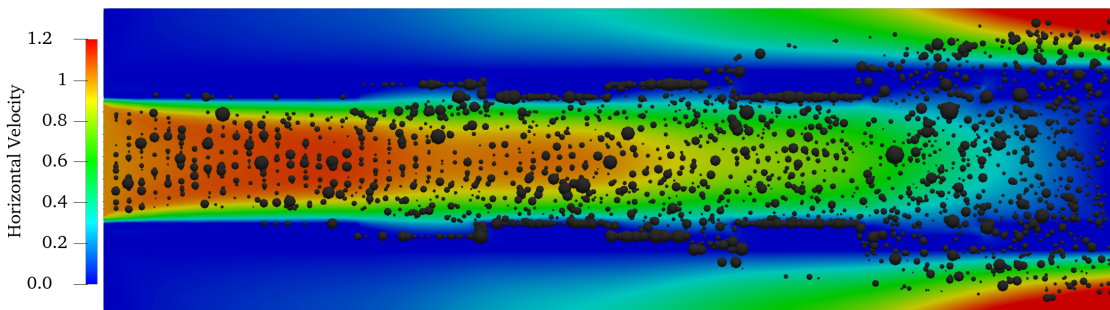


Figure 7.26: Velocity field and particle distribution in the permanent regime for the diesel DPF with an internal step-shaped edge.

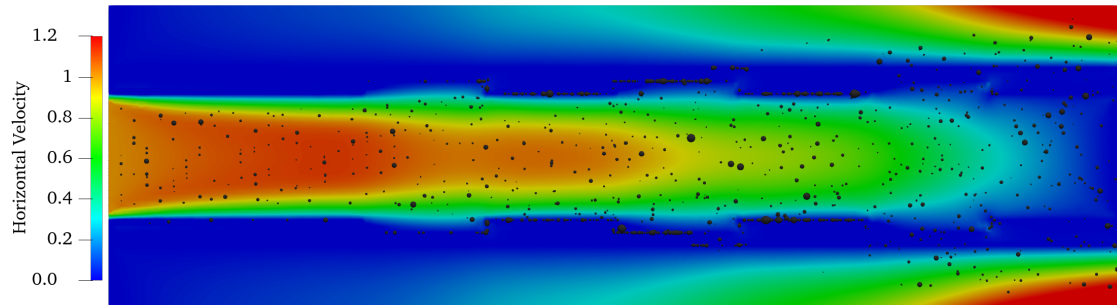


Figure 7.27: Velocity field and particle distribution in the permanent regime for the biodiesel DPF with an internal step-shaped edge.

The rates of particulate admission and exhaustion are shown below, for both fuels:

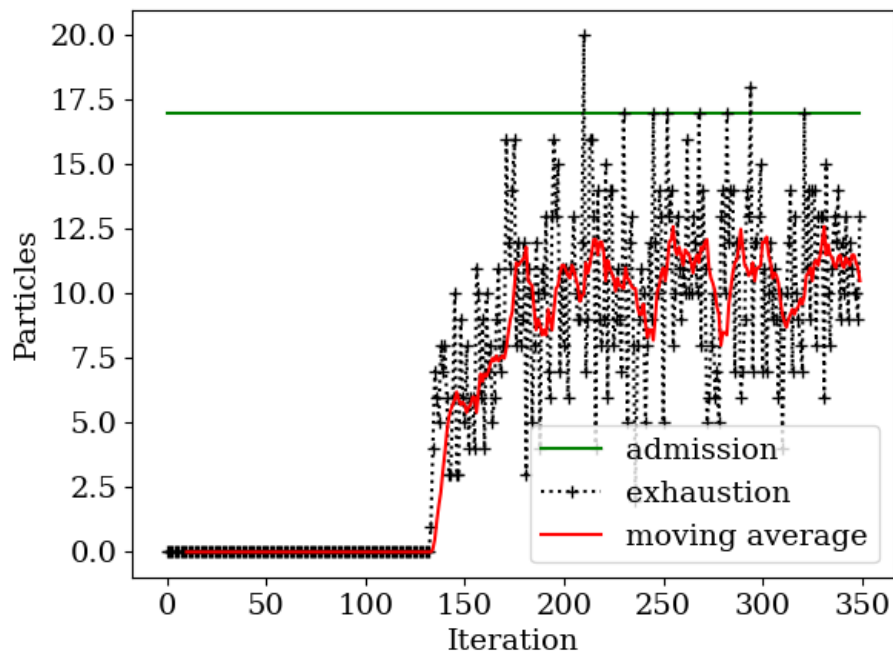


Figure 7.28: Particles' admission and exhaustion rates for diesel-powered engines, for a DPF with an internal step-shaped edge.

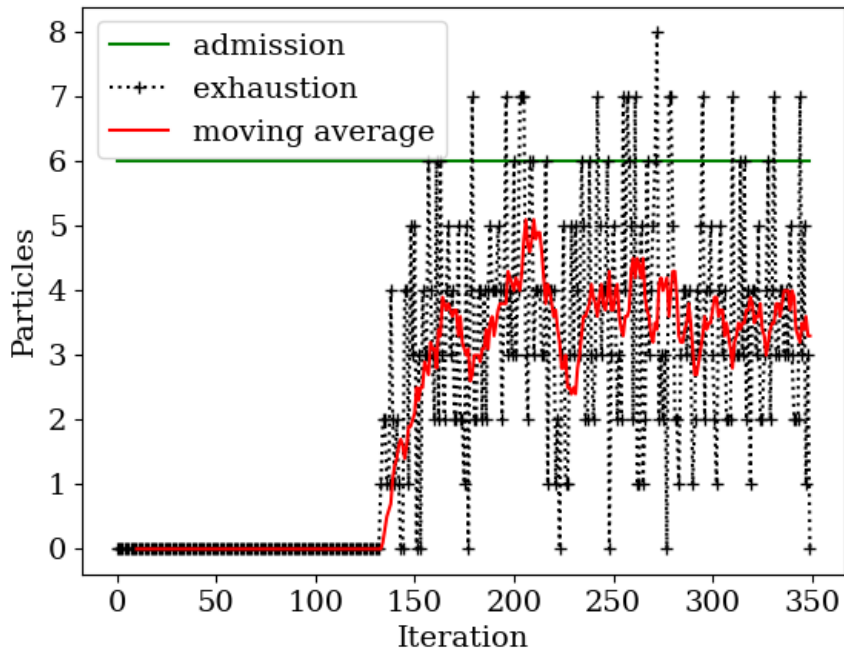


Figure 7.29: Particles' admission and exhaustion rates for biodiesel-powered engines, for a DPF with an internal step-shaped edge.

Analyzing the data shown in Figures 7.28 and 7.29, a reduction in filtration efficiency, of about 10% for diesel and 7% for biodiesel, can be noticed. In spite of the increase of the contact surface between the fluid and the porous walls, this does not prove to be sufficient to collect enough particles along the channel to compensate the ones that escape through the final portion of the channel, due to a higher pressure gradient, as has already been shown.

7.6.4 The External Step-shaped Edge

Similarly to the previous cases, an external version of the step-shaped edge is tested. The scheme is shown in Figure 7.30.

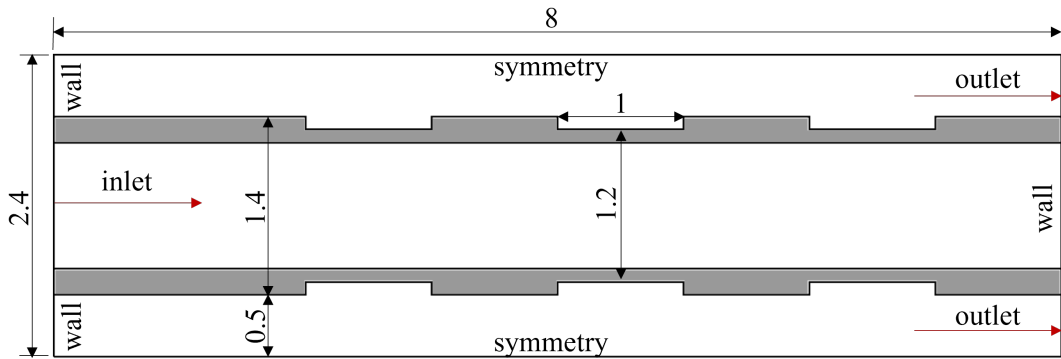


Figure 7.30: Scheme of the DPF with external step-shaped edge.

In the permanent regime, for both fluid phase and particulate rates, Figures 7.31 and 7.32 represent the filter's scenario.

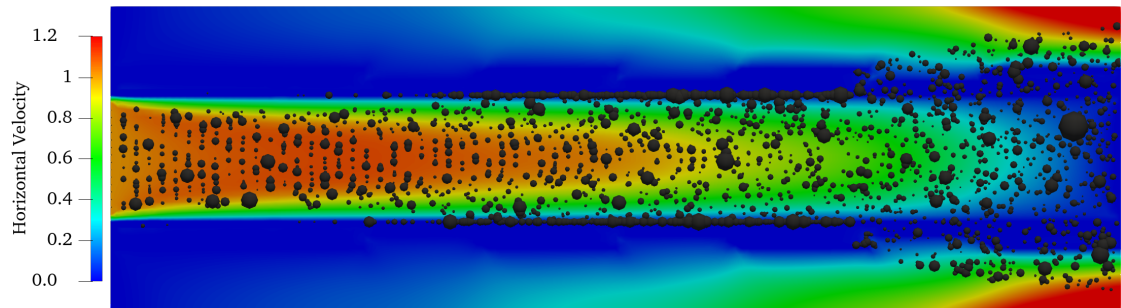


Figure 7.31: Velocity field and particle distribution in the permanent regime for the diesel DPF with an external step-shaped edge.

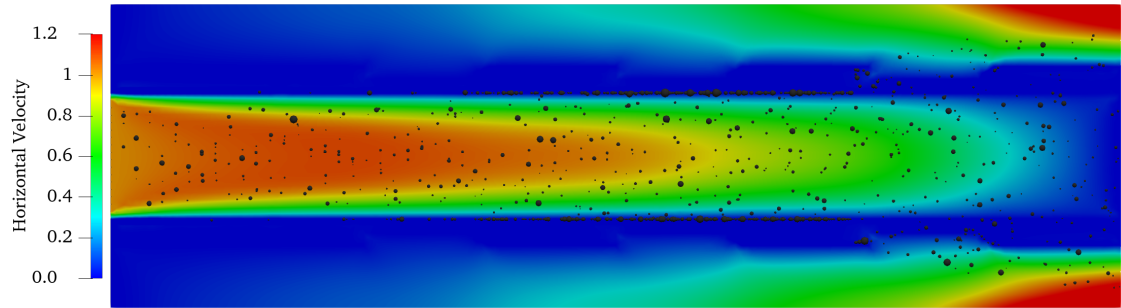


Figure 7.32: Velocity field and particle distribution in the permanent regime for the biodiesel DPF with an internal step-shaped edge.

The admission and exhaustion rates can be seen in Figures 7.33 and 7.34, where, once again, the moving average is determined in order to better visualize the results obtained.

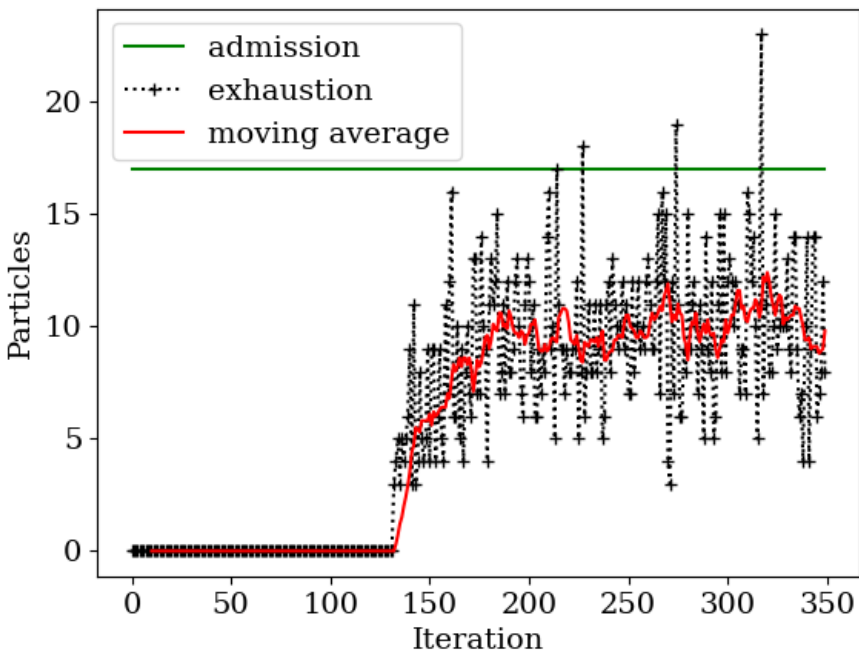


Figure 7.33: Particles' admission and exhaustion rates for diesel-powered engines, for a DPF with an external step-shaped edge.

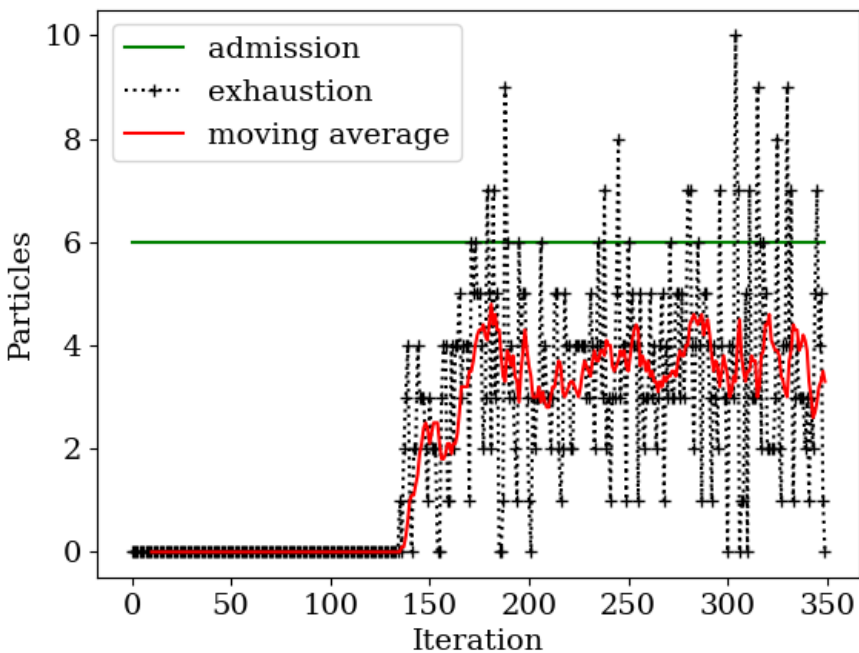


Figure 7.34: Particles' admission and exhaustion rates for biodiesel-powered engines, for a DPF with an external step-shaped edge.

For diesel engines, the filtration efficiency was exactly the same as that observed in the original geometry, with a flat filter. A small reduction of 2.3% was detected

in the biodiesel one, which is not significant, leading to the conclusion that, for this geometry, the exhaustion rates are the same as the original case. This was expected since the thickness along the channel does not change significantly to compensate the steps and, hence, in the final portion of the filter, there is no extra porous layer to slow down particles impelled by the higher pressure gradient.

7.6.5 The Internal Harmonic-shaped Edge

The same procedure that was adopted in the previous cases was used in this one, having the internal edge a harmonic shape, as shown in Figure 7.35.

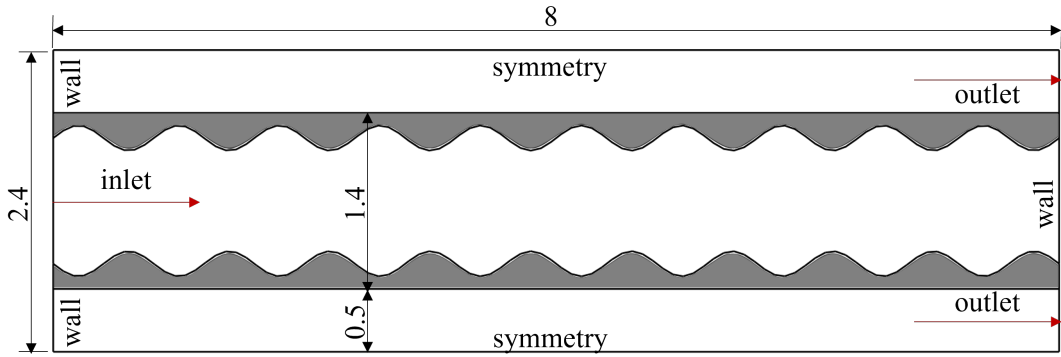


Figure 7.35: Scheme of the DPF with internal harmonic-shaped edge.

As already noticed in the previous cases, diesel and biodiesel filters have a similar behavior in the permanent regime, differing the size and amount of particles. The same happens for this case, as shown next:

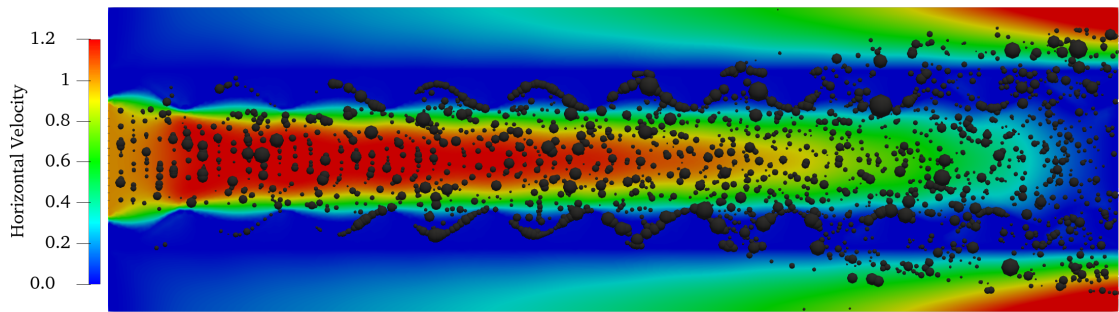


Figure 7.36: Velocity field and particle distribution in the permanent regime for the diesel DPF with an internal harmonic-shaped edge.

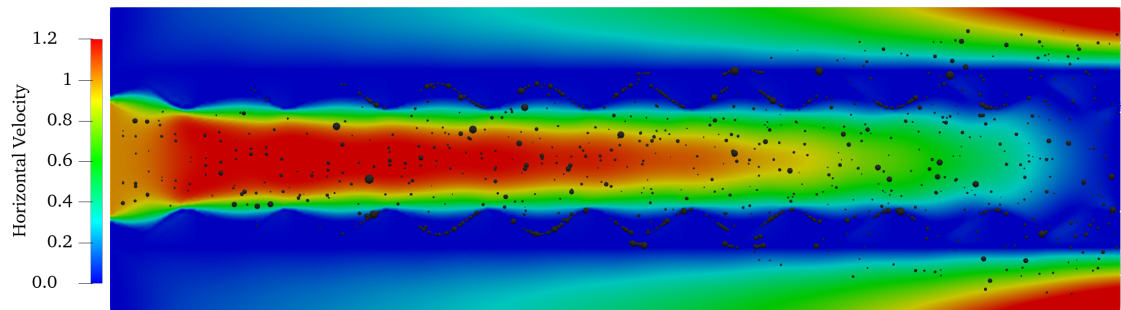


Figure 7.37: Velocity field and particle distribution in the permanent regime for the biodiesel DPF with an internal harmonic-shaped edge.

As was made for the other geometries, admission and exhaustion rates were compared for both fuels, as shown below:

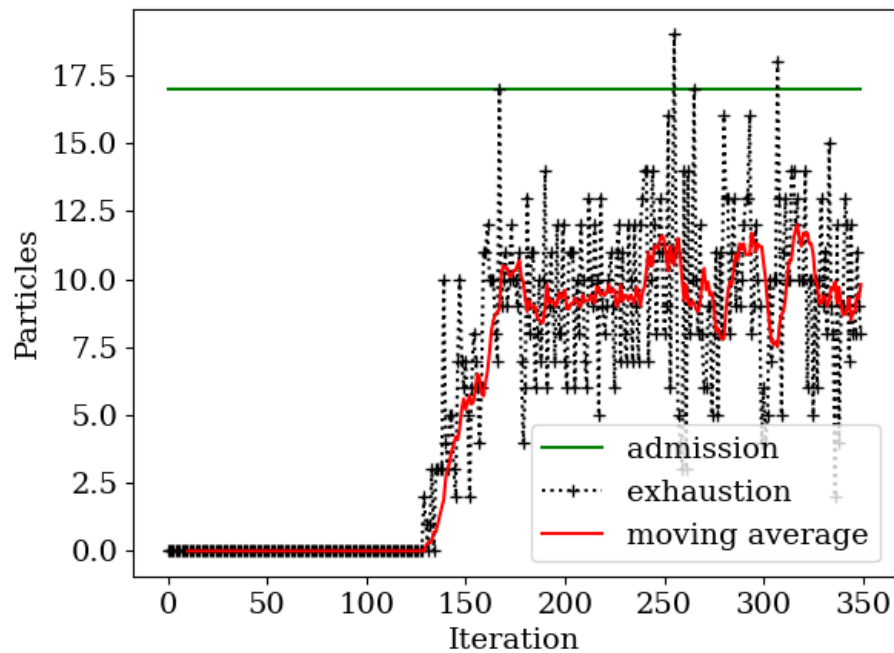


Figure 7.38: Particles' admission and exhaustion rates for diesel-powered engines, for a DPF with an internal harmonic-shaped edge.

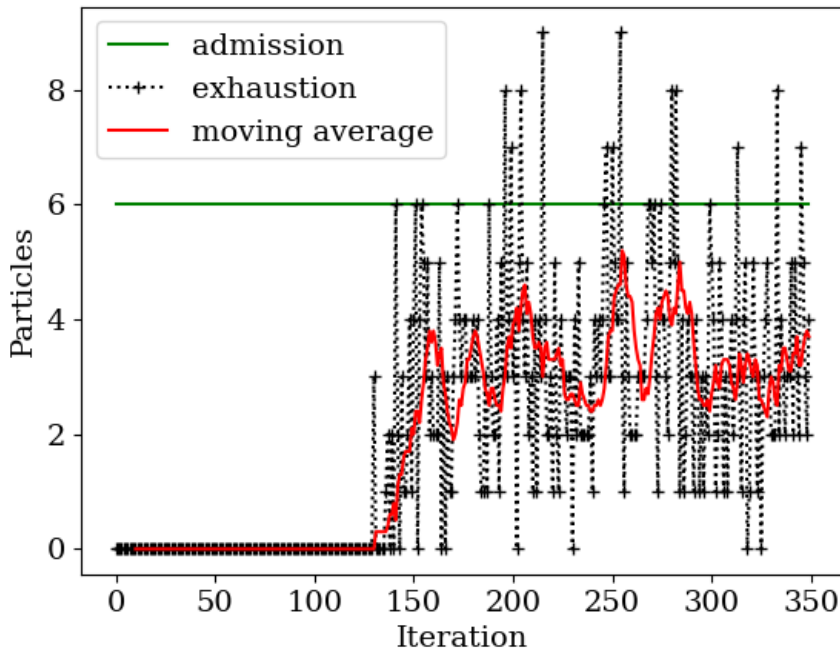


Figure 7.39: Particles' admission and exhaustion rates for biodiesel-powered engines, for a DPF with an internal harmonic-shaped edge.

The filtration rates were determined to be of 42% and 44%, for diesel and biodiesel, respectively. Comparing with the flat filter, gains of 5% in diesel and 2.3% in biodiesel filtration efficiencies were noticed. In spite of the positive numbers, this result does not seem to be significant in terms of enhancement of the filter. The slightly better filtration is due to a longer contact edge between the fluid and the porous walls, retaining a considerable amount of particles, as shown in Figures 7.36 and 7.37.

7.6.6 The External Harmonic-shaped Edge

The last case studied is the external version of the previous geometry, as follows:

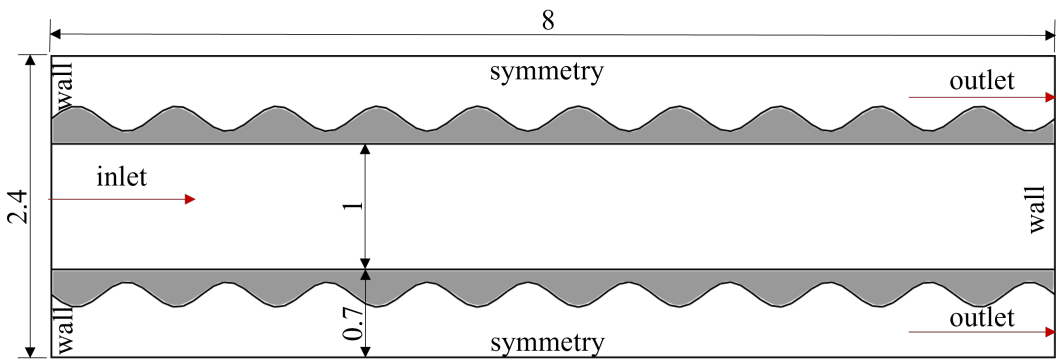


Figure 7.40: Scheme of the DPF with external harmonic-shaped edge.

Then, for the permanent state, the aspects observed for both diesel and biodiesel filters are shown in Figures 7.41 and 7.42, respectively.

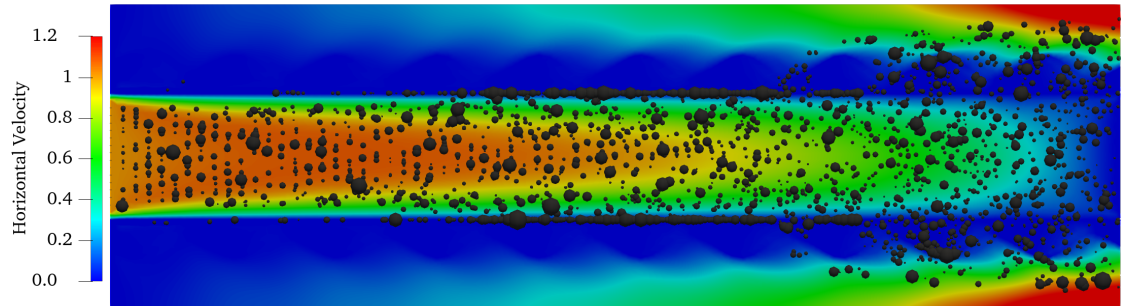


Figure 7.41: Velocity field and particle distribution in the permanent regime for the diesel DPF with an external harmonic-shaped edge.

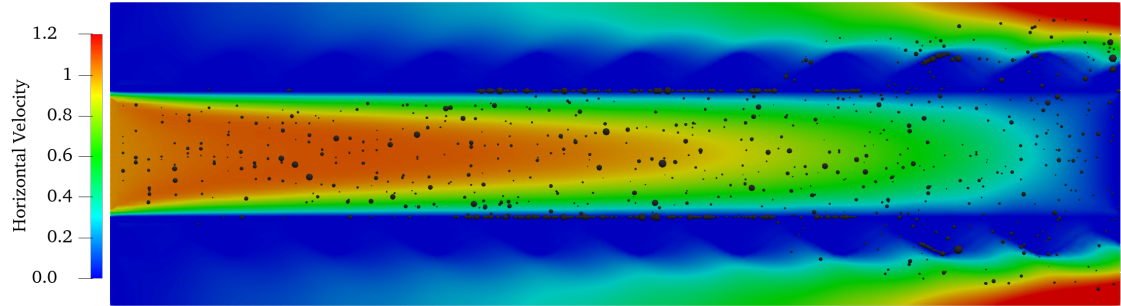


Figure 7.42: Velocity field and particle distribution in the permanent regime for the biodiesel DPF with an external harmonic-shaped edge.

Observing the exhaustion rates in Figures 7.43 and 7.44, the filtration efficiencies were calculated as 36% and 40%, for diesel and biodiesel, respectively. Such values show a decrease in efficiency when compared to the original geometry (the flat filter). This can be explained by the oscillation in the filtration layers at the end of the DPF. Since in some points, the thickness is below the average, this does not seem to compensate the regions where it is above, resulting in lower filtration efficiency values for both fuels.

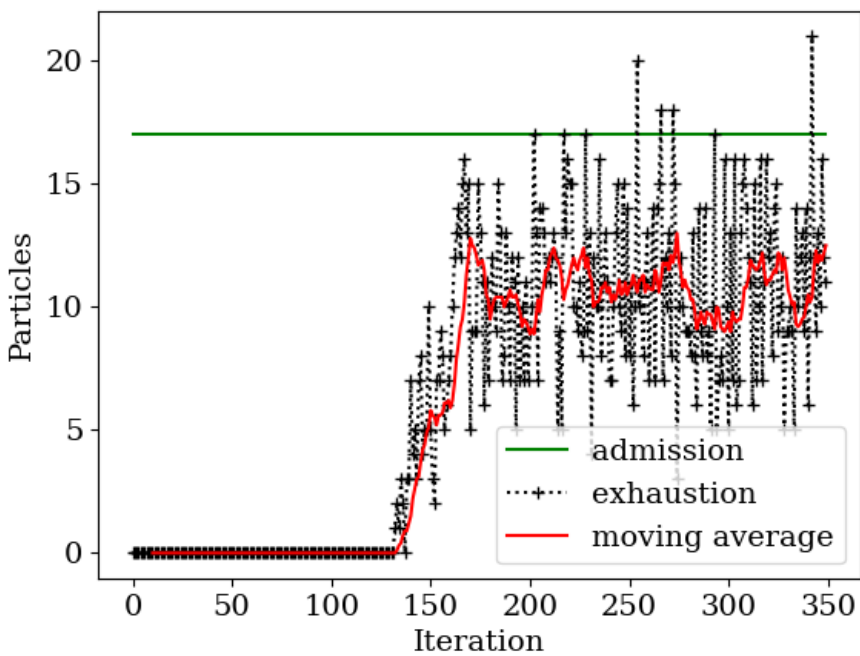


Figure 7.43: Particles' admission and exhaustion rates for diesel-powered engines, for a DPF with an external harmonic-shaped edge.

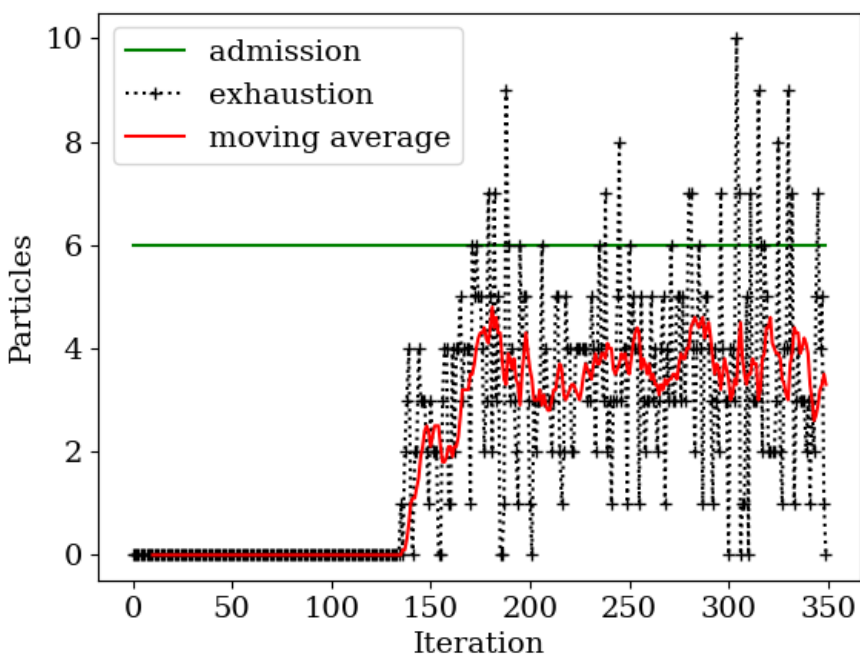


Figure 7.44: Particles' admission and exhaustion rates for biodiesel-powered engines, for a DPF with an external harmonic-shaped edge.

7.6.7 Comparison of Cases

All the analyses presented in this section were intended to help find the influence of the geometry of the DPF on its efficiency, for either diesel or biodiesel. As was presented, a thicker porous region in the outlet provides a better filtration due to the increased pressure gradient. At first, the same result was expected with the internal steep edge case, but a convergent channel is believed to push particles against the porous wall, facilitating their trespassing into the outlet channels, which does not happen in the external steep edge case. All the other cases provide no significant improvement, since they do not offer this compensation in thickness along the channel, as the pressure gradient increases. Table 7.3 sums up the results obtained and the advantages or disadvantages of changing the filter's geometry. Since particulate injections are made in a random way, according to the distribution shown for each fuel, such table is not considered a deterministic evaluation of the results.

Table 7.3: Comparison between filter geometries for diesel and biodiesel, regarding filtration efficiency.

	Diesel	Biodiesel	Comparison (diesel)	Comparison (biodiesel)
Flat Filter	40%	43%	-	-
Internal Steep Edge	35%	40%	-12.5%	-7.0%
External Steep Edge	47%	51%	+17.5%	+18.6%
Internal Step-shaped Edge	36%	40%	-10.0%	-7.0%
External Step-shaped Edge	40%	42%	0.0%	-2.3%
Internal Harmonic-shaped Edge	42%	44%	+5.0%	+2.3%
External Harmonic-shaped Edge	36%	40%	-10.0%	-7.0%

The advantages of biodiesel over diesel are reinforced in these simulations, since not only the first one produces less particulate matter in its consumption, the filtration efficiency of the DPF was noticed to be higher for all the geometries analyzed. Also, with an external steep edge, there was a higher percentage increase, when compared to the diesel engine.

Considering the findings in this section, an experimental analysis with an external steep-edged DPF should be encouraged, in order to evaluate the real reduction in particulate emissions and propose enhancements to the design of Diesel Particulate Filters.

Chapter 8

Conclusion

This work presented a broad literature review on both biofuel scenario and numerical simulation for fluid dynamics, going through a variety of studies about renewable sources of energy and how they can substitute fossil ones, as well as numerical methods to simulate multiphase flows, which is the aspect observed in emissions resulted from fuel consumption.

The whole formulation of fluid mechanics is presented, going from the integral forms of mass and momentum conservation to the Navier-Stokes equations. Energy conservation equation is also presented, as a way of calculating temperature in fluid systems. The Darcy/Fochheimer formulation complements the governing equations to represent the resistance imposed by porous media and also an alternative equation for mixed free/porous media is presented. For solid spherical bodies, the main forces exerted by the fluid are calculated, introducing the drag coefficient (C_D) graphical and empirical calculations. Newton's second law is, then, used to calculate the acceleration of each particle.

The finite element method is used in the Navier-Stokes and Darcy/Forchheimer differential system of equations along with continuity and energy formulations. For the material derivative, a semi-Lagrangian approach was used, in order to avoid non-linear terms of the equations. The final result is a linear system of equations for which the variables are the pressure, temperature and velocity values for each point.

The computational implementation was presented, for which the Object Oriented Python was used to create the several classes and make a more adaptive code. A Graphical User Interface (GUI) was developed to help handle the input *.xml* files used by the program to set parameters, contour and initial conditions more easily. Such GUI was also useful to track real-time simulation results. A command-line option is also used, where the geometric domain and parameter are defined and given as inputs to the main program. The start, the end and time step of the case may also be chosen when running the code.

A first verification of the implemented method is made for the traditional lid-driven cavity problem, comparing results to the ones from the literature, after a mesh convergence analysis was made. The satisfactory plot of both solutions demonstrate that the implementation is correct. Second the backward-facing step problem is analyzed and qualitatively compared with the literature, resulting in velocity fields that were within the expected behavior. Then, a transient problem, which is the flow around a cylinder is considered in order to demonstrate the code's adequacy to a fully transient case. Introducing the particulate movement study, a convective cavity was simulated, in order to determine stream lines generated by a temperature gradient. The temperature field showed its advection through the fluid and particles' positions the velocity field generated were tracked. Next, an expansion problem with heat transfer associated was analyzed with respect to temperature field and particles' movement, bringing to discussion the importance of recirculation zones in terms of particle emissions. The temperature field was also affected by said recirculation zones, due to the advective term of the energy conservation formulation. Then, the first example of a mixed free/porous flow was simulated in a Poiseuille-like geometry. In accordance to the resistance imposed by the porous medium, a steeper pressure drop is observed in this region and a lower velocity profile maximum is noticed as well, when compared to the free-flow region. The last verification is made in a flow over porous medium problem, for which the horizontal velocity profile is compared with the literature. The method proposed here provided a closer result to other more precise methods than the one proposed by the authors, which is considered adequate for regions that are not near the interface of the media.

Finally, the Diesel Particulate Filter (DPF) was presented. First, a description of its general geometry and working principles were shown and assumptions were made, regarding simplifications in the geometric aspects to run the simulation. The characteristics of single channels were presented and a two-dimensional approach showed to be appropriate. The particulate matter resulted from diesel and biodiesel consumption was also analyzed and a curve fit of the log-normal distribution was made to determine statistical parameters, such as the geometrical mean diameter and its logarithmic standard deviation. A first simulation, with a longer channel, was made, in order to compare with the one obtained in the literature, using a commercial software. Then, particles were introduced in a randomly distributed range and their path along the domain was observed. Such results led to the final simulation, for which a constant injection of particles is considered, approaching to what happens in reality.

The study showed that diesel-powered engines produce much more particulate matter than biodiesel-powered ones and, for that reason, in spite of the filters, more diesel soot particles end up escaping to the atmosphere. Although biodiesel soot is

present in a lower concentration, their hydraulic diameter range are almost entirely within the nanoparticle range. Such particulate matter may be more harmful to human health if expelled in large quantity to the atmosphere. A geometry analysis was also provided, showing that a steeper external edge enhances filtration efficiency, when compared to other geometries of the filter.

In order to complement and adapt this work, a few future improvements are listed below:

- Implement particle interactions and their interference in the fluid, called four-way coupling, considering particulate size and how they interfere in filtration when attached to the filter;
- Consider non-adiabatic particles and evaluate their dynamics compared to adiabatic ones;
- Optimize the semi-lagrangian and lagrangian calculations to save computational cost;
- Improve GUI interactions for a better user experience and input/output manipulation;
- Implement the option of quadrilateral-element mesh simulation;
- Adapt the code for three-dimensional simulation and, therefore, simulate more complex cases.

References

- [1] KIM, N., CHO, S., MIN, K. “A study on the combustion and emission characteristics of an SI engine under full load conditions with ethanol port injection and gasoline direct injection”, *Fuel*, v. 158, pp. 725–732, 2015. doi: <http://dx.doi.org/10.1016/j.fuel.2015.06.025>.
- [2] HASHIM, H., NARAYANASAMY, M., YUNUS, N. A., et al. “A cleaner and greener fuel: Biofuel blend formulation and emission assessment”, *Journal of Cleaner Production*, pp. 1–10, 2016. doi: <http://dx.doi.org/10.1016/j.jclepro.2016.06.021>.
- [3] RODRÍGUEZ-FERNÁNDEZ, J., LAPUERTA, M., SÁNCHEZ-VALDEPEÑAS, J. “Regeneration of diesel particulate filters: Effect of renewable fuels”, *Renewable Energy*, v. 104, pp. 30–39, 2017. doi: <http://dx.doi.org/10.1016/j.renene.2016.11.059>.
- [4] CIMOLIN, F., DISCACCIATI, M. “Navier–Stokes/Forchheimer models for filtration through porous media”, *Applied Numerical Mathematics*, v. 72, pp. 205–224, 2013. doi: <https://doi.org/10.1016/j.apnum.2013.07.001>.
- [5] CROWE, C. T., SCHWARZKOPF, J. D., SOMMERFELD, M., et al. *Multiphase Flows with Droplets and Particles*. USA, CRC Press, 2012.
- [6] “Python”. <https://www.python.org/>, 2021.
- [7] DA CUNHA, L. H. C. *Ale Finite Element Method for Simulating Flows with the Stream Function-Vorticity Formulation*. Master’s thesis, Mech. Eng. Program of Universidade do Estado do Rio de Janeiro, 2020.
- [8] MESQUIDA, I. M. V. *Analysis of Flow Pattern in a Gasoline Particulate Filter using CFD*. Master’s thesis, Chemical and Materials Engineering - University of Alberta, 2019.
- [9] ERTUK, E. “Numerical solutions of 2-D steady incompressible flow over a backward-facing step, Part I: High Reynolds number solutions”, *Com-*

puters and Fluids, v. 37, pp. 633–655, 2007. doi: doi:10.1177/0954407013504390.

- [10] REHAM, S. S., MASJUKI, H. H., KALAM, M. A., et al. “Study on stability, fuel properties, engine combustion, performance and emission characteristics of biofuel emulsion”, *Renewable and Sustainable Energy Reviews*, v. 52, pp. 1566–1579, 2015. doi: <http://dx.doi.org/10.1016/j.rser.2015.08.013>.
- [11] XU, L., CHENG, J.-H., LIU, P., et al. “Production of bio-fuel oil from pyrolysis of plant acidified oil”, *Renewable Energy*, 2018. doi: 10.1016/j.renene.2018.07.012.
- [12] BATCHELOR, G. K. *An Introduction to Fluid Dynamics*. USA, Cambridge University Press, 2000.
- [13] ZHANG, K., WANG, C.-A., TAN, J.-Y. “Numerical study with OpenFOAM on heat conduction problems in heterogeneous media”, *International Journal of Heat and Mass Transfer*, pp. 1156–1162, 2018.
- [14] BESSAIH, H., GARRIDO-ATIENZA, M. J., SCHMALFUSS, B. “On 3D Navier–Stokes equations: Regularization and uniqueness by delays”, *Physica D*, 2018. doi: <https://doi.org/10.1016/j.physd.2018.03.004>.
- [15] ABDELWAHED, M., CHORFI, N., HASSINE, M. “A stabilized finite element method for stream function vorticity formulation of Navier-Stokes equations”, *Electronic Journal of Differential Equations*, v. 2017, n. 24, pp. 1–10, 2011.
- [16] TORO, L., CARDONA, C. A., PISARENKO, Y. A., et al. “THE FINITE ELEMENT METHOD (FEM): AN APPLICATION TO FLUID MECHANICS AND HEAT TRANSFER”, *Fine Chemical Technologies*, v. 13, n. 4, 2018. doi: 10.32362/2410-6593-2018-13-4-17-25.
- [17] BAGAI, S., KUMAR, M., PATEL, A. “THE FOUR-SIDED LID DRIVEN SQUARE CAVITY USING STREAM FUNCTION-VORTICITY FORMULATION”, *Journal of Applied Mathematics and Computational Mechanics*, pp. 17–30, 2020. doi: 10.17512/jamcm.2020.2.02.
- [18] ZITOUNI, A. H., SPITERI, P., AISSANI, M., et al. “Thermal and fluid flow modeling of the molten pool behavior during TIG welding by stream vorticity method”, *International Journal on Interactive Design and Manufacturing (IJIDeM)*, 2020. doi: <https://doi.org/10.1007/s12008-020-00653-0>.

- [19] HOFFMANN, A. C., ÅSHILD SKORPEN, CHANG, Y.-F. “Positron emission particle tracking and CFD investigation of hydrocyclones acting on liquids of varying viscosity”, *Chemical Engineering Science*, v. 200, pp. 310—319, 2019. doi: <https://doi.org/10.1016/j.ces.2019.01.061>.
- [20] BARGHI, S. N. S. S. “REDUCTION OF FINE PARTICLE EMISSION FROM A PRILLING TOWER USING CFD SIMULATION”, *Chemical Engineering Research and Design*, 2015. doi: <http://dx.doi.org/doi:10.1016/j.cherd.2016.01.017>.
- [21] BORELLO, D., RISPOLI, F., VENTURINI, P. “An Integrated Particle-Tracking Impact/Adhesion Model for the Prediction of Fouling in a Subsonic Compressor”, *Journal of Engineering for Gas Turbines and Power*, v. 134, 2012. doi: [10.1115/1.4006840](https://doi.org/10.1115/1.4006840)].
- [22] GREIFZU, F., KRATZSCH, C., FORGBER, T., et al. “Assessment of particle-tracking models for dispersed particle-laden flows implemented in OpenFOAM and ANSYS FLUENT”, *Engineering Applications of Computational Fluid Mechanics*, v. 10, n. 1, pp. 30–43, 2015. doi: [10.1080/19942060.2015.1104266](https://doi.org/10.1080/19942060.2015.1104266).
- [23] ANJOS, G. R. *A 3D ALE Finite Element Method for Two-Phase Flows with Phase Change*. Ph.d. thesis, École Polytechnique Fédérale De Lausanne, 2012.
- [24] ZIENKIEWICZ, O. C., TAYLOR, R. L. *The Finite Element Method - Volume 3*. Wiley, 2000.
- [25] RUGGIERO, M. G., DA ROCHA LOPES, V. L. *Cálculo Numérico - Aspectos Teóricos e Computacionais*. Brazil, Makron Books do Brasil, 2012.
- [26] WANG, T. J. “A methodology for estimating the permeability of a soot deposit in a wallflow diesel particulate filter”, *Journal of Automobile Engineering*, v. 228, pp. 1154–1169, 2014. doi: [doi:10.1177/0954407013504390](https://doi.org/10.1177/0954407013504390).
- [27] WILLIAMS, A., MCCORMICK, R. L., HAYES, R. R., et al. “Effect of Biodiesel Blends on Diesel Particulate Filter Performance”, *Fluid Systems Conference and Exhibition*, 2006.
- [28] PINHEIRO, J. I., CARVAJAL, S. R., DA CUNHA, S. B., et al. *Probabilidade e estatística: Quantificando a incerteza*. Brazil, GEN LTC, 2012.